Air-sea interaction and the influence of sea ice during cold-air outbreaks over the subpolar North Atlantic Ocean

A thesis submitted to the School of Environmental Sciences at the University of East Anglia in partial fulfilment of the requirements for the degree of Doctor of Philosophy

Christopher Barrell

University of East Anglia

School of Environmental Sciences

April 2023

Abstract

Air-sea interaction in the subpolar North Atlantic (SPNA) has a strong influence on weather in the Northern Hemisphere and controls the formation of dense waters that feed into the Atlantic Meridional Overturning Circulation (AMOC). During cold-air outbreaks (CAOs) the strongest turbulent heat fluxes occur near the ice edge, hence the distribution of sea ice is critically important for determining air-sea interaction. I evaluate coupled model simulations for the SPNA and the influence of the marginal ice zone (MIZ) in short-range weather forecasts and long-range climate projections. Coordinated atmosphere-ocean measurements made during the Iceland-Greenland Seas Project (IGP) field campaign in 2018 are used to evaluate the then semi-operational Met Office Global Coupled model 2 (GC2). It is shown to simulate cold biased sea surface temperatures up to approximately 200 km from the ice edge due to an overly wide MIZ, which contributes to forecast error downstream.

A further quantitative analysis of 10-day sea ice forecasts from the Met Office Global Coupled model 3.1 (GC3.1) was performed. Evaluation using two satellite sea ice products shows that for individual cases dynamic sea ice in the coupled model provides no clear improvement over a persistent sea ice field. However, sensitivity tests with two ocean model grid resolutions (1/4° and 1/12°) and a modified atmospheric drag parameterisation over the marginal ice zone show that the 1/12° ocean model provides advancement in the simulation of eddy driven features along the ice edge. Moreover, the largest source of error in the model experiments is the sea ice input field from the commonly used OSI-SAF 401 operational product highlighting an opportunity for improvement.

Last, the future of air-sea interaction over the SPNA is investigated using output from the HadGEM3-GC3.1 climate model, produced as part of the 6th Coupled Model Inter-Comparison Project (CMIP6). Contrary to the short-range forecasts, comparison of two model resolutions (MM: 60 km atmosphere - 1/4° ocean; HH: 25 km – 1/12°) shows that the HH model accurately simulates the historic sea ice distribution, which provides confidence in its future projections. Nonetheless, the simulations agree in predicting that under climate change the subpolar North Atlantic will see further significant reductions in wintertime air-sea turbulent fluxes later in the 21st century, which may reduce the formation of dense waters that feed into the lower limb of the AMOC.

Acknowledgments

I would like to thank my primary supervisor, Ian Renfrew. Throughout the PhD you have been so generous with opportunities and advice, for which I am very grateful. Also, my supervisors Andrew Elvidge, Steven Abel and John King for all your astute guidance, ideas and interest; Tim Graham for your kind involvement; and Helge Goessling for your keen assistance.

The Iceland-Greenland Seas Project field campaign was a wonderful and enlightening experience. I am immensely thankful to everyone that I have had the chance to work with. Likewise, I am grateful for the hospitality and kindness I received while visiting the University of Bergen, particularly from Kjetil Våge and Joachim Reuder and their welcoming groups.

To my sister Kate, I am extremely grateful for you always looking out for me. I would not have gotten to this point if you hadn't. To my Dad, and my family and friends, thank you for your endless support and encouragement.

To my Freya, words cannot describe how thankful I am for your patience, warmth, understanding, lasagna, lockdown crossword breaks, and most of all, always keeping me smiling.

Last, to my late mother Sandra, your love, unbounded generosity and spontaneous adventures still guide me today, thank you.

Contents

x

List of Figures

List of Tables

List of Symbols and Acronyms

ABL	Atmospheric Boundary Layer
AMOC	Atlantic Meridional Overturning Circulation
AMSR2	Advanced Microwave Scanning Radiometer 2
CAO	Cold-Air Outbreak
DJFM	December, January, February, March
ECMWF	European Centre for Medium-range Weather Forecasting
ERA5	ECMWF's 5th generation reanalysis
GC2	Met Office Global Coupled model version 2.0
GC3.1	Met Office Global Coupled model version 3.1
HadGEM3-GC3.1	Third Hadley Centre Global Environment Model in the GC3.1 configuration
IIEE	Integrated Ice Edge Error
MIZ	Marginal Ice Zone
NAO	North Atlantic Oscillation
NWP	Numerical Weather Prediction
OSTIA	Operational Sea Surface Temperature and Ice Analysis
RH_{2m}	Relative Humidity
RMSE	Root Mean Square Error
SIC	Sea Ice Concentration
SPNA	Subpolar North Atlantic
SST	Sea Surface Temperature
T_{2m}	Air Temperature at 2 m
THFX	Total Turbulent Heat Flux
T_s	Surface Temperature
WAI	Warm Air Intrusion
z_0	Roughness Length

1 Introduction

1.1 The subpolar North Atlantic

The subpolar North Atlantic Ocean (SPNA) is a key region for the global climate system. It is where warm northward-flowing waters from the Atlantic Ocean meet cold polar airmasses flowing southwards. At the air-sea boundary wind stress and strong gradients in temperature and moisture result in the substantial exchange of momentum, heat and water, modulating oceanic and atmospheric circulation (Buckley & Marshall, 2016). The intermittent discharges of polar air that flow from the frozen land and ice surface, over the marginal ice zone (MIZ), then out over the comparatively warm ocean waters are known as cold-air outbreaks (CAOs). The abrupt change in surface conditions drives a rapid increase in atmospheric boundary layer (ABL) temperature and humidity, with the greatest surface turbulent heat fluxes just downstream of the MIZ where the cold, dry Arctic air first comes into contact with the surface waters (e.g., Brümmer, 1996; 1997; Renfrew & Moore, 1999). Over the SPNA, CAO events predominantly occur during winter (Kolstad et al., 2009) and are responsible for 60% to 80% of wintertime oceanic heat loss through sensible and latent heat fluxes (Papritz & Spengler, 2017). This heat loss to the ABL, along with loss of fresh water by evaporation, makes the surface waters denser and promotes convective overturning due to buoyancy loss. In the SPNA region this densification forms the headwaters of the Atlantic meridional overturning circulation (AMOC; Talley, 1996). This process is vital in driving the global thermohaline circulation, which, in turn, plays a critical role in global climate through the redistribution of heat and nutrients around the Earth's oceans (Schmitz, 1995).

Communication between the ocean and the atmosphere in the North Atlantic, particularly in the subpolar region, has profound effects on weather and climate conditions in northwest Europe. The release of ocean heat into the atmosphere raises climatic air temperatures by as much as 6°C compared to Pacific maritime climates at a similar latitude (Palter, 2015). The weather of northwest Europe is frequently governed by the North Atlantic region, as it lies downwind of the fast-flowing Northern Hemisphere (NH) Polar Jet stream in the upper atmosphere (Hall et al., 2014). The North Atlantic Oscillation (NAO) describes the relative strength of low pressure over Iceland and high pressure over the Azores, and has a strong influence on temperature and precipitation in Europe, as well as North America and northern Asia via teleconnections (e.g., Trigo et al., 2002; Seager et al., 2010; Baek et al., 2017; Yu et al., 2018). The positive NAO phase (NAO+) is associated with a deep subpolar low over Iceland and a strong subtropical high over

the Azores, which result in a stronger jet stream that brings warmer weather with increased precipitation and storminess from the west. The negative NAO phase (NAO-) occurs when the Icelandic Low and Azores high are weaker than average, often with a blocked jet stream, resulting in more northerly winds to northwest Europe that bring colder temperatures and below-average precipitation. The NAO plays a significant role in decadal variability in NH temperature trends and is partly responsible for periods of enhanced warming and periods of seemingly paused temperature increase against the backdrop of anthropogenic climate forcing (Iles & Hegerl, 2017). Shifts in the occurrence of NAO phases have significant implications for air-sea interaction and NH weather, with sea ice loss a key factor (Visbeck et al., 2001; Strong et al., 2009; Delworth et al., 2016). Crucially, the weather and climate of the SPNA are inextricably linked with the AMOC through air-sea interaction, and understanding their relationships in the past, present and future are key to short-range weather forecasting and long-range projections of global climate.

A schematic of the AMOC branches and their pathways around the SPNA is shown in Figure 1.1. The North Atlantic Current (NAC) brings warm saline Atlantic Water (AW) from the subtropical North Atlantic into the region. It branches south of Iceland, with a portion heading west as part of the North Atlantic Subpolar Gyre, densifying on its journey via open-ocean convection in the Irminger and Labrador Seas. The other branches continue north, predominantly through the Faroe-Shetland Channel and over the submarine Iceland-Faroe Ridge into the Nordic Seas basin (encompassing the Norwegian, Greenland and Iceland Seas; Østerhus et al., 2019). In the basin the density of these waters increases, cooling as it flows around the boundary (Mauritzen, 1996), and via convective overturning in the Greenland and Iceland Sea gyres (Swift et al., 1980; Swift & Aagaard, 1981; Marshall & Schott, 1999; Våge et al., 2011). Some AW enters the Barents Sea through the Barents Sea Opening (Loeng, 1991), and the Arctic Ocean through Fram Strait carried by the West Spitzbergen Current (Aagaard et al., 1987). Waters within the Nordic Seas basin become cold and dense, then are transported southward predominantly by the East Greenland Current (EGC) towards the Denmark Strait. This current is then joined by the North Icelandic Jet (NIJ), then exits the basin as Denmark Strait Overflow Water (DSOW; Jónsson, 1999; Jónsson and Valdimarssont, 2004; Harden et al., 2016). Most of the remaining Nordic Seas dense water flows out of the basin to the east of Iceland (Østerhus et al., 2008).

At present, the upstream sources and pathways of the dense waters that form the lower limb of the AMOC are not fully known and remain the subject of debate. The NIJ has been found to contribute the densest third (Harden et al., 2016) or more (Semper et al., 2019) of the DSOW. Its origin was suggested to be the result of an interior overturning loop in the Iceland Sea fed by

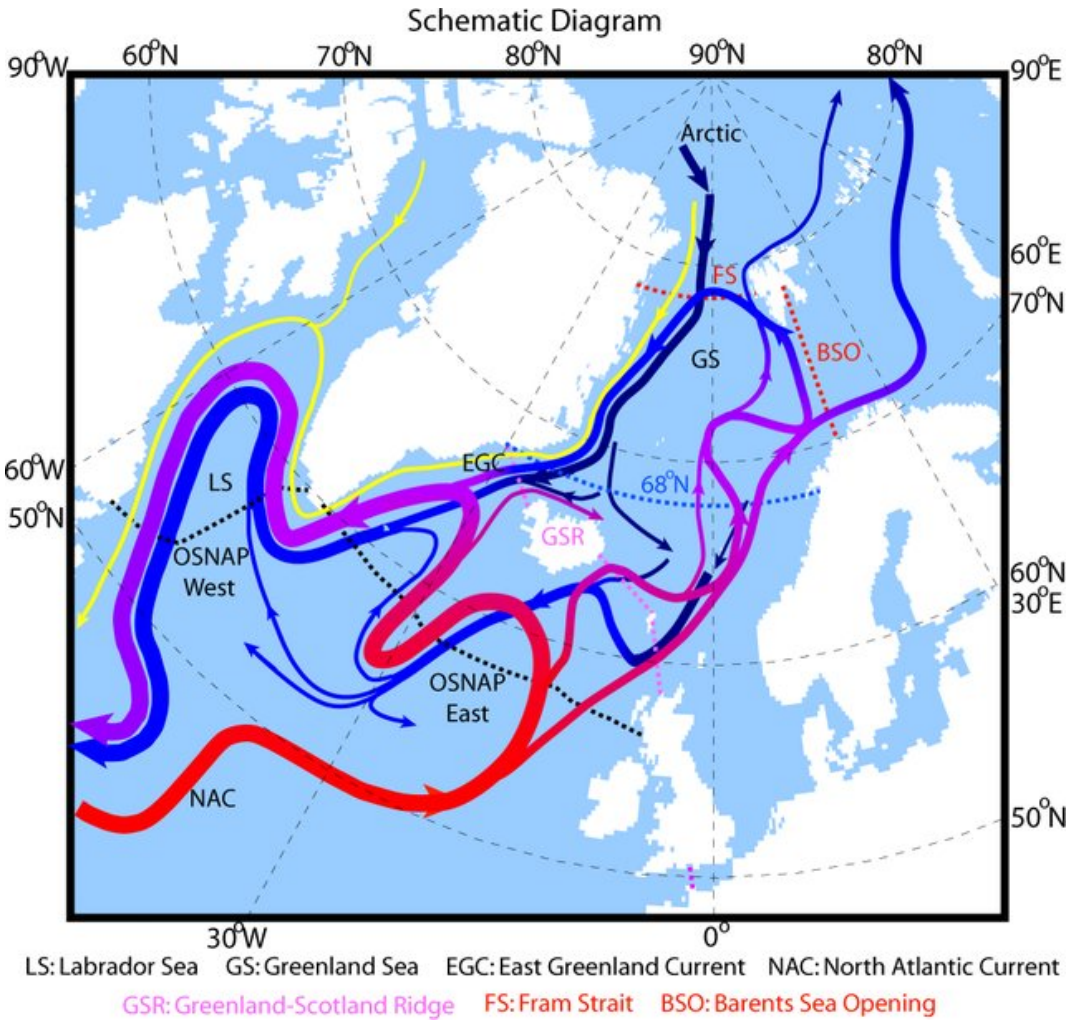

Figure 1.1 Schematic of long-term mean AMOC pathways. Colours of arrows indicate seawater density (light to dense: yellow-red-purple-violet-blue-dark blue). From Zhang & Thomas (2021).

the North Icelandic Irminger Current (Våge et al., 2013; Våge et al., 2015). However, it has been suggested more recently that the origin of the densest portion of the NIJ is the Greenland Sea (Huang et al., 2021), where sufficiently dense waters are regularly formed (Brakstad et al., 2019). DSOW constitutes around half of the outflow crossing the Greenland-Scotland Ridge and supplies the densest water to the Deep Western Boundary Current (Jochumsen et al., 2017; Østerhus et al., 2019). The other main portion of dense water flowing out of the Nordic Seas has only recently been identified as the Iceland-Faroe Slope Jet (Semper et al., 2020), which flows from north of Iceland south-eastwards and out through the Faroe Bank Channel.

Understanding water mass transformation in the SPNA and the atmospheric forcing that drives it continues to be an important topic of research and is a key motivation for this project. Such research feeds into the production of more accurate forecasting systems at short and long range, the need of which is reinforced by a rapidly changing climate. Annual mean Arctic sea-ice area has reduced by around 20% over the period 1979-2014 (Sévellec et al., 2017), and is

projected to continue to decline due to anthropogenic climate change (Notz & Stroeve 2016), with the summertime Arctic possibly ice free within decades from now (Boé et al., 2009; Overland & Wang, 2013). Feedbacks from the loss of sea ice and snow cover on land over the last two decades have contributed to "Arctic amplification", where surface air temperature has increased by more than double the global average (Holland & Bitz, 2003; Hansen et al., 2010; IPCC, 2021). The reduced air-sea temperature gradient and sea ice retreat have resulted in reduced wintertime turbulent heat fluxes in the Iceland and Greenland Seas (Moore et al., 2015) and evidence suggests a slowdown in the AMOC since the mid-20th century has occurred (Rahmstorf et al., 2015; Caesar et al., 2018). Thus, the core aim of the research that comprises this thesis is to improve understanding and numerical weather prediction of air-sea interaction in the SPNA region during CAOs and under the influence of a changing sea ice distribution.

1.2 Cold-air outbreak characteristics

Large fluxes of heat and moisture from the ocean to the atmosphere are characteristic of CAOs (Renfrew & Moore, 1999; Renfrew et al., 2019a). Their pathway typically involves a dramatic change in surface temperature, roughness and moisture availability as the air passes from land or ice to over open water, illustrated in Figure 1.2. The resulting low-level instability drives convection and strong ABL instability, with the ABL deepening with distance downstream (Hartmann et al., 1997). Modification of the ABL is also dependent on the stability at the top of the ABL and the divergence of the large-scale flow (Brümmer, 1996). Papritz & Spengler (2017) provide an analysis of the frequency and intensity of CAOs over the SPNA. They identify CAOs using an index based on the air-sea potential temperature difference, $\theta_{SKT} - \theta$, where θ denotes the potential temperature of an air parcel and θ_{SKT} is potential skin temperature, calculated as:

$$\theta_{SKT} = SKT \left(\frac{p_0}{p_s}\right)^{R/c_p},$$

with p_0 = 1000 hPa, p_s denoting surface pressure, R is the universal gas constant and c_p is the specific heat capacity. Figure 1.3 displays the percentage of time that CAOs occur over the SPNA, binned by their intensity. The most intense CAOs occur due to Arctic outflows through the Fram Strait between the coasts of Greenland and Svalbard, and over the Barents Sea west of Novaya Zemlya. Weaker, more frequent CAOs over the Greenland, Iceland and Norwegian Seas occur due to the underlying SST gradient. Significant CAOs also occur over the more southerly Labrador and Irminger Seas often as a result of airmasses that originate in the Canadian Arctic. Over the

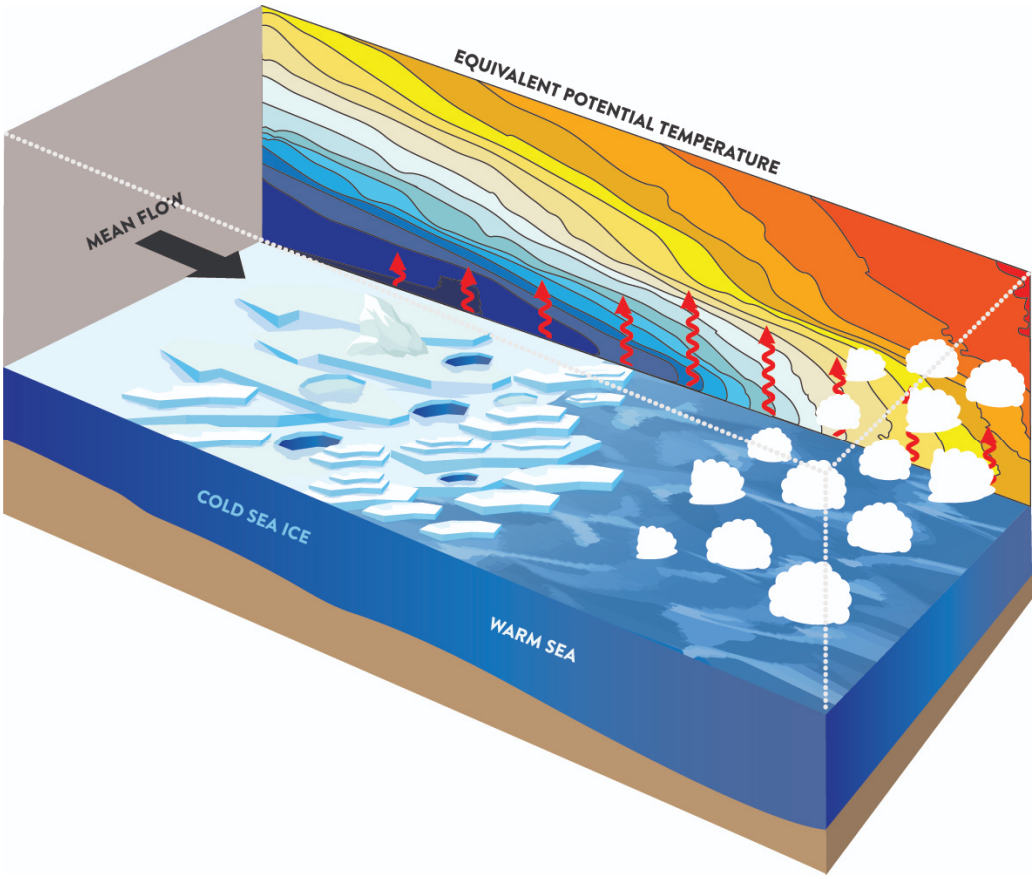

Figure 1.2 Sketch of a cold-air outbreak to illustrate the passage of a cold airmass flowing off the pack ice, over the marginal ice zone and out over the open ocean. Red arrows indicate the intensity of heat and moisture fluxes from the surface to the atmospheric boundary layer (ABL). The background depicts an indicative cross-section of the atmospheric equivalent potential temperature, showing the well-mixed ABL warming and deepening with distance from the ice edge.

Labrador and Irminger Seas it has been shown that CAOs are closely associated with the positive phase of the North Atlantic Oscillation (NAO; Thompson & Wallace, 2001; Claud et al., 2007; Kolstad et al., 2009), while in the Iceland and Greenland Seas CAOs are associated with a negative NAO (Papritz & Spengler, 2017).

CAOs are associated with a range of severe mesoscale weather phenomena, including polar lows, orographically driven low-level jets, roll clouds, Arctic ABL fronts, fog and icing (e.g., Harold et al., 1999; Drüe & Heinemann, 2001; Kolstad et al., 2011; Isachsen et al., 2013; Sergeev et al., 2017). Commonly, the onset of a CAO event is associated with a very cold upper-level trough and the strong baroclinicity and wind shear on the flank of the cool polar air can lead to the spontaneous development of polar mesoscale cyclones (PMCs), often named polar lows when sufficiently intense (Terpstra et al., 2021). Kolstad (2011) showed that CAO intensity and monthly variability largely determined the frequency of occurrence of polar lows.

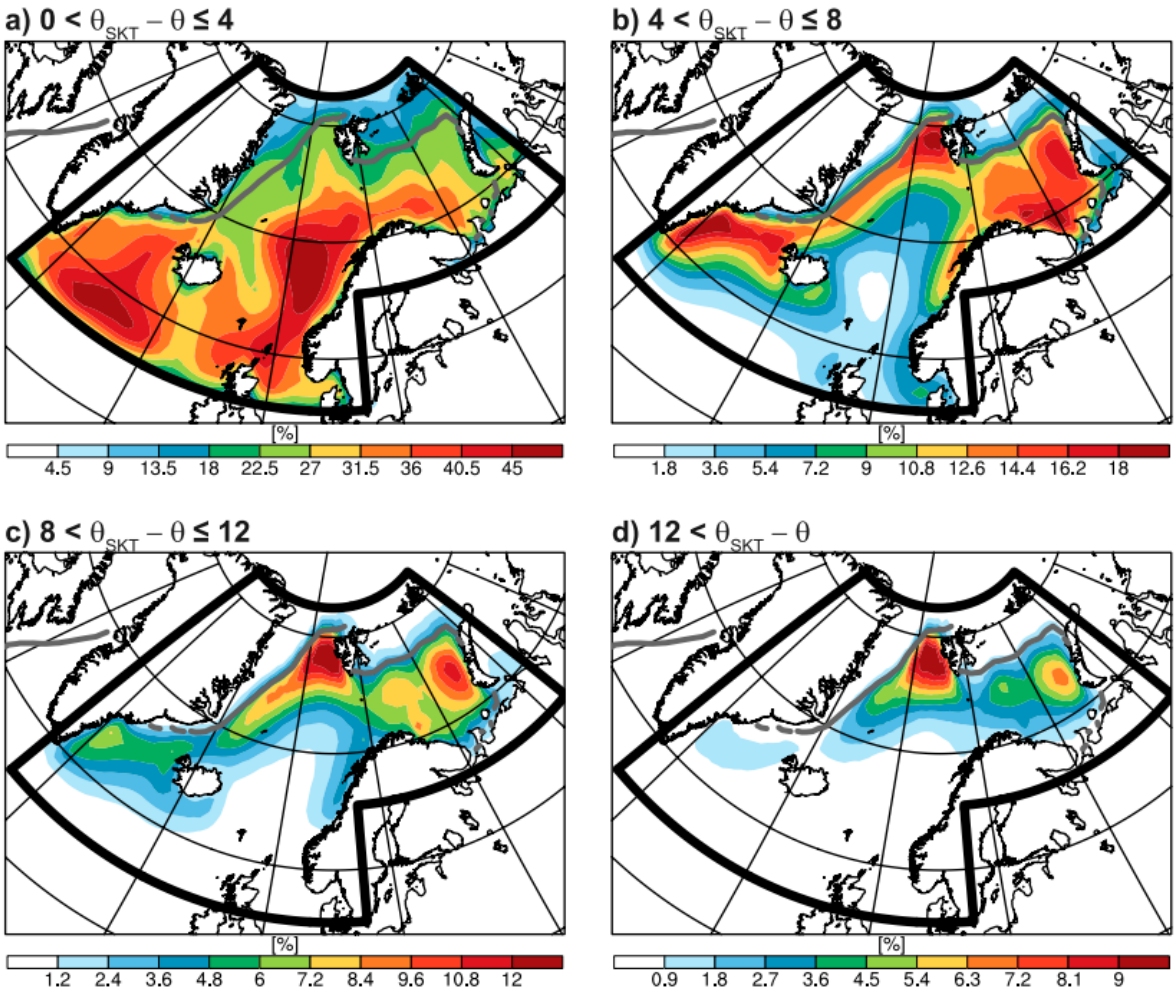

Figure 1.3 Mean frequencies of CAOs (percentage of time during winter that these CAO conditions occur) with trajectories binned according to CAO intensity and aggregated for model timesteps. CAO intensity is identified by the air-sea potential temperature difference $\theta_{SKT} - \theta$. The mean sea ice boundary (50% sea ice concentration) is shown by the grey contour. From Papritz & Spengler (2017).

Surface sensible heat fluxes destabilise the overlying air mass and latent heat fluxes provide further energy to intensify the vortices (Heinemann & Klein, 2003). Most active during winter, they normally have a horizontal scale of less than 1000km and wind speeds are commonly greater than 15 ms^{-1} (Bracegirdle & Gray, 2008). These small but severe storms, with strong winds and heavy precipitation (normally snow or hail), can cause significant socio-economic disruption in the polar maritime regions that impacts human activities, such as tourism, fishing, transportation, natural resource extraction and research activities (Terpstra & Watanabe, 2020). Low-level jets and PMCs are documented to enhance air-sea heat fluxes and ocean heat transport, thereby influencing the AMOC (e.g., Pickart et al., 2003; Condron & Renfrew, 2013; Jung et al., 2014).

Roll clouds, or cloud streets, are quasi-two-dimensional cloud structures that are roughly aligned parallel with the mean wind flow (Atkinson and Zhang, 1996; example in Figure 1.4). They are associated with roll convection and often indicate CAOs with strong air-sea temperature gradients (Brown, 1980). This form of convection comprises substantial vertical transport of momentum, heat and moisture (Etling & Brown, 1993). Roll clouds originate over the MIZ where the ABL first receives an injection of moisture and heat from polynyas and leads in the ice (Renfrew & Moore, 1999; Pagowski & Moore, 2001). Modelling studies have shown that the structure of the MIZ has a crucial influence on the formation of roll clouds and the development of the ABL, particularly due to sea ice inhomogeneities generating uneven heating, wind shear and vortices that induce organised roll convection downstream (e.g., Liu et al., 2004; Liu et al., 2006; Gryschka et al., 2008).

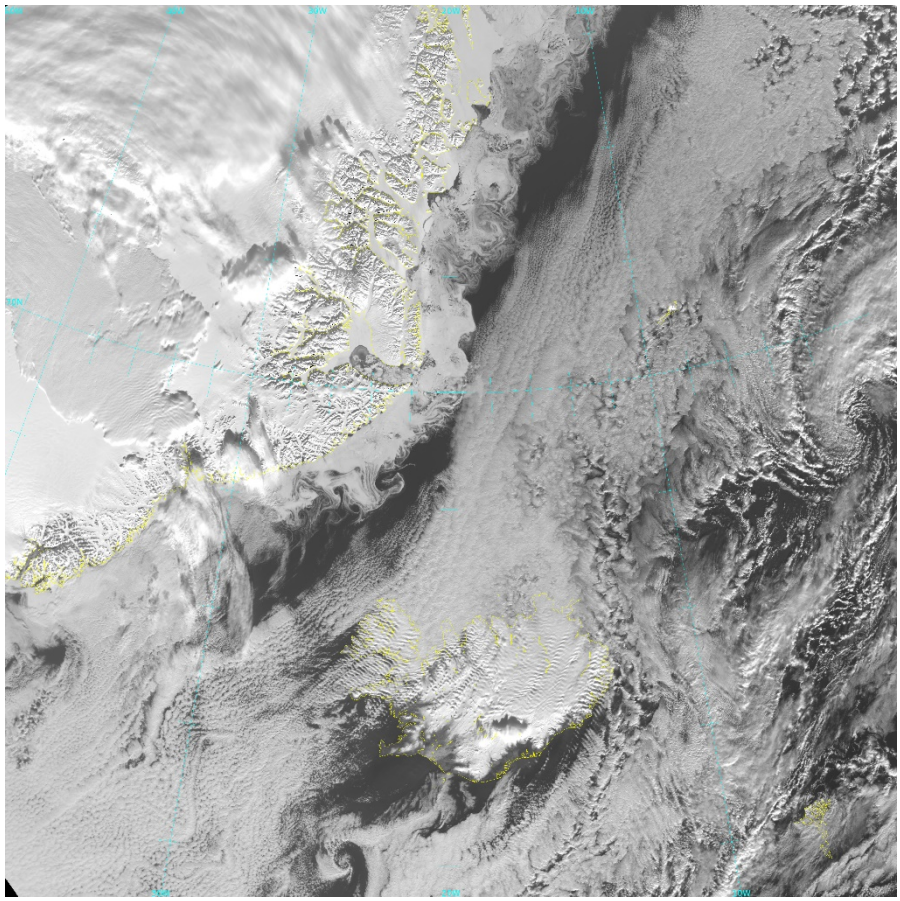

Figure 1.4 Satellite image during a cold-air outbreak over the Iceland and Greenland Seas from the Visible Infrared Imaging Radiometer Suite (VIIRS) on 2 March 2018 12:16 UTC.

1.3 Air-sea interaction and the influence of the marginal ice zone

Surface fluxes at high latitudes play a crucial role in atmospheric, oceanic and cryospheric processes. In the SPNA strong turbulent heat fluxes occur, occasionally exceeding 500 Wm^{-2} in measurements (e.g., Shapiro et al., 1987; Renfrew & Moore, 1999) and simulations (e.g., Wacker et al., 2005; Spensberger & Spengler, 2021). In Figure 1.5, climatological winter mean (DJFM; 1979-2012) turbulent heat flux over the entire SPNA region are shown to be positive (from ocean to atmosphere) in the European Centre for Medium-Range Weather Forecasts (ECMWF) Interim Reanalysis (ERA-I; Moore et al., 2012). Local maxima of over 200 Wm^{-2} occur just off the ice edge in the Labrador Sea and at the exit of Fram Strait in the northern Greenland Sea. This spatial distribution of heat fluxes corroborates the CAO distribution shown in Figure 1.2. Most striking is the local minimum in the Iceland Sea. This minimum is partly explained by the ocean temperature, with the Iceland Sea being a region of relatively cold SSTs due to water that spreads eastward from the EGC via the East Icelandic Current (Jónsson, 2007).

However, as Moore et al. (2012) show, the Iceland Sea minimum in winter mean turbulent heat fluxes is collocated with a saddle point in sea-level pressure between the Icelandic and Lofoten Lows, illustrated in Figure 1.6. The oscillation between these two climatological lows acts to modulate ocean-atmosphere heat fluxes in this region, demonstrated by compositing mean sea level pressure for the 10^{th} and 90^{th} percentiles of turbulent heat fluxes over the Iceland Sea, shown in Figures 1.6a and 1.6b respectively, which can be directly related to the phases of the NAO. Low monthly mean total turbulent heat fluxes over the Iceland Sea are associated with a deeper than usual Icelandic Low (NAO+) and more intense cyclonic atmospheric circulation. This brings a stronger southerly flow with warmer air temperatures over the Iceland Sea, often named a warm air intrusion (WAI), while enhancing heat fluxes over the Labrador Sea with a stronger north-westerly flow. Conversely, high heat flux events over the Iceland Sea (e.g., Harden et al., 2015) are typically associated with a weaker than usual Icelandic Low (NAO-) and a stronger Lofoten Low, which brings more pronounced northerly flow into the Nordic Seas but weaker north-westerly flow over the Labrador Sea.

The off-ice wind flow during CAOs and the air-sea fluxes downstream of the ice edge are strongly influenced by the characteristics of the marginal ice zone (MIZ) - the band of partially ice-covered water that separates the main ice pack from the open ocean. The MIZ distribution affects the wind, temperature, humidity, surface fluxes and cloud over the MIZ and downstream (e.g., Gryschka et al., 2008; Chechin et al., 2013; Renfrew et al., 2021). The MIZ is dynamic, responding to wind, ocean currents and waves over a range of spatial scales (Notz, 2012; Kohout et al., 2014). Sea ice conditions over the SPNA have been rapidly changing over the last 50 years.

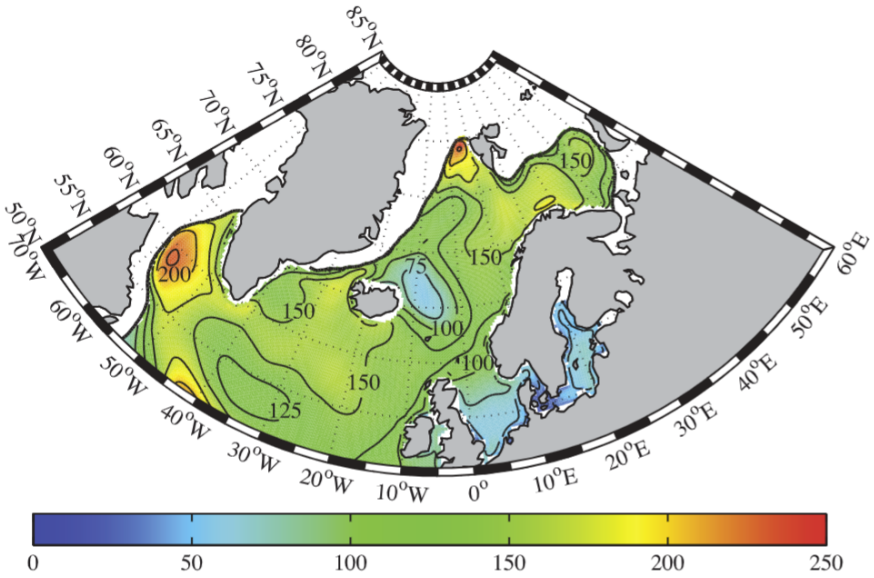

Figure 1.5 Winter mean (DJFM) climatology of the total turbulent heat flux (Wm^{-2}, contours and shading) from ERA-I 1979-2012. The thick black line represents the 25% winter mean ice concentration contour. From Moore et al. (2012).

For example, in the Iceland and Greenland Seas the sea ice edge has retreated coastwards since the 1970s. Before this time the sea ice edge, hence the area of greatest air-sea heat fluxes, typically lay in the vicinity of the Iceland and Greenland Sea gyres (Moore et al., 2015). These gyres facilitate ocean convection; they provide a preconditioned environment, with domed isopycnals due to the cyclonic flow, that lead to a weakly stratified mid-depth water column, which in turn promotes convection to greater depths (Swift & Aagaard, 1981; Voet et al., 2010).

Over the Iceland and Greenland Seas this sea ice loss is linked to a reduction in air-sea heat fluxes of around 20% since 1979, and modelling suggests that further reductions may decrease the supply of dense waters to the AMOC (Moore et al., 2015). Furthermore, the Arctic Ocean and the Nordic and Barents Seas have significantly warmed since the 1970s, with increased ocean heat transport into the region partly responsible for the loss of sea ice (Smedsrud et al., 2021; Tsubouchi et al., 2021). Over the coming decades the summertime Arctic is projected to continue warming and transition to a "New Arctic", where sea ice conditions over the entire region will become analogous to the MIZ (Sigmond et al., 2018). The Arctic Ocean and subpolar seas warming and becoming more like the Atlantic inflow is often termed "Atlantification" (e.g., Asbjørnsen et al., 2020), with significant effects on ecosystems (Ingvaldsen et al., 2021). The fundamental role that the MIZ plays in air-sea interaction in the SPNA region, and the rapid change in MIZ characteristics underway, makes it a key feature of this research.

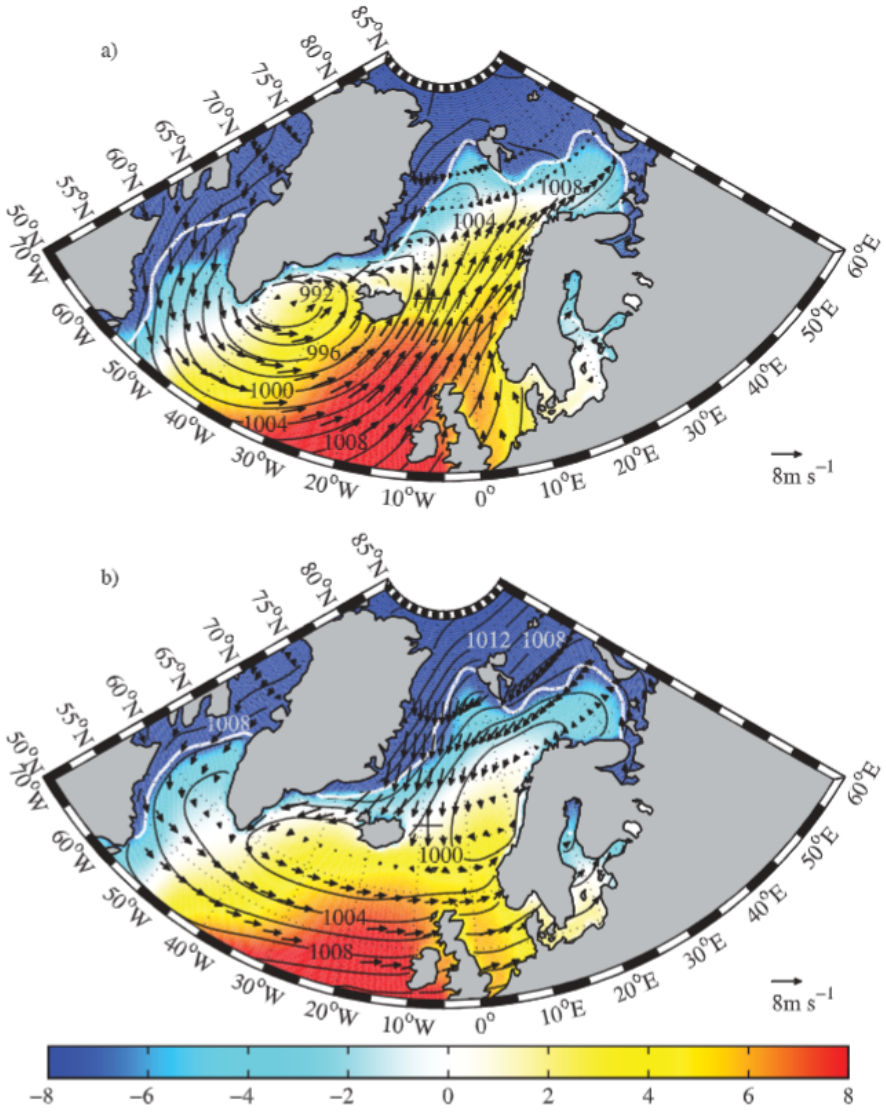

Figure 1.6 Composite monthly mean sea level pressure (mb, contours); 10 m wind (ms^{-1}, vectors) and 2 m air temperature (°C, shading) for winter months during which the total turbulent heat flux at the Iceland Sea site (marked with '+') is in the a) 10^{th} or b) 90^{th} percentile. The thick white line represents the 25% winter mean ice concentration contour. From Moore et al. (2012).

1.4 Numerical weather prediction systems and ocean-ice-atmosphere coupling

The important role that CAOs play in weather conditions at a range of scales, particularly the risk of dangerous or damaging mesoscale phenomena, along with the impacts of air-sea exchange on the global climate, make their accurate simulation in numerical weather prediction models (NWP) essential. The retreating sea ice also presents new opportunities in the Arctic, driving socio-economic interests in the region that demand accurate forecasts (Emmerson & Lahn, 2012; Jung et al., 2016). However, the remote, harsh environment of the high latitudes makes observational platforms difficult and expensive to operate. This problem is exacerbated

over sea ice and the MIZ, which has resulted in deficiencies in characterising these areas and their poor representation in weather and climate models. For example, simulation of air-sea interaction is typically hampered by surface exchange parameterisation schemes that poorly estimate surface drag (e.g., Elvidge et al., 2016; Renfrew et al., 2019b; Elvidge et al., 2021) and poor ABL parameterisations (e.g., Boutle et al., 2014; de Roode et al., 2019; Forbes & Ahlgrimm, 2014). As a result, substantial biases in surface fluxes over the MIZ are common and can extend for hundreds of kilometres downstream (Bourassa et al., 2013).

An example of how the representation of the MIZ can influence simulated meteorological variables is shown in Figure 1.7, in an evaluation of ECMWF's 5th reanalysis (ERA5) surface layer temperature, wind speed and direction, and sensible heat flux with aircraft observations. The overly smooth distribution of sea ice, an artefact of the satellite product used to initialise the model, leads to similarly weak gradients in the meteorological variables (Renfrew et al., 2021). The result is the same when evaluating a high-resolution (2.2 km) Met Office Unified Model (MetUM) product initialised using sea ice data from the same origin as ERA5 (Renfrew et al., 2021), highlighting the potential error introduced into NWP simulations by a poor representation of sea ice across all ranges of prediction.

A key tool to overcome these issues is to use NWP models that feature air-sea-ice interaction. A leading example is the European Centre for Medium Range Weather Forecasts' (ECMWF) Integrated Forecast System (IFS) high resolution global forecasts (HRES), which since June 2018 (IFS Cycle 45r1) have benefited from dynamic and thermodynamic coupling between sea ice, ocean and atmosphere. Evaluation using this model has demonstrated that the assumption of persistent sea ice is detrimental to medium-range predictions of sea ice and local 2 m temperature (Keeley & Mogensen, 2018). The Met Office's global operational forecast system remains atmosphere only, though work to transition to a coupled model configuration is underway with planned global coupled operational forecasts planned in 2022. Thus, another key aim of this research project is to evaluate experimental Met Office coupled models, feeding into the development of more accurate weather forecasts in the high latitudes.

The effects of sea ice loss in projections of future climate are best simulated in coupled models. Recent improvements of long-range projections have been made in the Coupled Model Intercomparison Project Phase 6 (CMIP6; Eyring et al., 2016). Projected change in Arctic sea ice area from this ensemble, for low, medium and high greenhouse gas emissions scenarios, is illustrated in Figure 1.8. These projected time series show the clear relationship between growing emissions, increasing global mean surface temperature and decreasing sea ice cover in

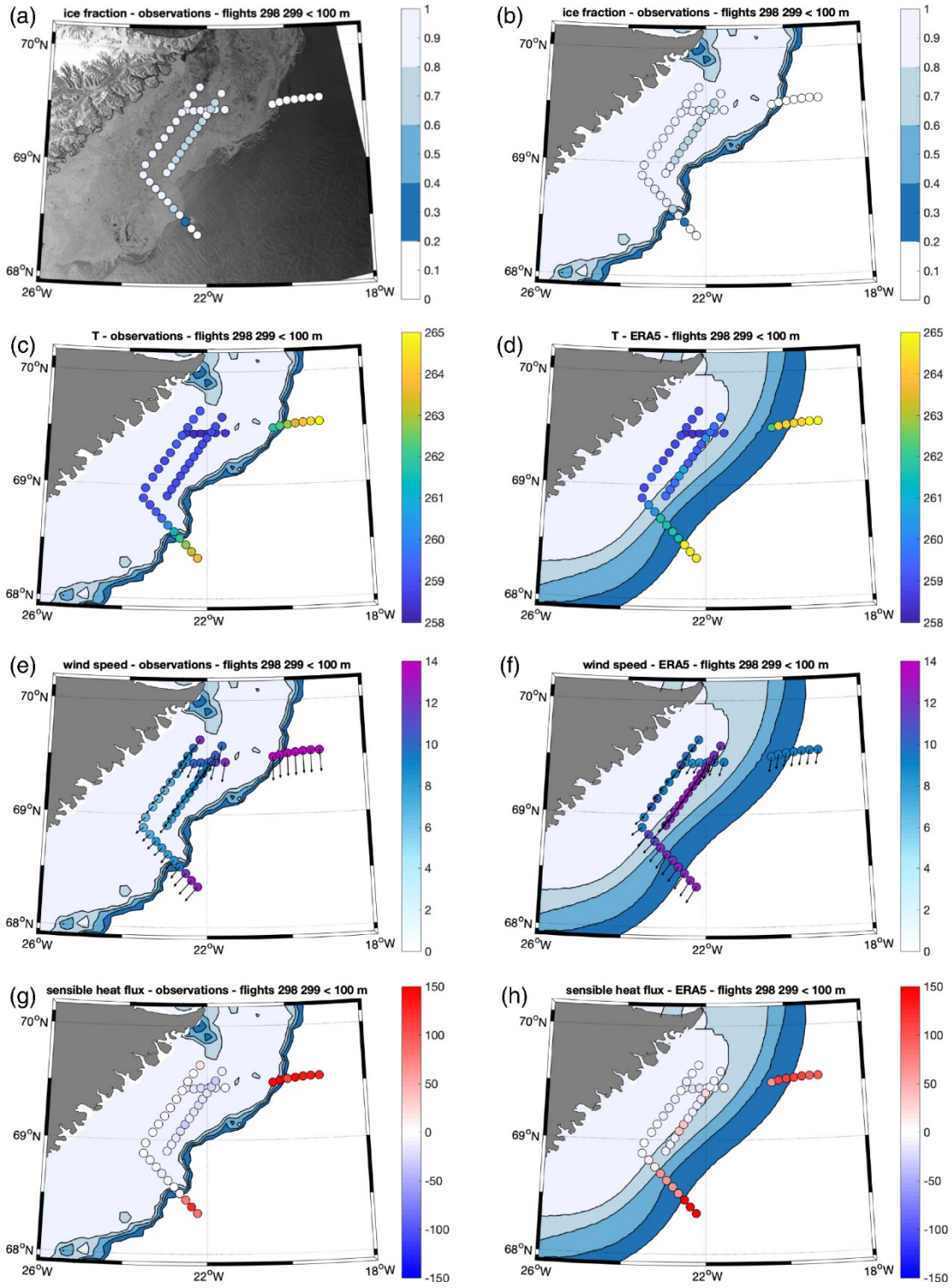

Figure 1.7 Observations from two science flights over the Iceland Sea marginal ice zone overlaid on a SAR satellite image, a), or AMSR2 sea ice analysis from the same day b), c), e) and g); and simulated values in ERA5 over OSTIA sea ice, d), f) and h) (c.f. Renfrew et al., 2021).

the Arctic. In winter, sea ice area is projected to continue to slowly decline then level off to 2100 under the lower emissions scenarios, however under the high emissions scenario it is suggested that ice area fall by at least 50%. However, in summer a drastic change in sea ice conditions is anticipated, with the Arctic predicted to become near or completely ice free by the end of the

21st century. A set of separate coupled model experiments suggests a weakening of the Icelandic Low and a southward shift of mid-latitude westerly winds in winter with future reductions in Arctic sea ice, though the response in atmospheric circulation is sensitive to the magnitude and geographic pattern of sea ice loss (Screen et al., 2018). The critical importance of the projected changes to the Arctic and the SPNA climate system, and the global implications, motivate the final key aim of this thesis, which is to analyse the changes in air-sea interaction for the SPNA region in CMIP6 projections.

1.5 Thesis aims and structure

The core aim of the research that comprises this thesis is to improve understanding of the physical air-sea interactions during cold-air outbreaks over the subpolar North Atlantic, including the influence of the marginal ice zone, and inform the simulation of these relationships in numerical weather prediction models. This will be carried out through careful investigation of short-range coupled model forecasts using a case study-based approach and analysis of state-of-the-art long-range climate projections.

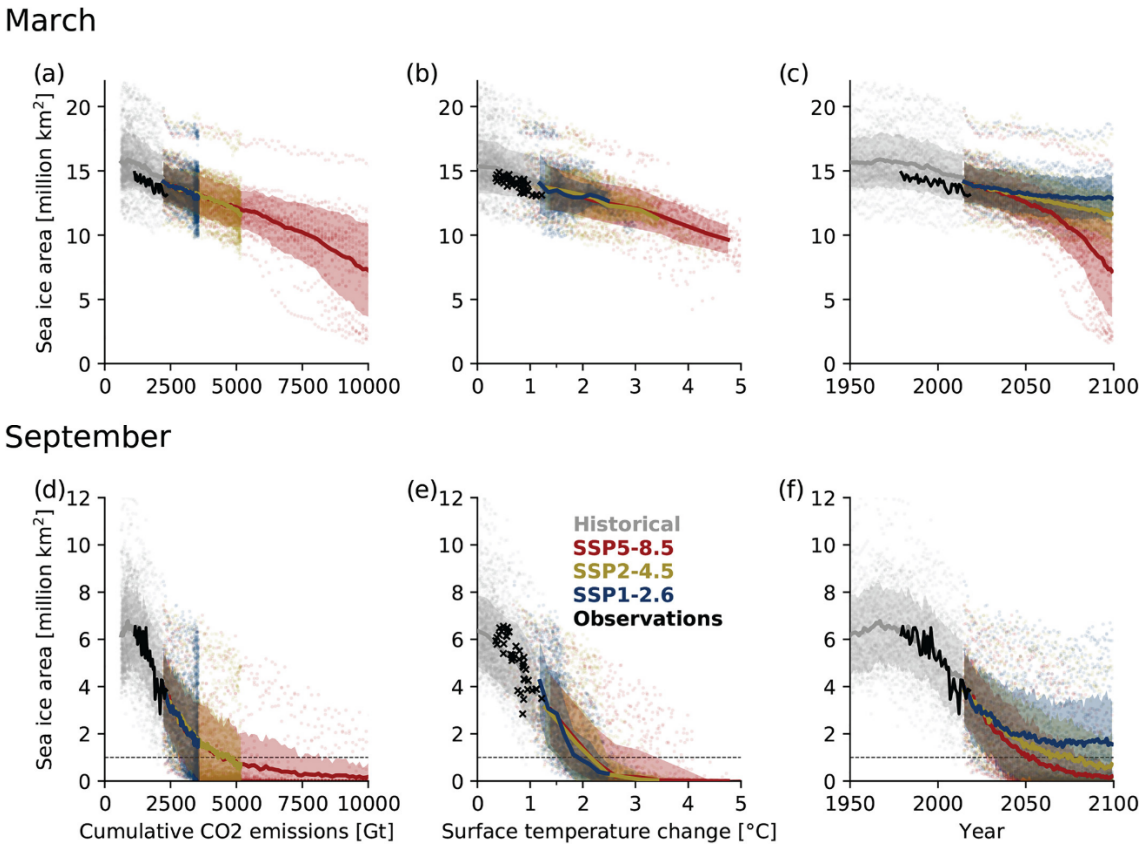

Figure 1.8 Projections of Arctic sea ice change from the CMIP6 ensemble in a) - c) for March and in d) - f) for September. These projections are displayed as a function of cumulative anthropogenic CO_2 emissions in a) and d); global mean annual surface air temperature change in b) and e); and years over the 21st century in c) and f). From Notz et al. (2020).

This is facilitated in part by the use of detailed observations made during the Iceland-Greenland Seas Project (IGP) field campaign that took place in 2018. This project comprises coupled atmosphere and ocean measurements made by a research vessel, an aircraft, ocean gliders, a meteorological buoy and an ocean mooring (c.f. Renfrew et al., 2019a). The majority of these observations were collected in the vicinity of the MIZ, enabling analysis of its impact on simulated surface layer meteorology in models.

This thesis aims to:

- Detail the collection and quality control of ship-based meteorological observations during the Iceland Greenland Seas Project (IGP) field campaign.
- Use the diverse set of IGP observations made during cold-air outbreaks to evaluate pseudo-operational forecasts from the Met Office Global Coupled model 2 (GC2) and compare with operational (uncoupled) forecasts to determine whether air-sea-ice coupling provides improvements in forecast skill.
- Evaluate sea ice forecasts in the Iceland and Greenland Seas from the Met Office Global Coupled model 3 (GC3) in several configurations that experiment with ocean model resolution and parameterisation of surface drag over the marginal ice zone.
- Investigate the projected changes in sea ice and air-sea interaction in the subpolar North Atlantic region over the 21st century with climate change using output from the HadGEM3-GC3.1 climate model.

In summary, Chapter 2 will provide a detailed description of the IGP observations utilised in this research project, including the process of calibration and quality control applied to the ship-based meteorological data, and outline some of the characteristics of CAOs observed during the IGP campaign. Also, background information on the NWP output used in this project will be presented. In Chapter 3 an evaluation of short-range predicted surface meteorology in the Met Office's Global Coupled model version 2 (GC2) is carried out using the IGP observations in several case studies through comparison with the atmosphere-only Met Office operational forecast product, enabling discussion on the advantages and disadvantages of the dynamic MIZ in the GC2 forecasts. Following the evidence from Chapter 3 that accurate simulation of the MIZ is crucial to the success of a coupled model, Chapter 4 presents results from an in-depth evaluation of the simulated MIZ in short-range forecasts from the improved Met Office Global Coupled model version 3.1 (GC3.1), performed as the updated model output became available. Quantification of model skill is performed with the Integrated Ice Edge Error metric (IIEE; Goessling et al., 2016), using two satellite sea ice products for verification. Chapter 5 then builds

on the understanding developed in the earlier chapters, with analysis of the climate scale HadGEM3-GC3.1 model configurations and their projections for air-sea interaction in the subpolar North Atlantic region over the course of the 21st century. It is shown that the rapid decline of winter sea ice and reducing air-sea temperature gradients under anthropogenic climate change will likely have significant impacts on atmospheric and oceanic circulation that affect the weather of north-western Europe and the global climate.

2 Observational data collection and processing

The first six months of my PhD were centred on the Iceland Greenland Seas Project (IGP). Alongside the typical period of learning and the development of research skills, my activities included attending project planning meetings at British Antarctic Survey and the Met Office; contacting suppliers and assisting the purchasing of scientific consumables; training on the operation and maintenance of instruments at the National Centre for Atmospheric Science; and the preparation of equipment and shipping. I then took part in both legs of the field campaign aboard the Research Vessel Alliance, releasing radiosondes, making measurements, maintaining equipment, relaying forecasts to the crew and assisting the planning of science activities, and coordinating with the aircraft team. Subsequently, my work has been heavily involved in the IGP project, from the initial data processing and quality control to collaboration with IGP partners on a range of research projects, including a five week visit to the University of Bergen. The skills and understanding that I developed through my involvement with IGP made me well placed to take on a research associate position for the project, so for 15 months (February 2020 to April 2021) I worked part-time in this role (0.5 FTE) while continuing the PhD part-time. My involvement in the IGP project included contributions to several research papers: *'The Iceland Greenland Seas Project'* (Renfrew et al., 2019a); *'An evaluation of surface meteorology and fluxes over the Iceland and Greenland Seas in ERA5 reanalysis: The impact of sea ice distribution'* (Renfrew et al., 2021); '*A ship-based characterization of coherent boundary-layer structures over the lifecycle of a marine cold-air outbreak'* (Duscha et al., 2022); and '*Coupled atmosphere-ocean observations of a cold air outbreak and its impact on the Iceland Sea*' (Renfrew et al., 2022).

2.1 The Iceland-Greenland Seas Project

2.1.1 Overview of operations

The Iceland-Greenland Seas Project (IGP) field campaign took place during February and March 2018 to investigate the atmospheric forcing and the ocean response in the Iceland and Greenland Seas. Importantly, how wintertime cold-air outbreaks (CAOs) near the marginal ice zone (MIZ) affect ocean heat loss and the generation of dense water masses that feed into the Atlantic meridional overturning circulation (AMOC). Coordinated atmosphere and ocean measurements were made by a range of observing platforms aiming to characterise coupled air-sea processes (Figure 2.1). The NATO Research Vessel *Alliance* left Reykjavik on 6 February to

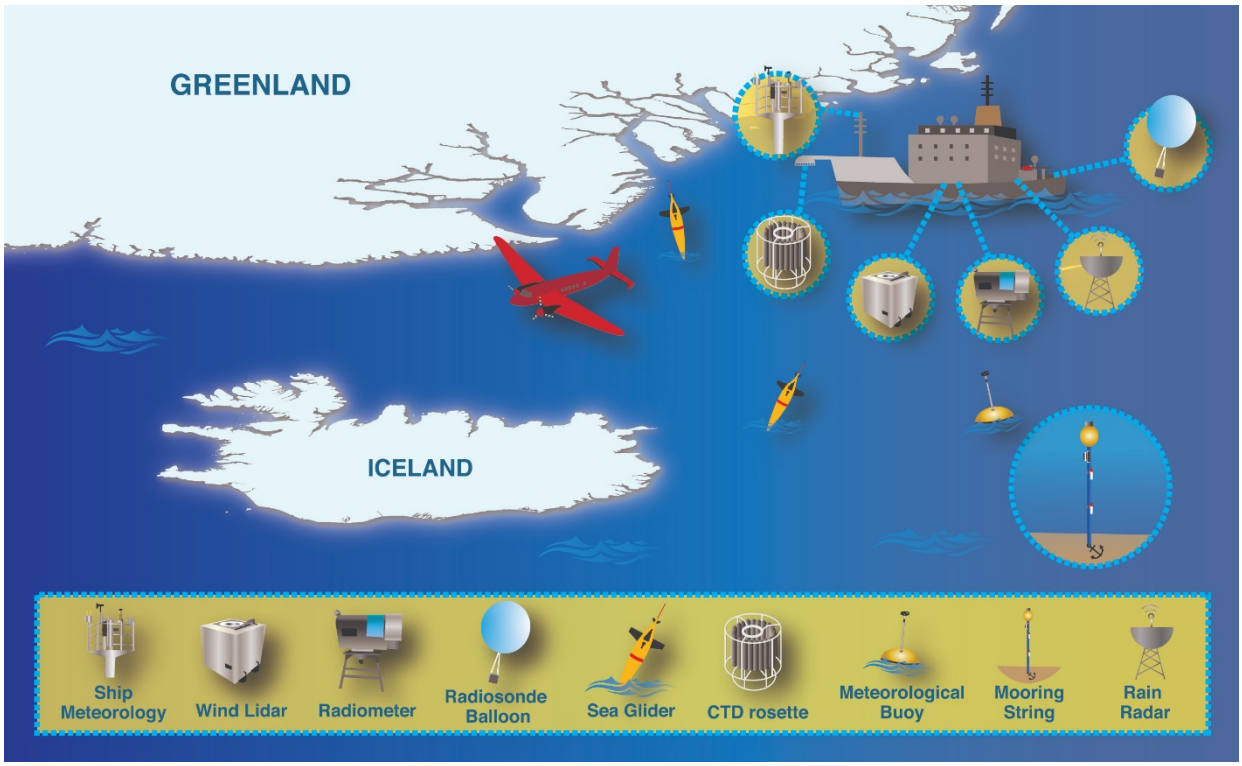

Figure 2.1 Schematic of the key observational platforms deployed as part of the Iceland-Greenland Seas Project.

carry out a 43-day research cruise in two legs to collect a suite of meteorological measurements while surveying the ocean hydrographic structure. The ship's track is displayed in Figure 2.2 and the onboard meteorological instruments are illustrated in Figure 2.3. A meteorological buoy was deployed, collocated with a previously installed mooring, and two ocean gliders were also utilised. From 28 February, British Antarctic Survey's DH6 Twin Otter instrumented research aircraft began operations, flying 14 science missions. In the Iceland Sea region, the ship and the aircraft were coordinated to allow simultaneous sampling of the ocean and the atmosphere and their interactions, providing a rare and rich data set. Following is a brief description of the key instruments from which observations are used in this study (see Table 2.1 and photos in Figure 2.4). Further background and details can be found in Renfrew et al. (2019a), while field campaign operations and technical information are described in the ship and aircraft field campaign reports (available at web.whoi.edu/all0118/).

2.1.2 Instrument description

Radiosondes

Radiosonde launches were a key component of the meteorological campaign. They provide reliable high-resolution profiles of the atmosphere to an altitude of around 25 km. We released a total of 100 radiosondes, providing a minimum of one daily launch and high-frequency

soundings (up to 3-hourly) during “interesting” weather or in coordination with the research aircraft. For example, for 48 hours during the onset and development of a CAO from 28 February radiosondes were launched every 3 hours. All sounding data was uploaded in ‘BUFR’ format to the World Meteorological Organisation’s Global Telecommunication System to be available for operational forecasting. Most of the soundings were assimilated by ECMWF for operational forecasting, shown by regular checks on the European Meteorological Network’s E-ASAP service (see www.eumetnet.eu) during the campaign. Several of the early radiosondes weren’t assimilated due to errors in the BUFR files, which I fixed through correspondence with Met Office colleagues.

The Vaisala RS41-SG radiosondes collect high-resolution temperature, humidity, pressure and wind measurements. Wind, height and pressure data are resolved from the radiosonde’s GPS data combined with differential corrected GPS data from the Vaisala MW41 ground station aboard the ship. Balloon preparation and release took place on the boat deck, with the ground station located in a container (Figure 2.3). The system’s height above mean sea level and its height difference with the antennae, launch position, and barometer are all adjusted parameters for the operational set up. Preparation of each radiosonde for launch included an automatic physical zero humidity check and an in-built functional temperature check. For each sounding initial surface values were entered using other instruments on the ship; however, we were forced to change the source of input data several times due to instrument failures. We released the balloons from the boat deck from the port or starboard side depending on wind direction, occasionally needing to request the captain turn the ship to guarantee a safe launch. Being constantly secured via a safety harness during each launch was essential due to the dangers of an icy deck, high sea states and winds regularly around 30-40 knots.

Hatpro Radiometer

The RPG Hatpro Radiometer provides a continuous characterisation of the atmospheric boundary layer (ABL). Profiles of atmospheric temperature and humidity are measured approximately every 10 minutes providing relatively high temporal resolution observations to accompany the radiosondes, though with lower accuracy. The passive radiometer measures the atmospheric microwave emission at different pressure levels using two frequency bands where the atmospheric opacity is high. Atmospheric water vapor information is derived from 7 frequency channels in the range of 22-28GHz, while temperature distribution is resolved from 7 channels within the oxygen absorption complex in the range of 51-58GHz.

The Hatpro also features a basic surface meteorological package recording barometric pressure, relative humidity and temperature. To enable the Hatpro to reliably make measurements of different pressure levels aboard a moving ship the unit was seated on a single axis motion-

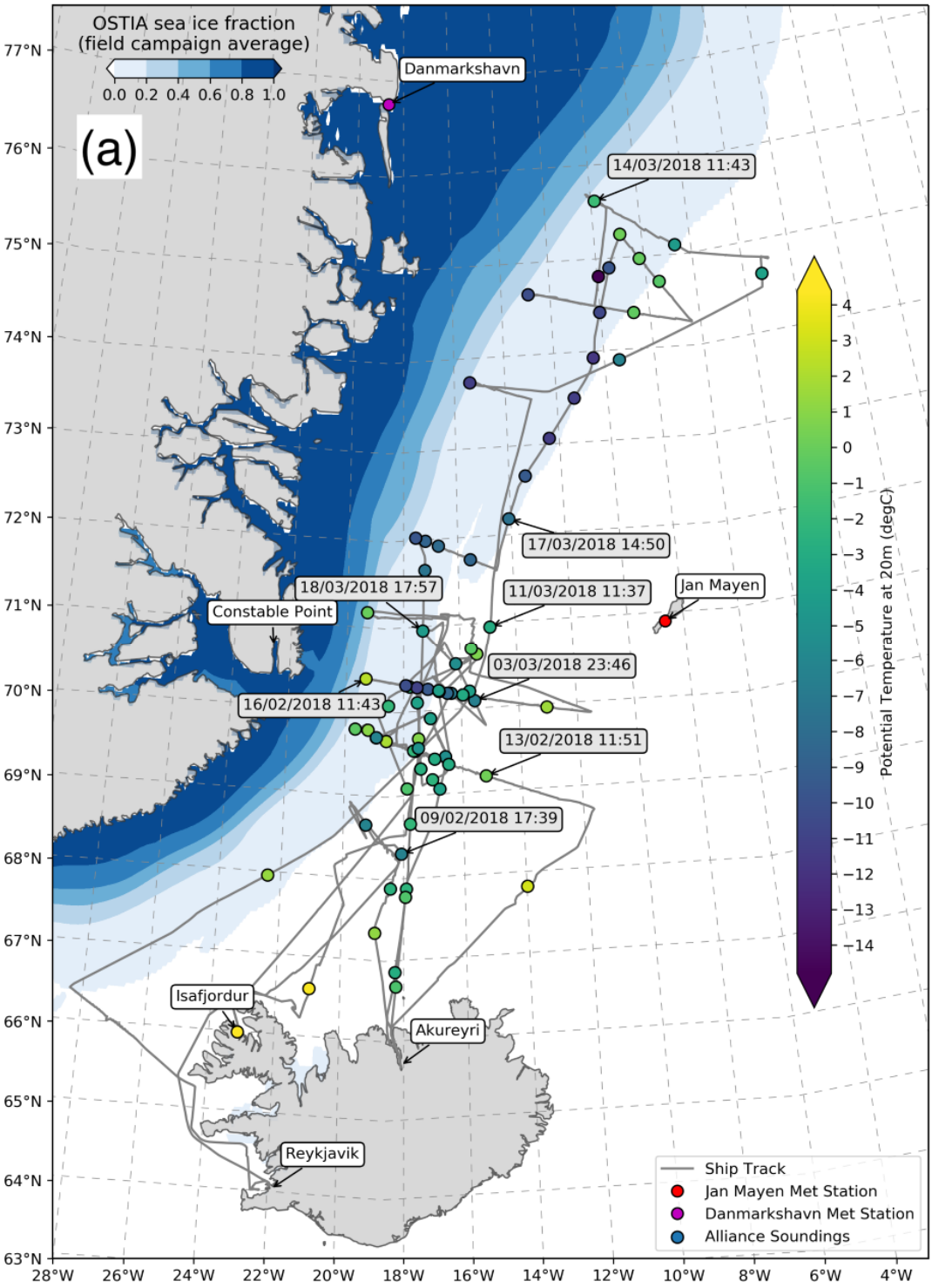

Figure 2.2 The track of the *Alliance* research vessel (grey) during the IGP field with radiosonde locations, which are shaded by the low-level potential temperature. Average sea ice fraction is displayed by the blue shading, using the Met Office Operational Sea Surface Temperature and Sea Ice Analysis (OSTIA).

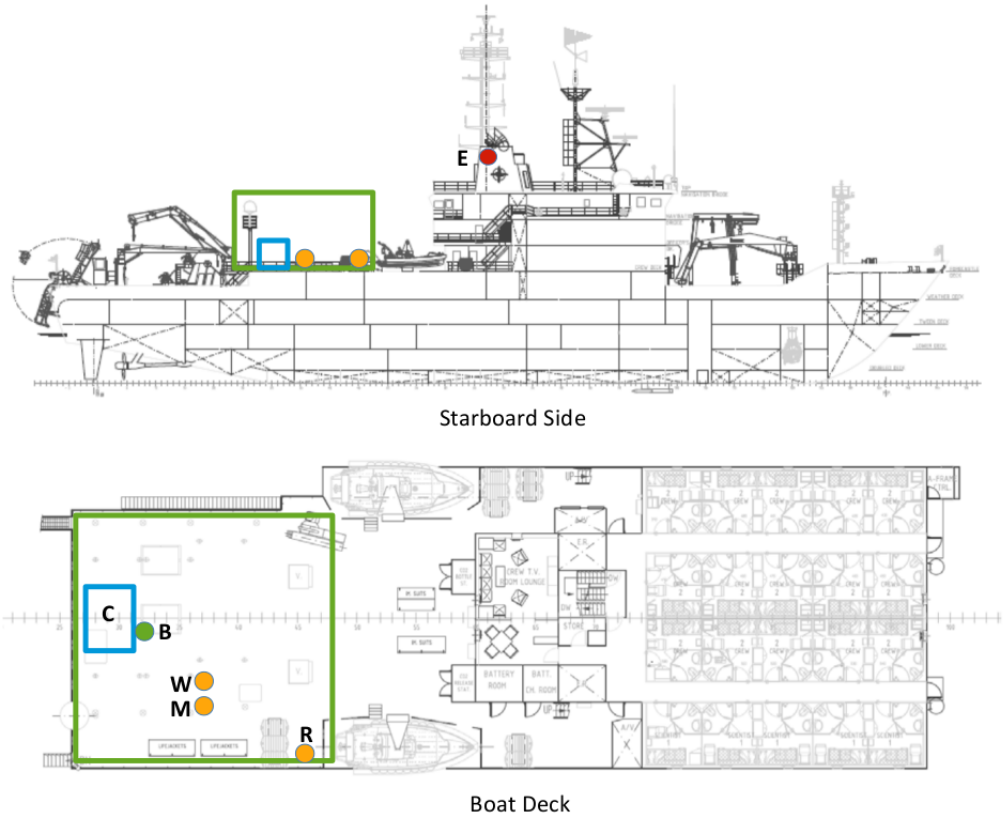

Figure 2.3 Instrument locations on the Alliance. C: Container, B: Balloon basket, R: Hatpro radiometer, W: Windcube lidar, M: Micro Rain Radar, E: Exhaust stack.

correction cradle (following Achtert et al., 2015). Known as the Stable Table, this detects the roll of the ship and produces movement in the opposite direction to maintain a horizontal planning for atmospheric scanning. Using accelerometers and gyroscopic sensors it can sample and correct for the roll of the ship at 10 Hz. The Hatpro was located on the boat deck, near the starboard rail. This provided a clear view for the instrument's selected operational scanning angle between 5° and zenith. Occasionally during the cruise, the Stable Table software crashed (often the result of large waves causing severe roll) resulting in the table being locked in one position until reset.

Windcube lidar

Vertical wind profiles (40-200 m) were measured by the Leosphere Windcube lidar (light detecting and ranging) instrument. The lidar produces successive pulsed infrared laser beams in cardinal directions within a 28° scanning cone, followed by a fifth vertical beam. The laser pulses are backscattered by aerosol particles in the air, such as water droplets or dust, that move with the wind. The collected backscattered light allows for a calculation of wind speed and direction using Doppler induced wavelength shift.

Platform	Instruments	Variables	PI
	Ocean observations		
R/V *Alliance*	CTD, XCTD, XBT,	*T*, *S*, *p* (O_2 CTD only)	R. Pickart, WHOI
	Vessel-mounted ADCP systems	*u*, *v*	R. Pickart, WHOI
	Water intake	SST	R. Pickart, WHOI
	Water sampling—geochemical tracers and isotopes	Nutrients, O_2, CFCs, and SF_6	E. Jeansson, NORCE
		$H_2{}^{18}O$, HDO	H. Sodemann, UiB
	Microstructure glider	Turbulence	S. Waterman, UBC
	Argo floats	*T*, *S*, *p*, *u*, and *v* (from drift)	K. Våge, UiB
Mooring	CTD, *T* recorder, ADCP, RCM	*T*, *S*, *p*, *u*, *v*	K. Våge, UiB
Seagliders	CTD, oxygen	*T*, *S*, *p*, O_2, *u*, and *v* (from drift)	K. Våge, UiB
	Atmospheric observations		
R/V *Alliance*	Wavepak Vessel-mounted meteorology	*T*, *p*, RH, *u*, *v*,	I. Renfrew, UEA
	Vaisala MW41 Radiosonde system*	*T*, *p*, RH, *u*, *v*	I. Renfrew, UEA
	HatPro radiometer	T, RH, LWP	I. Renfrew, UEA
	+ Motion correction platform	+ motion	I. Brooks, ULeeds
	Leosphere Windcube lidar	*u*, *v*, *w*, turbulence	J. Reuder, UiB
	Metek Micro Rain Radar	PPN rate, LWC	H. Sodemann, UiB
	Picarro L2130-i Isotope Spectrometer	$H_2{}^{18}O$, HDO of water vapor	H. Sodemann, UiB
	Precipitation sampling	$H_2{}^{18}O$, HDO	H. Sodemann, UiB
DH6 Twin Otter	Aircraft-mounted meteorology	*T*, *p*, T_{dew}, T_{sfc}, SW, LW	T. Lachlan-Cope, BAS and I. Renfrew, UEA
	BAT turbulence probe and LICOR	*u*, *v*, *w*, *T*, *q*, turbulent fluxes	T. Lachlan-Cope, BAS and I. Renfrew, UEA
	DMT Cloud, Aerosol and PPN Spectrometer	Aerosol and PPN spectra, LWC	T. Lachlan-Cope, BAS and I. Renfrew, UEA
	Grimm spectrometer	Aerosol spectra	T. Lachlan-Cope, BAS and I. Renfrew, UEA
	Picarro L2130-i Isotope Spectrometer	$H_2{}^{18}O$, HDO of water vapor	H. Sodemann, UiB
Meteorological buoy	Seawatch Wavescan Buoy*	T, RH, *u*, *v*, SST, SW, ocean currents	J. Reuder and E. Kolstad, UiB

Table 2.1 A summary of the IGP observations. Variables measured are *T* = temperature; *S* = salinity; *p* = pressure; O_2 = oxygen; *u*, *v*, *w* = velocities; *SST* = sea surface temperature; *CFC* = chlorofluorocarbons; SF_6 = sulfur hexafluoride; *RH* = relative humidity; *LWP* = liquid water path; *PPN* = precipitation; *LWC* = liquid water content; T_{dew} = dewpoint temperature; *SW* = shortwave radiation; *LW* = longwave radiation; *q* = specific humidity. Instruments marked with an asterisk had data broadcast to the Global Telecommunication System, hence were available for operational forecasting.

Simultaneous measurement of the wind speed at 12 different heights is made possible by the use of 12 different range gates for the laser pulse time of flight. From this data a signal processing algorithm computes wind vector components from five consecutive line of sight measurements. The device has an inbuilt motion correction algorithm; however, the raw data was reprocessed after the field campaign using more accurate ship attitude data.

Metek Micro Rain Radar

The Micro Rain Radar (MRR) is a compact FM-CW radar for the measurement of profiles of drop size distributions. Derived from this information are rain rates, liquid water content, and characteristic falling velocity resolved into 30 range gates. This high sensitivity instrument is able to detect very small amounts of precipitation below the threshold of conventional rain gauges. The droplet number concentration in each drop-diameter bin is derived from the backscatter intensity in each corresponding frequency bin. In this procedure the relationship between terminal falling velocity and drop size is used.

Vessel-mounted meteorology

Continuous standard meteorological measurements were captured by two WeatherPack devices. They were sited on the bow mast at 15 m above sea level. New sonic anemometers were fitted before the cruise but failed to work properly. In harbour at the halfway point, one was replaced with a propeller anemometer providing useful measurements. Due to instrument errors gaps also exist in the temperature, pressure and humidity data sets.

CTD rosette and underway continuous measurement

The primary oceanographic measurements were made using the conductivity-temperature-depth (CTD) system deployed form a small Baltic room on the starboard side. From the shelter of this space, CTD operations could be performed during a high sea state and sustained 30-35 knot winds. Water samples were also collected on each cast for chemical analysis using 12 Niskin bottles. When the sea state was too rough to carry out CTD operations, or the ship was short of time to occupy stations, expendable CTD (XCTD) and bathythermograph (XBT) probes were used to measure vertical profiles. In total, 189 CTD stations were occupied, 152 with chemical sampling, and 120 XCTDs and 144XBTs deployed. Continuous conductivity and water temperature measurements were made by the underway CTD system, sampling water through an intake on the bow of the ship at 2.5 m depth. However, this system suffered regular outages due to bubbles forming in the intake.

DH6 Twin Otter research aircraft

British Antarctic Survey's DH6 Twin Otter research aircraft began science operations from 28 February based at Akureyri airport. This versatile aircraft can be flown at low levels (<35 m) to measure surface layer properties, as well as boundary layer cross-sections and vertical profiles via flying in a 'sawtooth' pattern. The aircraft flew a total of 70 science hours, including 505 minutes in the surface layer at around 35 m altitude, of which 435 minutes with during CAO

conditions and 235 minutes were over or near sea ice. Longer missions were allowed by an extended range fuel tank, and its 'short take off and landing' capability made refuelling possible on Greenland at Constable Point. The instrument suite includes temperature and water vapour sensors, and a turbulence probe facilitating turbulent flux measurements via the eddy covariance method. Other notable instruments include upward and downward shortwave and longwave radiation sensors, a downward looking infrared thermometer, a cloud and aerosol spectrometer, a water vapour isotope analyser and video cameras.

Meteorological Buoy

A meteorological buoy was deployed during the first leg of the Alliance cruise. It operated in an open ocean location roughly 200 km away from the MIZ for 78 days in the northwest Iceland Sea (70.649° N, 15.426° W). Measurements of meteorological variables were made hourly, as well as sea surface temperature (SST), ocean currents and wave height, period and direction. Air pressure measurements were found to be erroneous for around half of the period and replaced with mean sea level pressure from ERA5. Likewise, quality control showed that SST measurements were unreliable so were replaced with the shallowest observations from a co-located ocean mooring. At a depth of 8 m these measurements are within the well-mixed ocean surface layer so should compare well, though variability will be reduced (Våge et al., 2018). A short period of air temperature measurements was also removed due to suspected icing, following corroboration with the nearby Jan Mayen meteorological station.

2.1.3 Data processing and quality control

A common problem with making measurements in the harsh conditions of the subpolar seas is the inevitable instrument failure. During the IGP field campaign, the planned high temporal resolution meteorological observations from the WeatherPacks provided far less coverage than intended. However, a continuous data set is vital to investigate ocean-atmosphere interaction and calculate surface turbulent heat fluxes. Problems had been anticipated and prepared for by installing redundancy into the observation system. As a result, the two WeatherPack timeseries from the bow mast (Leg 1: WeatherPack 4, functioning intermittently; Leg 2: WeatherPack 2, near continuous) were supplemented by near-surface temperature humidity and pressure measurements from the Hatpro radiometer on the boat deck, with radiosondes providing an extra reference data set.

Figure 2.4 Photos of observational equipment used during the Iceland-Greenland Seas Project field campaign: a) the WeatherPack meteorological instruments on the bow mast of the *Alliance*; b) a radiosonde launch; c) the RPG Hatpro radiometer; d) a CTD cast being performed; e) the British Antarctic Survey DH6 Twin Otter research aircraft; and f) the Windcube lidar and Micro Rain Radar.

To produce continuous sets of observations these data required synthesising, through a process of quality control and calibration. The procedure followed was to select a 'default' set of observations based on the reliability of the instruments. When this data source becomes unavailable or errant it is replaced by another data source. Though before any variable is replaced a statistical comparison must be carried out in order to remove bias and calibrate the data sets. Important considerations are the instrument position and its immediate environment. Here, details of the data quality control and processing applied are described.

Air temperature

Default observations are from WeatherPack 2 during Leg 2 of the cruise (26 February to 22 March). This instrument is corroborated by radiosonde observations (Figure 2.5). A longer time series covering both legs is available from the Hatpro radiometer surface meteorology sensor, but it suffers from a warm bias due to its position on the deck of the ship. These data sets are compared over a sample period where they overlap, finding a bias of +3.22° C. With a correlation coefficient and slope close to 1, the Hatpro time series are calibrated by subtracting this bias, resulting in good agreement with WeatherPack 2. These time series are spliced together, with a remaining data gap on 10 February filled using observations from WeatherPack 4. However, it is out of syncronisation by several hours, so a small time adjustment is applied. Some infrequent, brief (<3 hours) air temperature measurement gaps remain, so these are infilled with linearly interpolated values to provide a continuous data set.

Air pressure

WeatherPack 4 provided the longest and most reliable air pressure data, checked with independent shipboard observations during the cruise, so is selected as the default time series (13 February to 24 February). By this time WeatherPack 4 had been syncronised with the other instruments. Despite the lower altitude of the Hatpro, comparing its measurements to WeatherPack 4 finds a small bias of –0.67. This is possibly due to the sensor's position near to the air intake for the Hatpro's de-icing blower. As for air temperature, the Hatpro air pressure data was bias corrected and used to infill the time series, and remaining gaps linearly interpolated.

Relative Humidity

Default observations are from WeatherPack 2 during Leg 2 of the cruise (26 February to 22 March). More measurements are available from the Hatpro radiometer, however, feature a non-systematic dry bias. Thus, they are calibrated by assuming a linear relationship, adjusting the Hatpro data using the slope and intercept of the regression analysis. As with the air temperature data, a remaining short gap on 10 February was filled using phase adjusted data from WeatherPack 4 and remaining brief gaps interpolated.

Specific Humidity

To provide a continuous time series, specific humidity has instead been calculated as a function

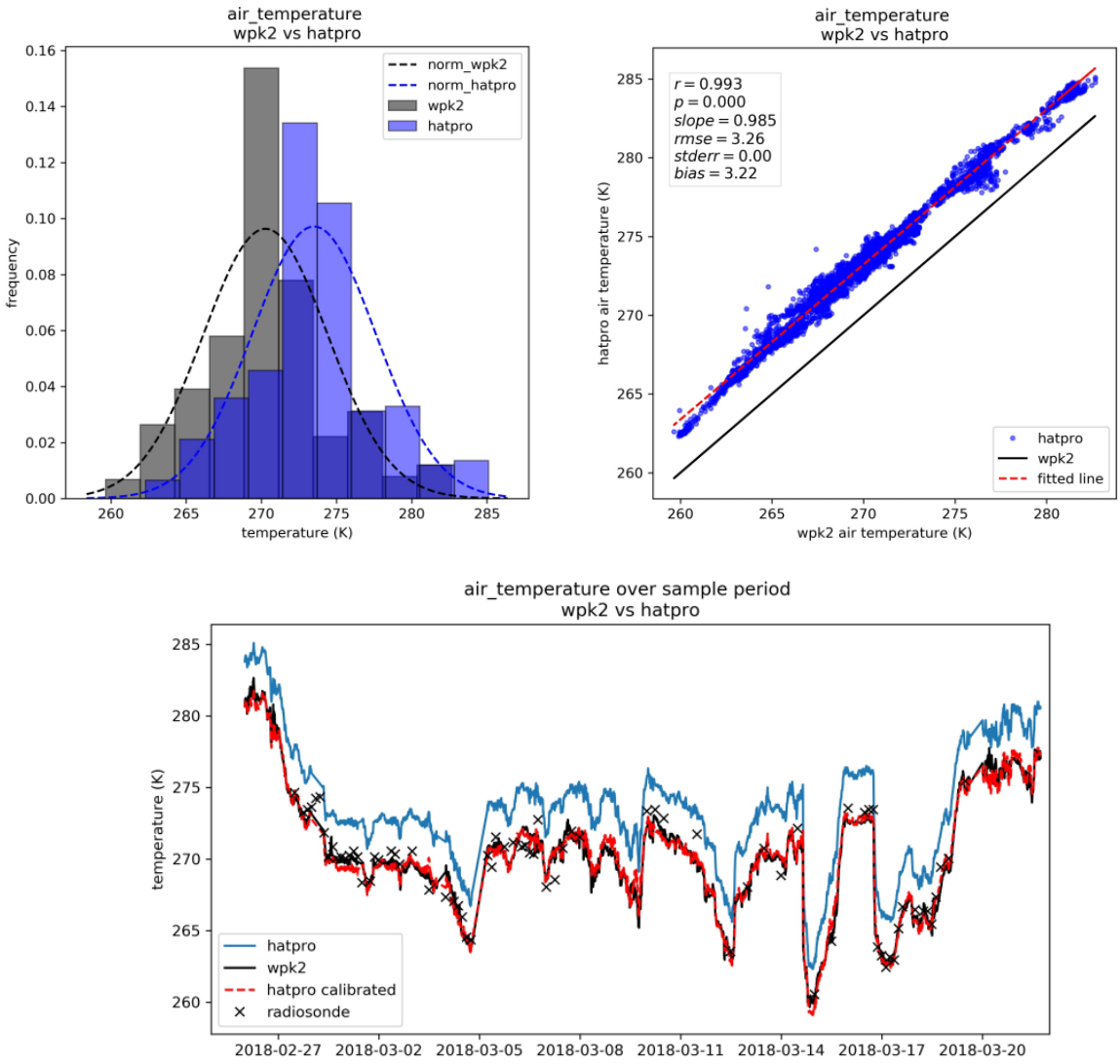

Figure 2.5 a) A histogram displaying the distribution of observations from the instruments WeatherPack 2 (grey) and Hatpro (blue), with bars showing the probability density and dashed lines showing a normal distribution fitted to the datasets. b) A scatterplot displaying a comparison of the two sets of measurements, with the red dash line showing a linear regression fit and key statistics inset. c) Time series for the overlapping period between WeatherPack 2 (black), Hatpro (blue), Hatpro with bias removed (red) and ~30 m radiosonde observations (black crosses).

of the processed relative humidity, air temperature and pressure time series following:

$$q = \frac{w}{1+w} \quad \text{and} \quad w = RH \cdot w_s \,,$$

where w = mixing ratio, RH = relative humidity and w_s = saturation mixing ratio at the given temperature and pressure (Hobbs & Wallace, 1977). During Leg 2, a Picarro water vapour isotope analyser was installed on the boat deck, providing an alternative humidity data set that is in good agreement.

Wind speed and direction

Wind measurements are available from the Windcube lidar (lowest level at 40 m) for most of the campaign, WeatherPak 2 during Leg 2, and the shipboard NMEA system used for navigation (though this is shaded from the wind at certain angles of attack. The Windcube lidar observations have been reprocessed to improve corrections for ship motion at the University of Bergen (Duscha et al., 2022). During the time that Windcube and WeatherPack 2 observations overlap they are generally in very good agreement, however, the WeatherPack also occasionally suffered from wind shading. Further investigation found this shading had occurred during northerly winds while the ship was travelling due south, when the bow mast was lying downwind of the ship's superstructure. As a result, the Windcube lidar data set was selected as the default.

Sea surface temperature

Shipboard underway CTD data were collected for the majority of the research cruise, however with frequent data issues. Throughout the sea surface temperature time series unphysical spikes were removed to reduce error feeding into the bulk aerodynamic flux calculations. The SST fluctuations would be hard to diagnose by themselves, but the conductivity sensor produced even more severe spikes that were easily isolated. This facilitated a programmable method by which periods of unphysical measurements were discarded from the underway CTD data. The remaining data gaps are infilled by CTD cast measurements at 2 m depth and interpolated, when sufficiently high temporal resolution measurements are available.

Surface turbulent heat fluxes and bulk variables

The resultant datasets of standard meteorological variables are used as inputs to the COARE 3.0 algorithm to calculate estimated bulk variables at standard heights (corrected by Monin Obhokov Theory), surface turbulent fluxes and flux coefficients (see Fairall et al., 2003). These processed data offer the best temporal coverage possible, yet gaps remain in the wind and SST sets, leaving gaps in the COARE 3.0 output. Fairall et al. (2003) found that this bulk flux scheme is accurate to with 5% for wind speeds of 0-10 ms^{-1} and 10% for wind speeds of 10-20 ms^{-1}. The resultant dataset, with standardised variables and turbulent heat fluxes, provides a rare and valuable data set for the characterisation of air-sea interaction during the field campaign and for the evaluation of numerical weather prediction products.

Technical summary

The quality controlled, calibrated and synthesised data set was output in NetCDF format, following standardised Climate and Forecast (CF) conventions. Variables are temporally

downsampled to provide 10-minute means to smooth some high frequency instrument noise, while preserving enough detail to analyse small scall meteorological processes. The NetCDF file includes data flags to provide metadata on the source instrument and processing that each processed variable has received at any given point in the time series, and whether the ship was in harbour or on active science duties. The data set has been published online with documentation at www.ceda.ac.uk (see Barrell & Renfrew, 2019), alongside many of the other IGP data sets.

2.2 The Met Office Unified Model

In this thesis we evaluate a range of weather and climate simulations produced using the Met Office Unified Model (MetUM). The MetUM is a seamless numerical weather prediction modelling system which enables the same dynamical core and parameterisation schemes to be applied across a broad range of spatial and temporal scales. The dynamical core is responsible for solving non-hydrostatic deep atmosphere equations using a semi-implicit, semi-Lagrangian approach on a regular longitude-latitude grid. Sub-grid scale processes are represented by parameterisations, such as radiation, surface exchange and boundary layer turbulence (Walters et al., 2017).

For this study MetUM output was accessed from the Met Office managed Archive Storage system (MASS) using MONSooN, a collaborative supercomputing facility offered by the Met Office and Natural Environment Research Council (NERC); and the JASMIN environmental data storage and analysis facility operated by NERC and the Centre for Environmental Data Analysis (CEDA). More detailed description of the model configurations used are provided in the following chapters.

3 Evaluation of predicted surface layer meteorology near the marginal ice zone in the Met Office Global Coupled model (GC2)

3.1 Introduction

Sea ice a dominant constraint for ocean-atmosphere surface fluxes in the polar regions (Bourassa et al., 2013). The marginal ice zone (MIZ) is the band of ocean near the main ice pack that is partially covered in a variety of sea-ice types, ranging in spatial scale from broken floes (around 10 km to 20 m) to brash ice and pancake ice (around 30 cm to 2 m). These are separated by narrow leads and larger spaces of open water. This morphological heterogeneity makes the MIZ dynamic, responding to ocean currents and waves, wind and internal dynamics (Notz, 2012; Renfrew et al., 2019b).

The decline in Arctic sea ice is causing important changes in the position, width and area of the MIZ (Cavalieri & Parkinson, 2012; Kwok, 2018). In satellite records of sea ice concentration over the period 1979-2011, the poleward edge of the Arctic MIZ has retreated poleward into regions where sea ice is increasingly thinner and younger. With the equatorward edge moving comparatively little, summer MIZ width has been found to have increased by 13 km decade^{-1}, representing a 39% widening (Strong & Rigor, 2013). Climate models project this trend to continue, with summer sea ice conditions in the 'new Arctic' becoming analogous to the MIZ (Sigmond et al., 2018).

When a cold-air outbreak (CAO) flows over the MIZ, strong air-sea exchange drives rapid changes in the atmospheric boundary layer (ABL). Fluxes of heat and moisture from the ocean to the ABL peak immediately downwind of the MIZ, with sharp increases in ABL temperature and humidity (Renfrew & Moore, 1999; Liu et al., 2006; Spensberger & Spengler, 2021). This ABL development has been shown to be very sensitive to sea ice distribution using numerical simulations, with significant differences in temperature, humidity, wind, cloud and surface fluxes over the MIZ and downstream depending on sea ice fraction and distribution. For example, the development of roll clouds has been shown to be dependent on the existence and structure of the MIZ (Liu et al., 2006; Gryschka et al., 2008).

Accurate simulation of CAOs and their interaction with the MIZ in numerical weather prediction (NWP) models is important for weather forecasting near the MIZ and downwind. However, there

is a paucity of observations in the high latitudes that results in substantial uncertainty in forecasts, particularly where air-sea interaction is concerned. Here, this problem is tackled by employing a novel set of observations made as part of the Iceland Greenland Seas Project (IGP; Renfrew et al., 2019a). NWP models often crudely represent air-sea-ice interactions over the MIZ leading to significant biases in surface fluxes and surface layer meteorological variables that can extend for hundreds of kilometres downstream (Bourassa et al., 2013). These biases are often caused by poor representation of surface exchange, such as unrepresentative drag coefficients (Elvidge et al., 2016; Renfrew et al., 2019b). Furthermore, this problem has generally been compounded by the common assumption of persistent sea ice and sea surface temperature (SST) fields in NWP to enable computationally less expensive atmosphere-only models.

Aiming to improve short- to medium-range forecasting, a new generation of coupled models for high resolution operational forecasting has been developed in recent years, taking lessons from lower resolution long-range climate models. A leading example is the European Centre for Medium Range Weather Forecasts' (ECMWF) Integrated Forecast System (IFS) high resolution global forecasts (HRES), which since June 2018 (IFS Cycle 45r1) have benefited from dynamic and thermodynamic coupling between sea ice, ocean and atmosphere. Evaluation of this model demonstrated that the assumption of persistent sea ice is detrimental to medium-range predictions of sea ice and local 2 m air temperature (Keeley & Mogensen, 2018). Despite this study's overall finding, wintertime bias in the coupled model was comparable to the uncoupled version and a more detailed analysis is required to establish where the benefits are most prominent, and the sources of error.

At the time of writing, the Met Office's global operational forecast system remains atmosphere only, with work ongoing to transition to a coupled model configuration. Here we evaluate psuedo-operational forecasts from a version of the Met Office's coupled model in development through comparison with the operational uncoupled model using in-situ surface layer meteorological measurements made during the Iceland-Greenland Seas Project (IGP). This novel data set is exceptional in its diversity of measurements during the winter, where observations are sparse. Hence, this chapter aims to use these rare in-situ observations to establish the value of the coupled model and provide valuable feedback to the Met Office, helping to inform future development of coupled model configurations.

In Section 3.2 the IGP observations and model versions evaluated are described. In Section 3.3 the sea ice and sea surface temperature fields are evaluated, and the impacts on surface layer

atmospheric variables discussed, with further discussion in Section 3.4 and conclusions in Section 3.5.

3.2 Data and methods

3.2.1 In-situ observations

The IGP field campaign that took place in February and March 2018 provides atmospheric and oceanic observational data sets from a range of instrument platforms that are described in Chapter 2 and Renfrew et al. (2019a). Here we make use of the synthesised surface layer meteorology from the *Alliance* research vessel (Barrell & Renfrew, 2019), the meteorological buoy in the northwest Iceland Sea (Reuder et al., 2020) and two flights (293 and 294) performed by the research aircraft (Renfrew et al., 2021) in the vicinity of the ship to corroborate measurements. The buoy's air pressure sensor failed soon after deployment, so values are infilled from ERA5 to permit processing using the COARE3.0 algorithm as done for the shipboard data (Fairall et al., 2003). Another short period of data was removed due to suspected icing on the temperature sensor, corroborated with temperature readings from Jan Mayen meteorological station (see Renfrew et al., 2020).

3.2.2 Met Office model configurations

Global operational forecast (uncoupled)

The MetUM atmosphere only global configuration (10 km grid, 70 vertical levels) provides short to medium range weather forecasts. The forecasts used in this study were operational at the time, produced using the Global Atmosphere 6.1 (GA6.1) and Global Land 6.1 (GL6.1) configurations (both described by Walters et al., 2016). We refer to the uncoupled model as the UCM.

Sea surface temperature and sea ice concentration for model initialisation are taken from the Met Office's daily Operational Sea-surface Temperature and sea Ice Analysis (OSTIA), provided at a horizontal resolution of ~6 km. OSTIA's daily SST and SIC are sourced from satellite observations from the EUMETSAT Ocean and Sea Ice Satellite Applications Facility (OSI-SAF).

GL6.1 specifies the model's handling of exchange between the land, ocean or ice surface and the atmosphere above. In this configuration, roughness length (z_0) is a key parameter for calculation of surface exchange (Renfrew et al., 2019b). Over sea ice and the MIZ roughness length for momentum flux is prescribed by a single value: $z_{0\_ice} = 3 \times 10^{-3}$ m, $z_{0\_MIZ} = 100 \times 10^{-3}$ m. Similarly, the scalar roughness lengths for heat and moisture exchange are prescribed over sea

ice, with $z_{0T} = z_{0q} = 0.6 \times 10^{-3}$ m. Over the MIZ, these scalar values are set by a basic assumption, where $z_{0T\_MIZ} = z_{0q\_MIZ} = 0.2 \times z_{0\_MIZ}$.

Global coupled model version 2 (GC2)

The experimental Global Coupled Model 2.0 (GC2; herein referred to as the coupled model or CM) is based on the global operational forecast model with the same 10 km horizontal grid length and an increased 85 vertical levels (Williams et al., 2015). Employing the MetUM's seamless approach, the CM largely features the same atmospheric dynamics and parameterisations as the UCM. Its configuration includes GA6.1 and GL6.1 meaning roughness lengths over pack ice and the MIZ are prescribed the same as described above for the UCM allowing direct comparison.

Ocean-ice-atmosphere interaction is enabled by Global Ocean 5.0 (GO5.0; Megann et al., 2014) and Global Sea Ice 6.0 (GSI6.0; Rae et al., 2015) components. Coupling is achieved using the Met Office's Forecast Ocean Assimilation Model (FOAM; Blockley et al., 2014) with interactive ocean from the Nucleus for European Modelling of the Ocean (NEMO; Madec, 2008) community model and the Los Alamos CICE sea ice model version 4.1 (incorporated in GSI6.0; Hunke and Lipscomb, 2010) that is integrated with the atmosphere model using the OASIS coupler. This is also initialised using SST and SIC data from OSTIA. The CM version tested here uses an ocean model with 1/4° resolution.

GSI6.0 uses the 'zero-layer' thermodynamic model of Semtner (1976) to calculate the growth and melt of sea ice. Despite a multi-layer ice model being available in CICE version 4.1, it was not implemented in GC2 because the sea ice surface temperature and conductive heat flux into the ice are calculated by the atmospheric component of the model (GA6.1); this is not consistent with the CICE multi-layer scheme, which calculates these quantities itself (Rae et al., 2015). Note, in Chapter 4 the Global Coupled Model 3.1 (GC3.1) is investigated, where the use of a multi-layer sea ice scheme is a key development. In GSI6.0 a constant value for the freezing point of sea water is used T_f = -1.8 °C. The model calculates surface temperature, T_s, considering the heat fluxes to the surface, and accounting for the energy used to melt the sea ice, until $T_s - T_f = 0$ or the sea ice fraction is reduced to 0. Thus, if sea ice exists in a grid cell after this calculation, but is less than 100% concentration, grid cell T_s = -1.8 °C.

3.2.3 Case Study selection

As a means for evaluating the coupled and uncoupled models three case studies have been investigated. For each case study the forecasts (initialised at 00 UTC at the start of each case

period) are evaluated using observations made aboard the *Alliance*. The objective of this approach is to isolate two periods during CAOs, with a third comparative case featuring what may be considered as opposing conditions with advection of relatively warm and moist southerly air over the region, known as a warm-air intrusion (WAI).

The cold-air outbreak cases make use of opportunistic measurements and are not measured in the same locations, during the first the research vessel was in the Iceland Sea, the second in the Greenland Sea. The WAI period was selected to be around the geographical region of the first CAO case over the Iceland Sea. Synoptic charts for each case are provided in Figure 3.1 and an overview of the observations used in Figure 3.2 and. A brief description of the synoptic situation for each case study is provided:

- *WAI1 (15-02-2018 to 20-02-2018)*

  This period was dominated by an anomalously warm air mass advected from the south (Figure 3.1a), associated with a positive phase of the North Atlantic Oscillation (NAO; Renfrew et al., 2019a). Air temperatures were typically above 0 °C and relative humidity above 90%, while wind speeds were moderate between 5 and 15 ms^{-1}. Measurements were made in the Iceland Sea in similar area to CAO1 enabling a direct comparison.

- *CAO1 (27-02-2018 to 04-03-2018)*

  A transition to NAO negative conditions occurred on 26 February 2018 as part of a typical delayed response to a sudden stratospheric warming (SSW; Kolstad et al., 2010) that had occurred on 8 February 2018, which was also responsible for the 'Beast from the East' over the UK. In the morning of 28 February 2018, a southward advancing cold front passed the *Alliance*, associated with a small baroclinic mesoscale cyclone that enhanced wind speeds (Figure 3.1b; Figure 1.4), resulted in a sudden change in conditions observed at the ship. Air temperature dropped from 2 °C to –3 °C and wind speed increased from 2 ms^{-1} to 16 ms^{-1} in less than 12 hours. This started a prolonged period of weak to moderate CAO conditions over the Iceland and Greenland Seas.

- *CAO2 (15-03-2018 to 19-02-2018)*

  A shorter but stronger CAO was observed over the Greenland Sea and was also associated with a mesoscale cyclone (Figure 3.1c). On the afternoon of 16 February 2018, the CAO onset seen at the ship was more extreme than CAO1 as air temperature fell from around 0 °C to –9 °C and wind speed increased from 8 to 21 ms^{-1} in 6 hours. This event was mostly restricted to the Greenland Sea and only measured for several

days due to the NRV Alliance needing to travel south to meet its scheduled return to port at the end of the campaign.

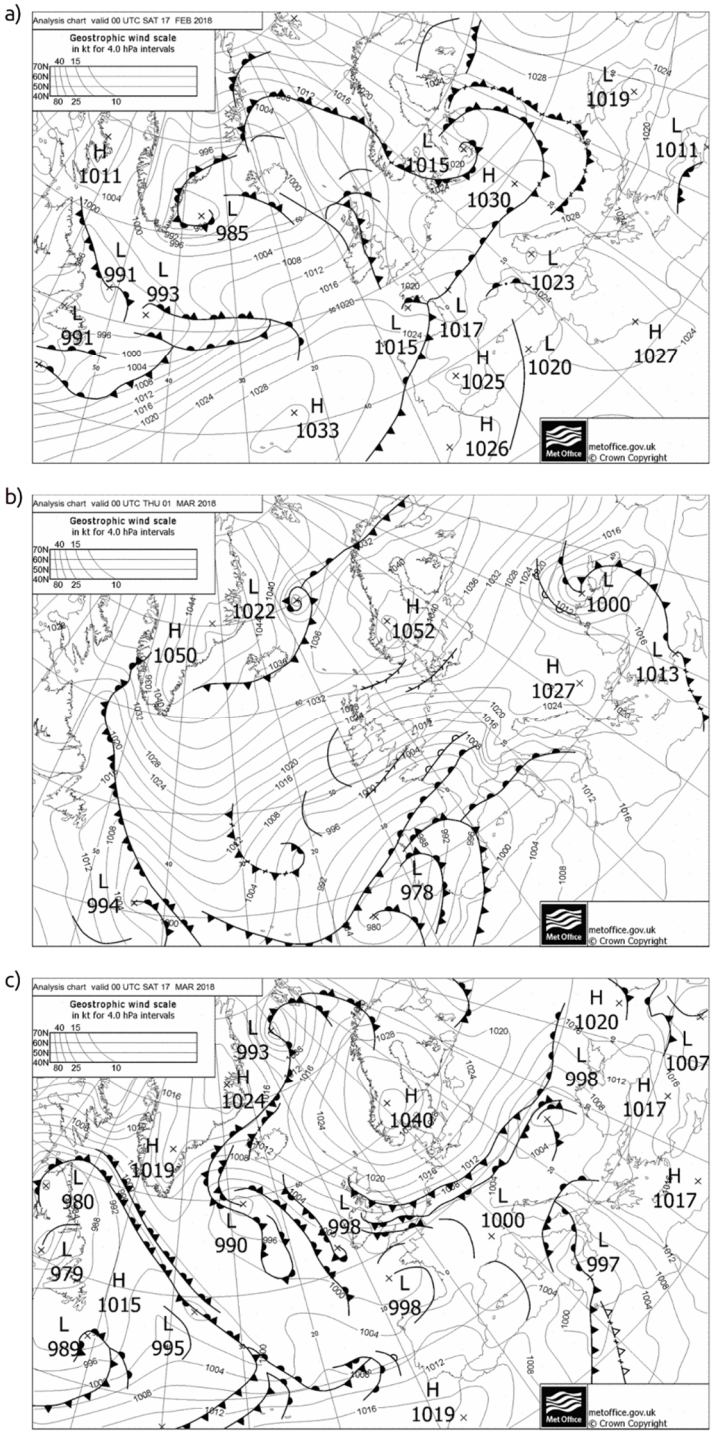

Figure 3.1 Met Office mean surface level pressure analysis charts for the North Atlantic region: a) 00 UTC 19-02-2018, T+48 hours in case study WAI1; b) 00 UTC 01-03-2018, T+48 hours in CAO1; and c) 00 UTC 17-03-2018, T+48 hours in CAO2.

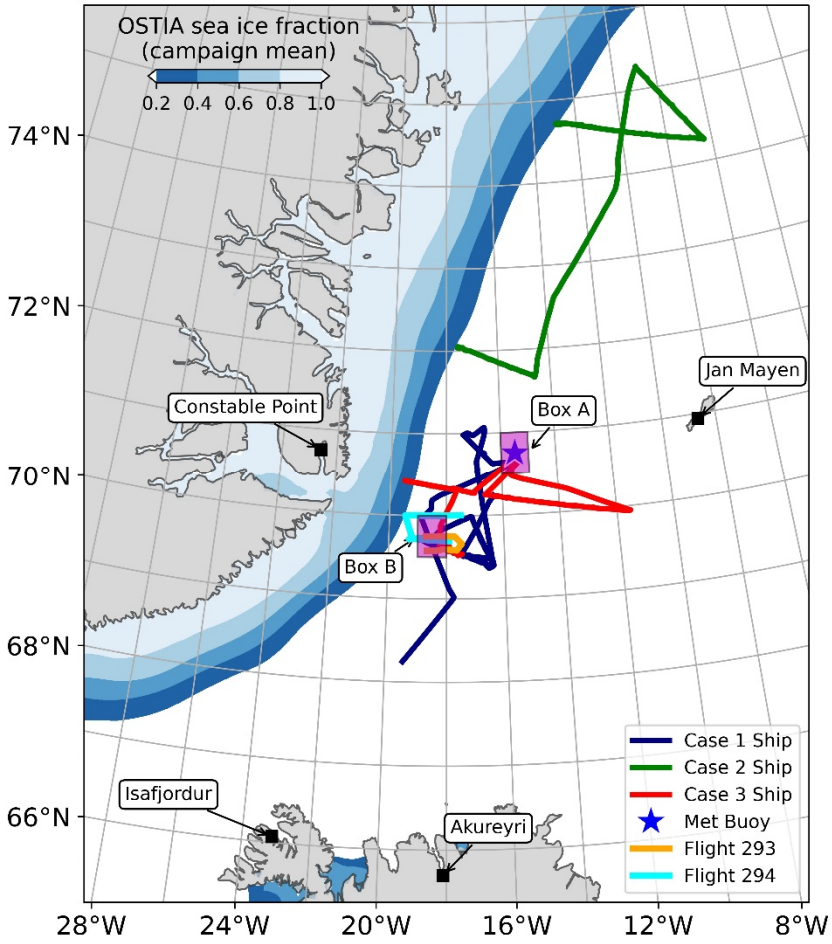

Figure 3.2 Overview of the track of the Research Vessel Alliance during Cases 1, 2 and 3 (dark blue, green and red lines respectively), science legs of Flights 293 and 294 (orange and cyan respectively), location of the meteorological buoy (blue star) and Boxes A and B (labelled) used for analysis in Section 3.4.

3.3 Results

To gain an understanding of the spatial patterns in the models, surface fields are shown for a region encompassing the Iceland Sea and the Greenland Sea, with shipboard observations also shown using the same colour scale. The maps depict the nearest daily (1200 UTC) OSTIA sea ice analysis with magenta contours for 20% and 80% SIC. These allow an assessment of the modelled sea ice field against real world sea ice evolution. To evaluate model predictions, values were extracted at nearest-neighbour grid cells to the location of the ship at model time steps. This enables a comparison of predictions against observations made on a moving platform, time series analysis and the derivation of scatter plots and statistics to assess model skill. First the modelled sea ice fields are evaluated, then the implications for surface temperature and near-surface meteorology are discussed.

3.3.1 Dynamic versus persistent sea ice

First, we compare dynamic sea ice in the CM with the persistent field in the UCM then discuss the implications for surface meteorology in the following sections. Figures 3.3, 3.4 and 3.5 display the surface temperature and sea ice concentration in the uncoupled and coupled models, and the difference between them, at T+36 hours in each forecast period. A key difference between the models is that the UCM removes any sea ice with concentration <15% on initialisation. This has the effect of creating a more abrupt ice edge than the original OSTIA sea ice product. In comparison, the CM features a wider MIZ extended by a wide band of low concentration sea ice in the outer MIZ.

At a forecast lead time of T+36 hours it is already apparent that the UCM persistent sea ice field does not accurately match the updated OSTIA sea ice analysis in CAO1 (Figure 3.4), in which the MIZ has expanded towards the east and south. The sea ice edge lies approximately 100 km further to the east in the CM. However, when looking at the difference between the model sea ice fields, this increase in sea ice is not visible on the colour scale as it is <10%. What this difference plot does highlight though is that the MIZ is significantly wider in the CM, making more accurate than that in the UCM.

Another difference between the models is noticeable in the distribution of the sea ice. The CM shows some local regions of higher and lower concentration sea ice along the MIZ more similar to those that occur in real world conditions due to currents and wind forcing, unlike the homogeneous UCM sea ice field. However, at this grid scale these features lack the observed sharp gradients in sea ice concentration.

In CAO2 the same band of sea ice appears in the CM even more clearly defined than in CAO1 (Figure 3.5). At first glance the UCM appears similar to the CM and matches the updated OSTIA analysis better than in CAO1, however, the difference plot shows that in fact there has been significant ice growth in almost all of the CM ice field. A notable exception is a patch of reduced ice concentration near the Denmark Strait in the CM, which corresponds with a local wind jet associated with an orographic barrier flow flowing north to south along the East Greenland coast. This demonstrates that the CM is somewhat realistically simulating wind forced sea ice divergence.

Despite WAI1 being of figuratively opposite synoptic conditions, with opposing wind flow advecting relatively warm and moist air into the region, the same band of low concentration sea ice exists in the CM (Figure 3.3). This evidences that this band is caused by the inclusion of sea ice with concentration <15% in GSI6.0, not due to freezing under CAO conditions. Yet in this

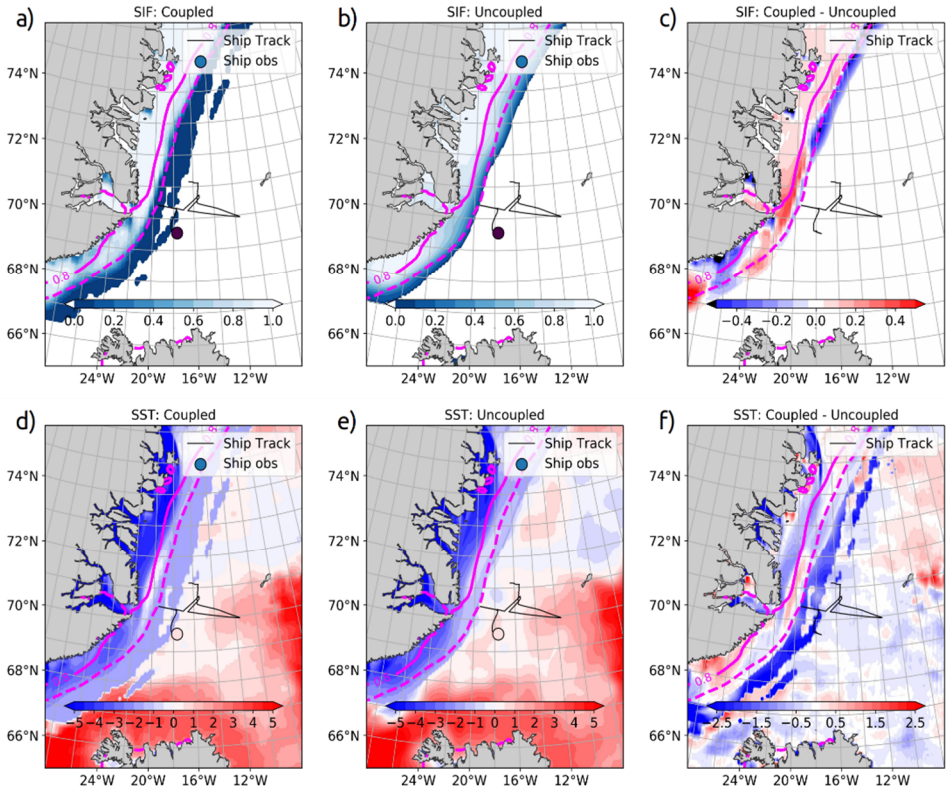

Figure 3.3 Comparison of coupled and uncoupled forecasts for WAI1 at 12 UTC 16/02/2018 (T+36 hours) for sea ice fraction (top row) and sea surface temperature (bottom row). Panels a) and d) show the coupled model, b) and e) the uncoupled model, and c) and f) the coupled model minus the uncoupled model. The magenta dashed and solid lines show the 20% and 80% sea ice concentration contours from the nearest daily OSTIA analysis.

case, in the northern part of the CM domain, the MIZ loses a significant amount of ice in line with the warmer conditions. Again, this demonstrates that the live sea ice in the CM is a more accurate simulation as it matches the OSTIA contours more successfully than narrower MIZ in the UCM. By T+84 hours into the CAO1 forecasts the persistent sea ice field in the UCM poorly matches the OSTIA analysis (Figure 3.7). In contrast, the CM is closer to OSTIA, with ice growth mirroring the observed eastwards propagation of the ice edge. However, it cannot be said that the CM sea ice field is accurate; above 72° N the 20% sea ice contour does not advance eastwards enough, either underestimating thermodynamically driven freezing of surface waters during the CAO or dynamic ice transport.

Conversely, in CAO2 the CM sea ice is reasonably accurate on the fourth day of the forecast. Though, this is mainly due to the more constant sea ice field, illustrated by comparing the persistent UCM sea ice with the OSTIA analysis (Figure 3.8). Nonetheless, the outer MIZ remains far extended eastwards in the CM.

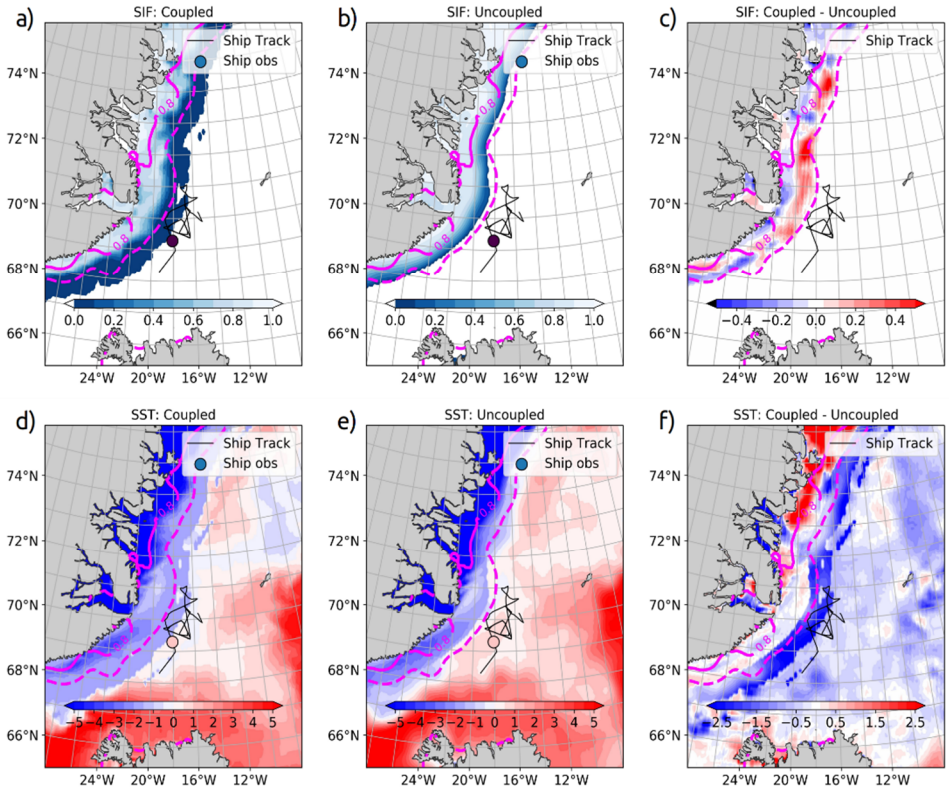

Figure 3.4 As Figure 3.3 for CAO1 at 12 UTC 28/02/2018 (T+36 hours).

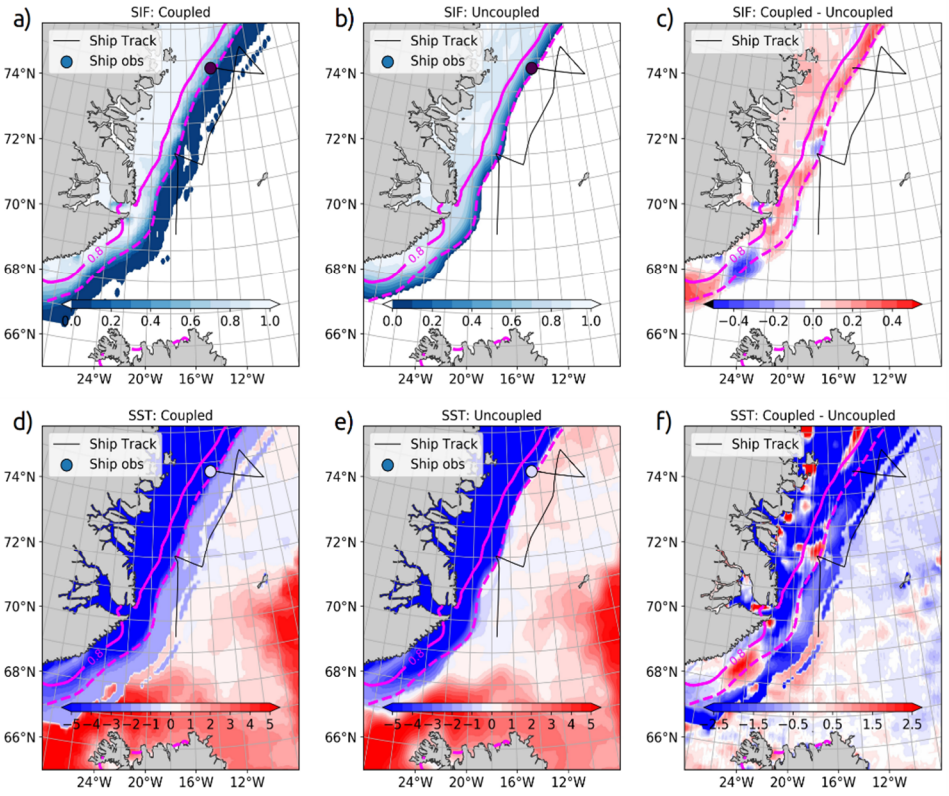

Figure 3.5 As Figure 3.3 for CAO2 at 12 UTC 16/03/2018 (T+36 hours).

As seen in the earlier forecast time step discussed, WAI1 is marked by MIZ retreat in the northern part of the domain (Figure 3.6). By T+84 hours into the forecast, the CM has lost a significant amount of ice in this region that appears to match the observed pattern accurately.

The ubiquitous extended band of low concentration sea ice seen in these cases in the CM denotes a region where a very small amount of sea ice exists. However, in truth the sea ice in this region consists of the odd small ice flow and tiny melting fragments that are widely dispersed. This extremely sparse sea ice has little impact on ocean wave dynamics or surface roughness. As such, the prescribed model surface roughness value should arguably be very similar – if not the same – as that of the ice-free ocean, yet this is not the case. Depending on wind speed, the surface roughness of the ocean (z_{0_ocean}) is in the range of 1×10^{-2} to 1×10^{-5} m (Donelan et al., 1993). But over the MIZ, the model surface roughness (z_{0_MIZ}) is set to a blanket value of 0.1 m. The result of this is that crossing the boundary from 0 to 1% sea ice concentration represents a sudden large stepwise increase in model surface roughness, while in reality the surface is virtually unchanged.

This problem explains the decision to remove any sea ice below 15% concentration in the UCM, as a crude method for tuning the model while minimising computational cost of the surface exchange parameterisation scheme. As the CM does not employ such a tactic, the resulting outer MIZ is a key difference between the models, which has an impact on ocean-ice-atmosphere momentum, heat and moisture fluxes.

3.3.2 Effects on surface temperature

Despite the outer MIZ that consistently exists in the CM forecasts being of low concentration, it has a commanding influence on the surface temperature (T_s) field. Where grid cells contain marginal sea ice the model sea water temperature is around freezing point (–1.8 °C). This temperature can be incorrect around the low concentration outer MIZ region, illustrated by the unphysical T_s gradients in the CM in Figure 3.5. In each of the three case studies a clear band of cooler T_s exists in the CM that corresponds with the low concentration sea ice. Particularly in the CAO2 and WAI1 cases, where the prominence of this cold T_s band is highlighted by its juxtaposition next to areas of warmer T_s in the CM in parts of the domain. However, it should be remembered that the representation of surface temperature is limited by the model resolution, which is unable to resolve small scale eddies and filaments.

Shipboard *SST* measurements by the *Alliance* (shown by the shaded dots in panels d) and e) of Figures 3.3, 3.4 and 3.5) provide an approximate method to evaluate modelled T_s against in-situ observations. Note, the underway *SST* measurements are made by a water inlet at 2.5 m depth

on the bow of the ship, hence observing the top layer of the ocean. Although the sensor is close to the sea water intake to minimise effects from the ship, this measurement is different to the temperature at the ocean-atmosphere boundary, T_s. Nonetheless, the *Alliance SST* data provides a close approximation of T_s for the purpose of this analysis. At T+36 hours in WAI1 and CAO1 (Figures 3.3 and 3.4) the UCM appears to match the observations more closely than the CM. In CAO2 (Figure 3.5) the measured *SST* is warmer than both models at the ship's position, however this could be due to the ship being further in the modelled MIZ. The cause of this is likely due to be one or both of two factors: first, as previously mentioned, the model sea ice field and its OSTIA basis being overly smoothed and not representative of true sea ice distribution; and second, an observational bias that occurs due to the ship intentionally navigating to avoid sea ice. Nonetheless, this does evidence that further into the MIZ, *SST* is typically around freezing point.

Considering the models' T_s across the whole domain, the CM is typically significantly cooler than the UCM. It could be that this is partly the result of cooling by the overlying cold airmass in the CAO cases, but it is also the case for most of the domain in WAI1 when the overlying air was warmer than the ocean. In WAI1, the excepting region of warmer T_s in the northern part of the domain corresponds with a region of surface water that was below 0 °C, where the air-sea temperature gradient was greatest, hence warming would be expected in a responsive ocean model. Comparatively, in the southern part of the domain, where *SST* is of similar temperature with the overlying airmass and a more equilibrium state would be assumed, the CM *SST* remains cooler than the T_s analysis in the UCM. Indeed, this region of T_s warming in the CM correlates with increased downward sensible heat fluxes (not shown), though it should be noted that modelled turbulent heat fluxes during WAI1 are positive downward over much of the domain, including where *SST* is cooler in the CM.

At T+84 hours the open ocean CM T_s is very similar to the earlier time step in all three cases (Figures 3.6, 3.7 and 3.8), albeit with some detectable cooling during the CAO cases. Yet a notable difference at the later time step is some erosion of the outer MIZ in all cases. This suggests that this band of sea ice was misplaced with the ocean model working to correct the initialisation problem. Over sea ice and the MIZ, warmer patches in the T_s difference plots typically correspond to where SIC is reduced, exposing the warmer underlying ocean.

An evaluation of the accuracy of the model T_s fields is enabled by comparison with the measured SST time series from the *Alliance*. Figure 3.9 compares six-hourly observations and each model's prediction for the ship's position, with one-hourly observations added for insight. In all cases

there are points where the ship has entered the fringe of the MIZ, effectively shown by the points where the measured SST drops significantly below 0 °C. However, the CM predicts more of these events than observed, particularly in CAO2 and WAI1, suggesting that its MIZ and associated freezing point T_s are incorrectly simulated. Furthermore, at moments where the ship has encountered some marginal sea ice, the CM T_s of –1.8 °C is too extreme, with observations closer to 0 °C.

The time series for each case shows that the CM T_s is cold biased. This is confirmed by the scatter plots in Figure 3.9, which demonstrate that the cold bias exists for almost all data points across the three case studies, typically by –0.5 to –1.0 °C. This is influenced by the numerous points where the CM incorrectly predicts T_s to be at –1.8 °C. These occur when the ship lies within the CM outer MIZ described in Section 3.3.1, evidencing that this extended MIZ is poorly simulated. Verification of the model MIZ extent using available satellite products is an important next step and will be carried out in Chapter 4.

3.3.3 Effects on surface layer meteorology

Air Temperature

Over the open ocean during the CAO cases, near-surface air temperature (T_{2m}) is almost universally cooler by up to –1 °C in the CM at T+84 hours into the forecasts (Figures 3.7 and 3.8). In both cases this is generally the result of the CAO airmass having passed over more extensive, more concentrated and lower temperature MIZ leading to cooler surface layer air. This is illustrated by the difference between the models being greatest just off the ice edge and decreasing with distance downstream; the surface layer air is increasingly mixed with air from higher within the ABL that has more similar properties in the two models. In WAI1, with warmer air advected into the region from the south, T_{2m} is comparatively warmer in the northern half of the CM domain and cooler in the south (Figure 3.5). Comparing the models' temperature and mean sea level pressure fields (not shown) reveals that this difference is due to a difference in timing of the passage of a band of warmer air associated with a small mesoscale cyclone to the east, which in the UCM had moved further northwards and out of the domain at this time step. Over sea ice and the majority of the MIZ, model differences in T_{2m} correspond with the differences in the T_s field, hence, largely result from the evolving sea ice in the CM. During the two CAOs, patches of warmer T_s and T_{2m} are due to reductions in sea ice concentration and gaps opening at the coast due to wind stress. In WAI1 a similar relationship between T_s and T_{2m} exist, which is particularly clear near Scoresby Sund and along the Greenland coast to the south where the CM is significantly warmer in both fields (Figure 3.6).

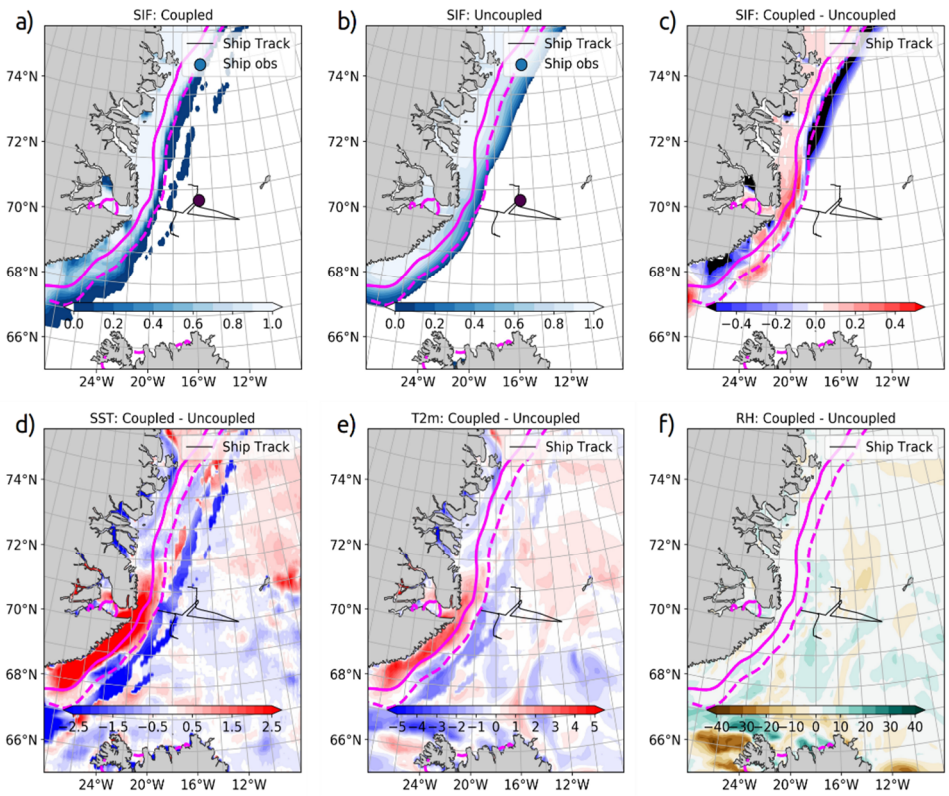

Figure 3.6 Comparison of uncoupled and coupled forecasts for WAI1 at 12 UTC 18/02/2018 (T+84 hours). Panels a), b) and c) show sea ice fraction for the coupled model, uncoupled model and the difference (coupled minus uncoupled) respectively; d) sea surface temperature difference, e) 2 m air temperature difference, and f) relative humidity difference. The magenta dashed and solid lines show the 20% and 80% sea ice concentration contours from the nearest daily OSTIA analysis.

A key difference between the models T_s caused by the outer reaches of the MIZ that exists in the CM were discussed in Sections 3.3.1 and 3.3.2. Due to grid cells being considered part of the MIZ, the increased model z_{0T_MIZ} enhances heat exchange between the surface and the atmosphere. The effects of this can be seen in all three cases. In the two CAO cases, where there has been substantial growth of sea ice the result is lower T_{2m} in the CM. However, over the low concentration outer MIZ there is a detectable band of warming T_{2m} in the CM, despite being co-located with cooler T_s. Comparatively, in WAI1 the outer MIZ in the CM translates to lower T_s and associated T_{2m} as would be expected. To reiterate, during the CAOs in the CM there is a band of enhanced upward heat flux into the atmosphere over the outer MIZ, despite model T_s being at freezing point due to the existence of sea ice and colder than in the UCM. Hence, we attribute this enhanced heat flux to the parameterisation scheme and its high z_{0T_MIZ} value, even where sea ice concentration is nearing 0%. The significant differences in air temperature that result from the representation of sea ice illustrate the importance of accurate sea ice simulation for the CM to prove beneficial.

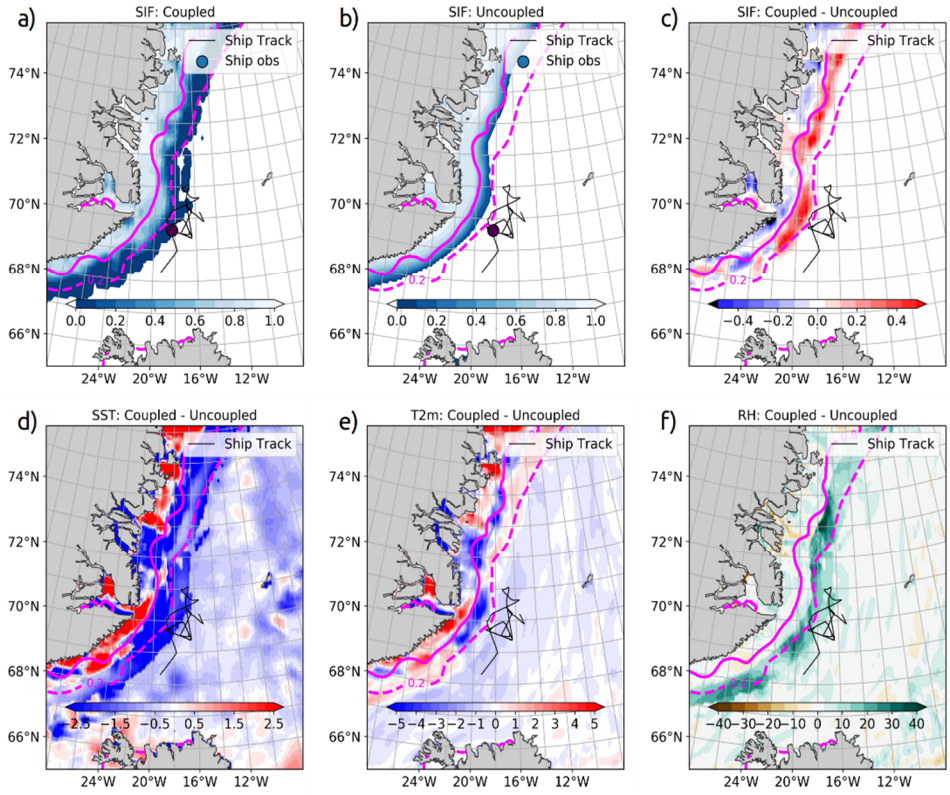

Figure 3.7 As Figure 3.5 for CAO1 at 12 UTC 02/03/2018 (T+84 hours).

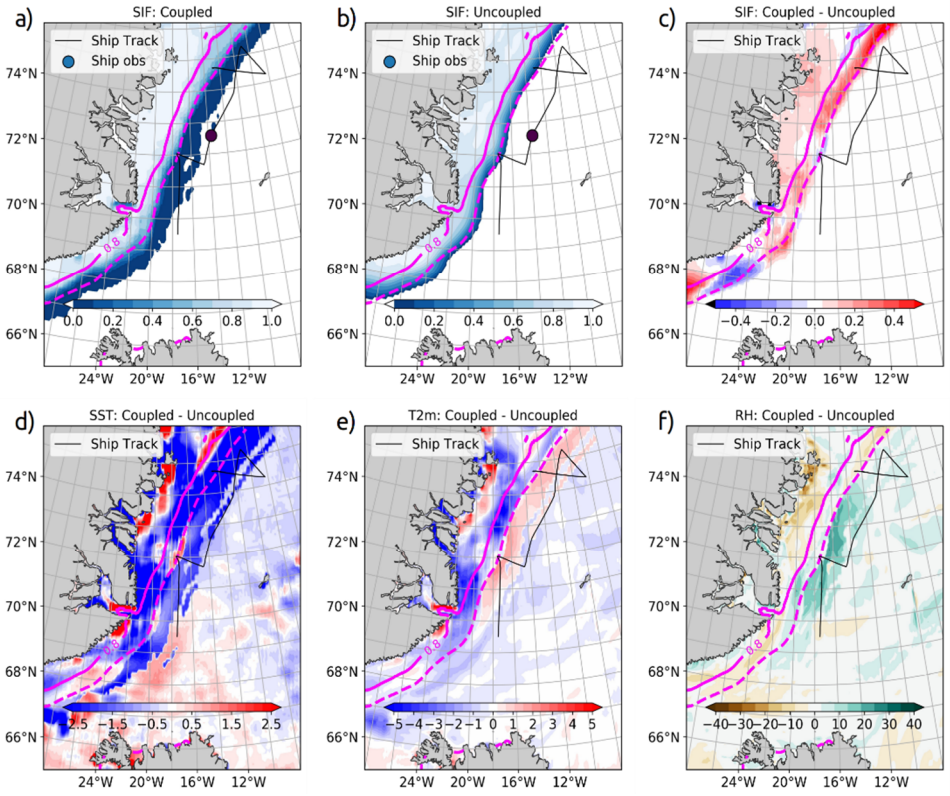

Figure 3.8 As Figure 3.5 for CAO2 at 12 UTC 18/03/2018 (T+84 hours).

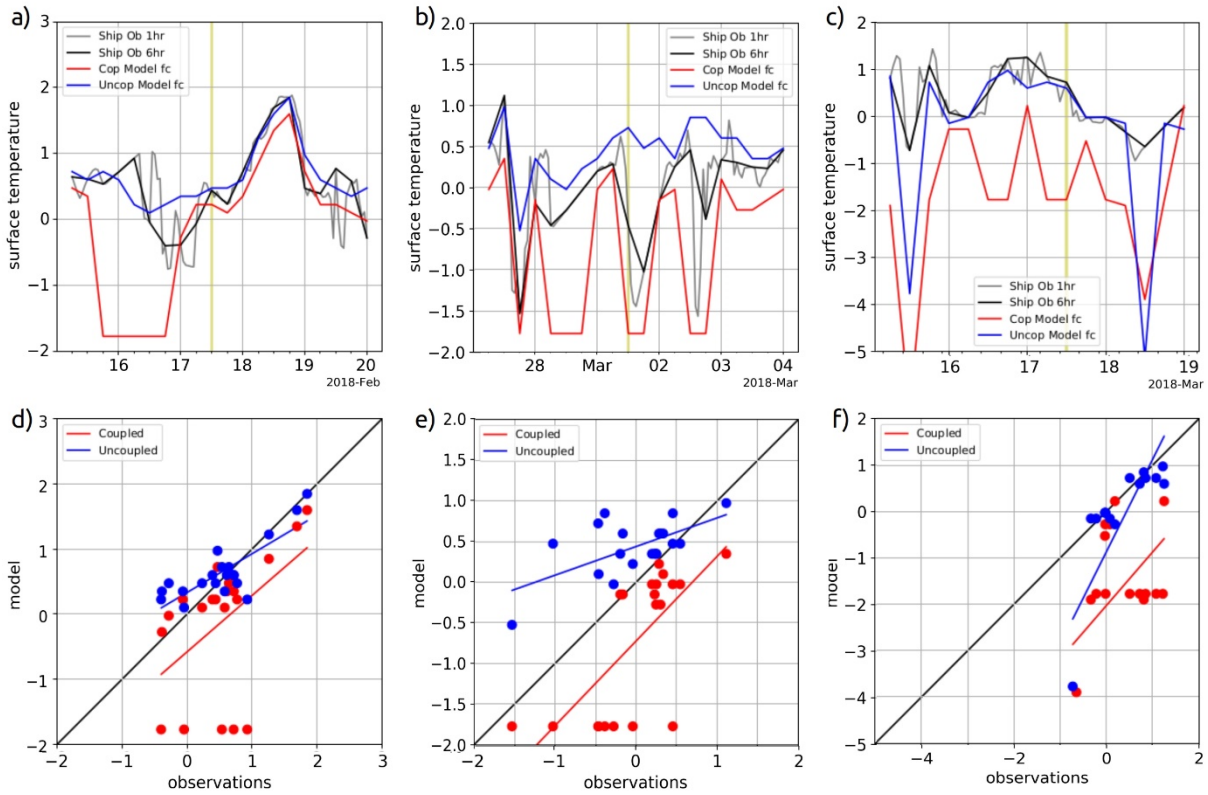

Figure 3.9 Comparison of time series of sea surface temperature observations from the *Alliance* (1-hourly in grey; 6-hourly in black) against model predictions extracted along the ship track from the coupled model (red) and the uncoupled model (blue); and scatterplots comparing 6-hourly model predictions against observations for each forecast period for a) and d) WAI1; b) and e) CAO1; and c) and f) CAO2.

Comparing time series of observations and model predictions at the location of the ship provide a means for evaluating whether the dynamic sea ice in the CM has a positive effect on near-surface forecasting. During each case study, the ship spent a good deal of time near the MIZ and periodically entered its fringes, often in the region where the CM assumes the outer MIZ exists but not in the UCM.

In CAO1 the CM T_{2m} time series shows better agreement with observations than the UCM, with the scatterplot below confirming the CM's good performance (Figure 3.9). During the CAO conditions, the CM is consistently cooler, which is partly attributed to the CM atmosphere's interaction with lower surface temperatures due to the MIZ extending eastwards and growing in concentration. In CAO2, however, the time series are more similar between the models. Interestingly, both predict the arrival of the CAO cold front at the position of the ship around 12 hours earlier than observed. The standout division between the models occurs when ship enters the outer MIZ in the CM, where, as mentioned above, the significantly higher z_{0T_MIZ} value results in greater transfer of heat into the atmospheric surface layer.

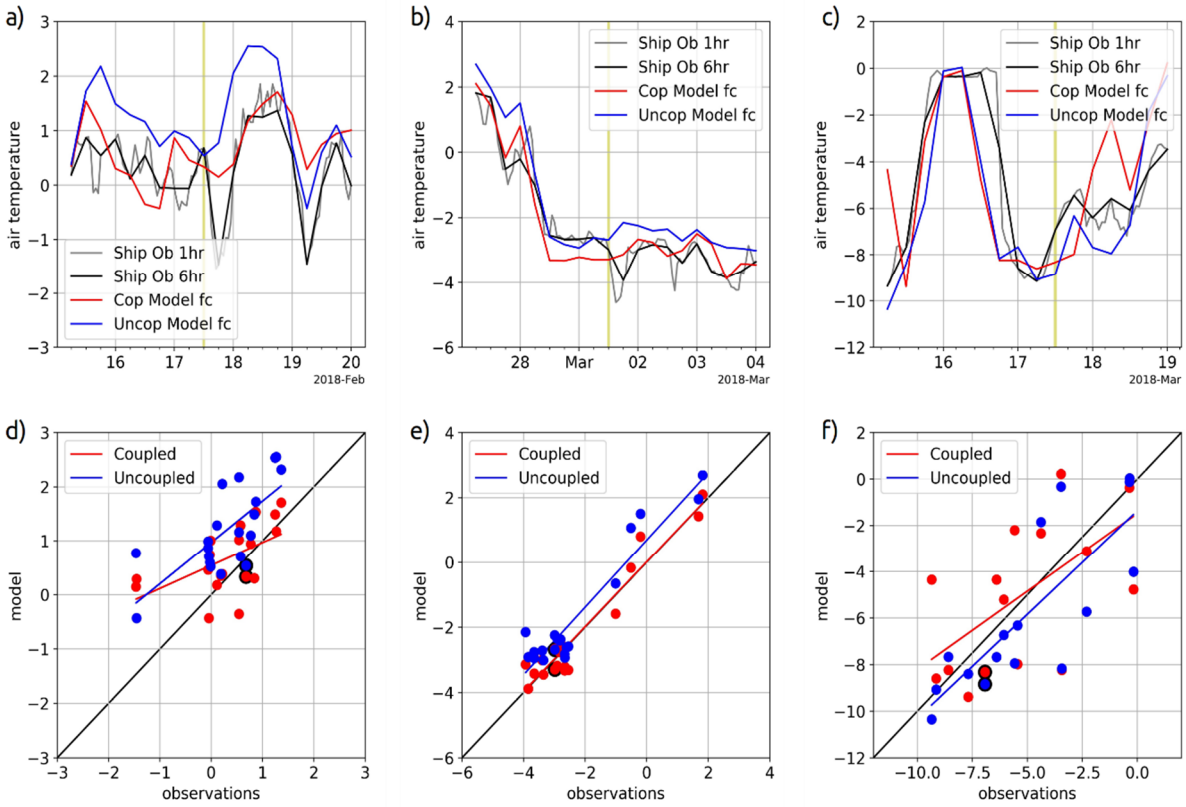

Figure 3.10 As Figure 3.8 for 2 m air temperature.

The WAI1 scatter plot (Figure 3.9) indicates by way of its linear regression lines that the CM has a slightly lower bias, albeit with a wide spread of points for both models. Similar to CAO1, despite the reversed atmosphere-ocean temperature gradient, the CM is closer to truth in WAI1. In fact, the UCM performs substantially poorer than in the CAO cases, with a significant warm bias for virtually the whole time series. Again, this could be linked to the cooler *SST* upwind of the ship's location in the CM but may also hint of the UCM performing less well under more stable conditions.

Relative Humidity

In the CAO cases, at T+84 hours, over the open ocean the near-surface relative humidity (RH_{2m}) differs little between the CM and the UCM, despite the cooler T_{2m} (Figures 3.7 and 3.8). Though, sporadic patches of lower RH_{2m} in the CM correlate with areas of larger difference between model T_{2m} fields. In WAI1 the difference between the model's RH_{2m} fields appears to consistently correlate with that of T_{2m} (Figure 3.6). The same expected relationship occurs near the Greenland coast in all of the cases, with areas of increased RH_{2m} relating to increased T_{2m}. As is the case in the T_{2m} field, the standout difference between the models occurs over the outer MIZ.

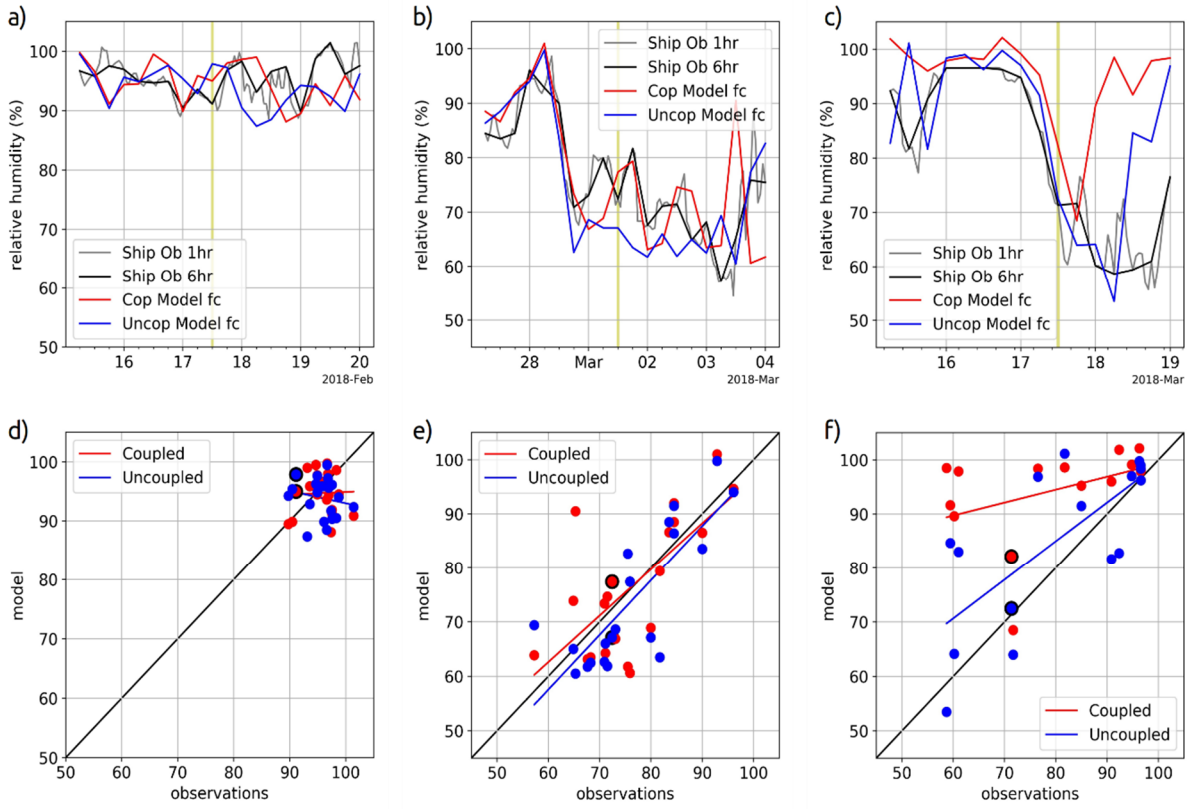

Figure 3.11 As Figure 3.8 for 2 m relative humidity.

In fact, for RH_{2m} the existence of sea ice, and the consequent higher value for z_{0q}, results in a much greater flux of moisture into the atmosphere in CAO1 along the entire outer MIZ, with values up to 50% higher in the CM (e.g., Figure 3.7). This, at least in part, explains the similarity between RH_{2m} model fields further downstream, whereby the competition between increased moisture input to the atmosphere and effect of lower T_{2m} appear to balance each other out.

In CAO2 the band of increased RH_{2m} in the CM is less extreme (Figure 3.8). Spatially, this is partly limited by the CAO airmass not extending far to the south. The reduced magnitude may be due to the smaller difference between the persistent and CM sea ice fields in this case as discussed in Section 3.1. Nonetheless, the outer MIZ and its z_{0q} value appear to have a significant impact, as well as the balancing out of RH_{2m} values downstream by lower T_{2m}.

The CM outer MIZ in WAI1 appears to have little to no impact on RH_{2m} (Figure 3.6). But this is as expected with the incoming airmass having equilibrated with the surface over its long ocean fetch, hence near saturation point. This is confirmed by looking at the time series of RH_{2m} observations at the ship, which are consistently >90% (Figure 3.11). As a result, model forecasts of near saturation are both accurate at the ship for the duration of WAI1.

Comparison of time series at the ship during CAO1 is similar to that of T_{2m}, where despite lower T_s, the increased flux of moisture into the atmosphere over the MIZ results in a more accurate CM RH_{2m} forecast at the ship downstream of the MIZ (Figure 3.11). However, these competing errors do not balance so neatly in CAO2, with the CM near-surface atmosphere becoming too moist. This is most clear from 17 March 2018 18:00 UTC to the end of the forecast, where the ship is in the outer MIZ in the CM and consequently RH_{2m} is forecast substantially higher than observed. Thus, it is evident that the higher setting of z_{0q} in the CM due to the presence of low concentration sea ice significantly affects moisture flux into the atmosphere.

3.4 Stationary box analysis

Two spatial sample boxes (see Figure 3.2) are designed to compare model outputs at strategic locations with observations in the local vicinity during CAO1 (Figure 3.12). Box A is situated over the meteorological buoy deployed during the IGP cruise, making use of near continuous hourly observations in an open ocean environment. Box B is placed to evaluate the region previously described to have low concentration sea ice in the CM but none in the UCM. Its position has been chosen to make use of available ship and aircraft observations while simplifying interpretation by using a fixed location, and so complementing the above analysis. This provides a means to challenge or corroborate findings made by sampling the models along the ship track, which as a constantly moving platform moved through different local conditions, particularly in and out of the MIZ. This alternative method serves to increase the number of observations used and the robustness of earlier findings. For further rigour three forecast initialisations have been used to improve reliability of findings and assess effects of increasing forecast lead time.

Each box contains 35 model grid points, over which each diagnostic has been averaged for each available time step. The box size, roughly 35 km by 50 km, has been selected to capture a useful number of observations in Box B. The same size has been used for Box A for fair comparison, even though a single nearest gird point could have been used for comparison. The resulting time series are then compared with the available observations. It should be noted that due to the observation platforms being on-the-move, the number of available measurements in Box B are limited and fewer than those available from the continuous time series at the meteorological buoy in Box A. It has been found in earlier analysis that due to an extended band of <15% concentration sea ice, a band of cold biased T_s exists in the CM.

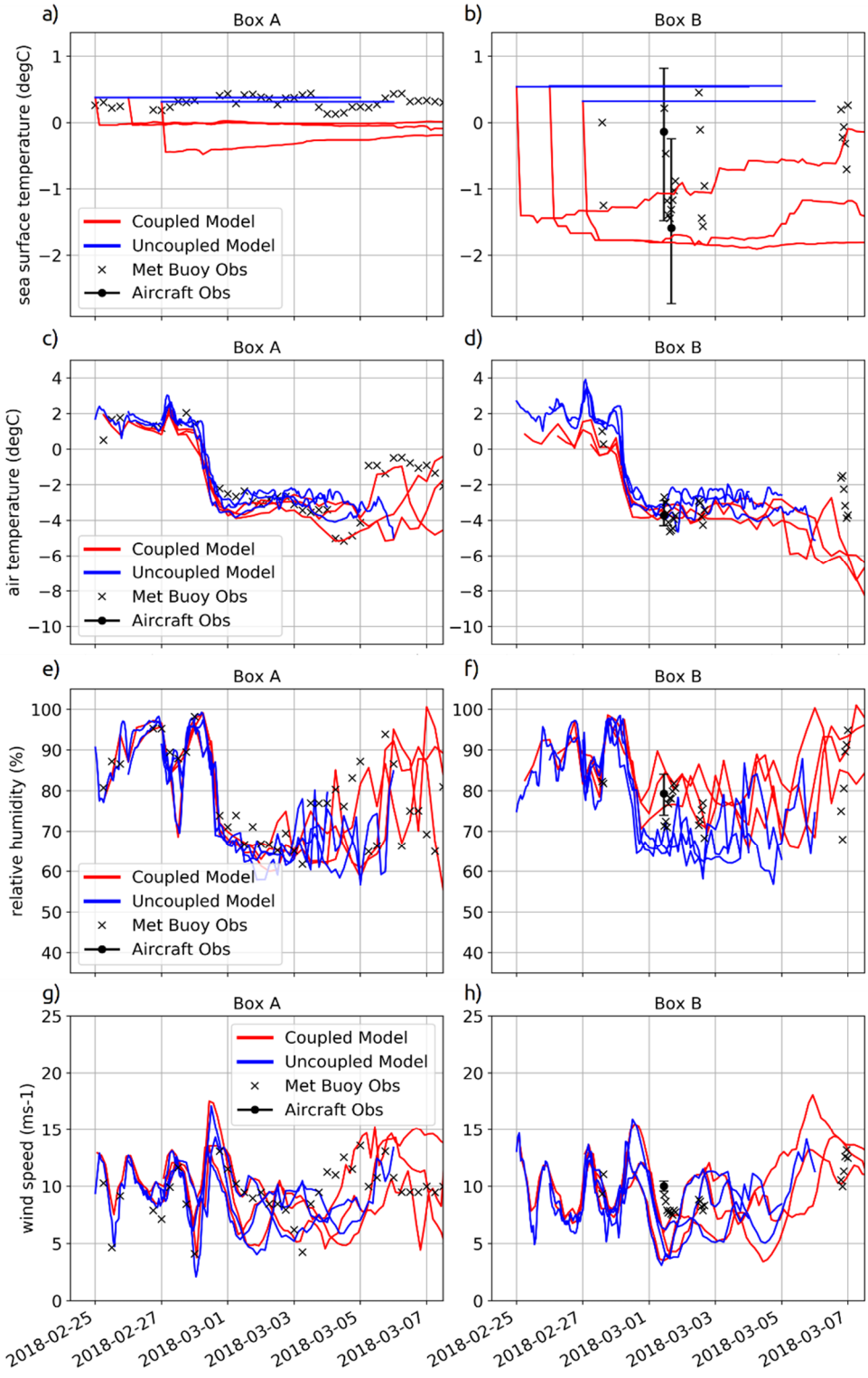

Figure 3.12 Analysis of time series from the coupled model (red) and the uncoupled model (blue) for Box A (left column) over the meteorological buoy in the open ocean and Box B (right column) at the edge of the marginal ice zone using observations from the meteorological buoy in Box A and aboard the *Alliance* in Box B (black crosses) and from the research aircraft (black circles showing leg mean; black bars showing leg range); for a) and b) sea surface temperature, c) and d) 2 m air temperature, e) and f) relative humidity, and g) and h) 10 m wind speed.

Figure 3.12 confirms that a cold bias exists, both in Box A over the open ocean and Box B at the MIZ edge. The stepwise drop in the model forecast from its input analysis as the ocean model spins up illustrates that the CM T_s bias is a product of its ocean and ice models, though it tends to converge with the persistent T_s field in the UCM with increasing lead time. In Box A the bias is small (< -0.5 °C), but if found to be consistent over the wider open ocean could have a significant impact on ocean-atmosphere exchange. Box B reiterates earlier comparisons with the ship, with the majority of the box containing low concentration sea ice in the CM bringing the area averaged T_s towards freezing point. The observations generally lie between the persistent UCM T_s field and the CM predictions. This demonstrates the weakness of the overly smooth CM MIZ, which doesn't reflect the true sea ice distribution and its sporadic patches of sea ice and open water.

Comparing T_{2m} in the two boxes shows that the CM tends to predict slightly lower air temperatures, more so at the MIZ fringe, and is arguably more consistent with observations during the CAO. This in part reflects the difference in the model T_s fields, but the fact that the magnitude of the difference between the models isn't larger in Box B may be attributed to the increased upward flux of heat due to the higher z_{0T} due to the presence of the low concentration outer MIZ in the CM. Before the CAO arrives at the two sample regions, RH_{2m} is in very close agreement between the models. In Box A this continues for the first few days after the cold front passes the meteorological buoy though the models appear to begin diverging with the CM surface layer air becoming moister in line with observations. However, in Box B the CM is immediately more humid during the CAO and shows significantly better agreement with observations. As for T_{2m}, despite cold biased T_s, the higher z_{0q} appears to increase upwards moisture flux resulting in more accurate RH_{2m} values than the UCM. It should be remembered for both boxes that the changing sea ice position and concentration in the CM upstream of these observation sites is having an influence on the differences between the models.

In earlier sections model winds have not been evaluated as the CM and UCM simulate very similar wind conditions, as illustrated in Figure 3.11. The very similar time series of wind speed in the two models in Boxes A and B is expected as they use the same initialisation data, dynamical engine, horizontal grid resolution and surface momentum exchange parameterisation. The different model sea ice distributions in Box B have a much smaller influence on wind speed than for T_{2m} and RH_{2m}. It is difficult to say from these results which model is more accurate, but both perform reasonably well compared with the in-situ observations.

3.5 Discussion

During CAO conditions in CAO1 and CAO2 the air flow to the position of the ship has been modified by the MIZ. In CAO2, the ship spends a good deal of time around the edge of the MIZ, which places it in the outer MIZ (<15% SIC) that exists in the CM but not the UCM. Comparatively, during WAI1 the air mass arriving at the ship has not been modified by the MIZ, though the ship does briefly enter the outer MIZ region in the CM. These differences between the cases enable an assessment of the impact of the representation of the MIZ in each model on the near-surface meteorology.

The surface temperature (T_s) in the CM is consistently cold biased compared to observations made by the research vessel *Alliance* (Figure 3.8), with bias values of –0.72 °C, -1.98 °C and –0.65 °C for CAO1, CAO2 and WAI1 respectively. In comparison, T_s in the UCM was more accurate overall, with biases of 0.44 °C, -0.58 °C and 0.12 °C (in above order). Similarly, RMSE values are consistently higher for the CM (Table 3.1).

From this is can be gathered that, despite the assumption of persistence, the UCM ocean T_s field remains more accurate and the CM representation of T_s around the MIZ is problematic. Visual analysis of model sea ice fields suggests that the dynamic sea ice in the CM is advantageous over the persistent field in the UCM. Hence, it seems a disparity exists in the evidence considered here, where the beneficial sea ice forecasting capability of the CM does not translate to the T_s field, which is important for forecasting near-surface meteorology. A vital next step in this work is to quantify the accuracy of the CM sea ice field. As sea ice concentration measurements were not made aboard the *Alliance*, a verification technique that uses satellite-based observations could be used, such as calculating the spatial RMSE (e.g., Collins, 2002; Day et al., 2014a; Keeley & Mogensen, 2018) or the Integrated Ice Edge Error (IIEE; Goessling et al., 2016).

		CAO1		CAO2		WAI1	
		UCM	CM	UCM	CM	UCM	CM
T_s (°C)	Bias	**0.44**	-0.72	**-0.58**	-1.98	**0.12**	0.65
	RMSE	**0.63**	0.96	**1.38**	2.42	**0.37**	1.12
T_{2m} (°C)	Bias	0.61	**0.02**	0.84	**0.15**	0.90	**0.37**
	RMSE	0.83	**0.52**	**2.23**	2.69	1.06	**0.75**
RH (%)	Bias	-2.35	**0.23**	**4.78**	14.04	-1.71	**-0.91**
	RMSE	**7.71**	9.07	**11.89**	19.39	4.99	**4.48**

Table 3.1 Bias and RMSE for predictions from the coupled and uncoupled models compared to observations aboard the *Alliance* of sea surface temperature, 2 m air temperature and 2 m relative humidity (as displayed in Figures 3.8, 3.9 and 3.10 respectively). Numbers in bold highlight which of the two models is more accurate in each case study.

Keeley & Mogensen (2018) found that the sea ice model used in the ECMWF HRES forecast was advantageous in summer and autumn over the Arctic during the time the sea ice undergoes most change, but not so during winter and spring; RMSE scores in the Iceland and Greenland Sea were neutral or worse in all seasons. The IIEE verification technique used by Goessling et al. (2016) is more sophisticated in that it can be decomposed into absolute extent error and misplacement error; hence it will be applied in further evaluation presented in Chapter 4. Indeed, it is instantly obvious in all of the spatial T_s charts presented in this study that the CM features a cold band where the outer MIZ appears in the CM but not the UCM. This represents a wide region of very low concentration sea ice, with T_s at freezing point accordingly. *SST* observations from the *Alliance* show that this region is poorly simulated. The GC2 configuration, at climate timescales, has been shown to have little T_s bias in the northern North Atlantic (Williams et al., 2015). However, the evidence presented in this study shows that over short-range forecasts in the locale of the MIZ T_s can be significantly biased.

Another problem of the outer MIZ in the CM arises from the assumed surface roughness value over the MIZ (z_{0_MIZ}). z_{0_MIZ} is assumed to have a constant value of 0.1 m, which is approximately 2 to 3 orders of magnitude higher than that of the neighbouring ice-free ocean surface. Hence, the CM features a band with significantly higher roughness length along the MIZ edge. With the basic relationship for scalar roughness lengths for heat and moisture: $z_{0T\_MIZ} = z_{0q\_MIZ} = 0.2 \times z_{0\_MIZ}$, there is a clear impact on predicted T_{2m} and RH_{2m}. Renfrew et al. (2019b) evaluate the MetUM GL6.0 surface exchange configuration with this scalar roughness parameter (used in operational forecasts prior to September 2018), denoting it the 'rough' experiment, alongside two other configurations: an older 'smooth' setup, with $z_{0\_MIZ} = 0.5 \times 10^{-3}$ m (with z_{0T_MIZ} and z_{0q_MIZ} calculated in the same manner), and another more sophisticated parameterisation scheme for surface exchange based on the work of Lüpkes et al. (2012) and Elvidge et al. (2016). The 'rough' experiment, with the same parameters as the model configurations in this study, in forecast evaluations over the MIZ in the Barents Sea and Fram Strait, performed worst with larger bias and RMSE for all variables except specific humidity. Evidence in this study adds to the conclusion by Renfrew et al. (2019) that further research is required to accurately and individually define scalar roughness length parameterisations. The Lüpkes - Elvidge scheme was employed for Met Office operational forecasting in September 2018, but not used in the updated Global Coupled model version 3.1 (GC3.1), hence investigation of GC3.1 in the following chapter includes an experimental configuration that trials the Lüpkes - Elvidge scheme.

Substantially increased turbulent heat fluxes occur in the CM over the MIZ due to its high value for z_{0_MIZ}. A quick calculation for sensible heat flux demonstrates the effect of increasing z_{0_MIZ}.

Following the Monin Obukhov similarity theory, sensible heat flux can be calculated following the bulk aerodynamic formulae:

$$C_{HN} = \frac{\kappa^2}{\ln(z/z_{0MIZ})\ \ln(z/z_{0TMIZ})},$$

$$SH = c_p\,\rho\,C_{HN}\,U\,(T_s - T_a),$$

where κ is the von Karman constant (0.4), z is the reference height (10 m), $z_{0T\_MIZ} = 0.2 \times z_{0\_MIZ}$ in GSI6.0, c_p is the specific heat capacity of air (1004 J kg^{-1} K^{-1}), ρ is the density of air (1.3 kg m^{-3}), U is wind speed and $T_s - T_a$ is the surface-air temperature difference. Selecting 00:00 UTC 18 March 2018 as an example, when the *Alliance* was near the MIZ, observations were approximately U = 8 m s^{-1}, T_s = 0 °C and T_a = -6 °C. Aircraft observations during the IGP campaign around the edge of the MIZ (0 % to 25 % sea ice concentration) found C_{HN} to be typically around 0.0005 (Elvidge et al., 2022). Computing upward sensible heat flux using these values gives around 31 W m^{-2}. However, performing the same calculation for the CM, with the *Alliance* in the CM outer MIZ so that z_{0_TMIZ} = 0.2 × (0.1 m) = 0.02 m, hence C_{HN} = 0.0056 and T_s = -1.8 °C, finds the sensible heat flux to be around 246 W m^{-2}. In this example, the much rougher surface prescribed in the model MIZ increases upward sensible heat flux by a factor of 8, despite a reduced surface-air temperature difference in the CM.

The accuracy of predicted T_{2m} and RH_{2m} in the CAO cases presented is significantly impacted by the simulated MIZ, with two main factors involved. First, the distribution of the dynamic MIZ >15% in the CM appears to improve over the persistent sea ice field in the UCM, but the existence of excessive low concentration sea ice causes a significant problem. The effect of the low concentration sea ice in the outer MIZ is greater exchange of heat and moisture from the surface to the atmosphere. However, the results are different for the accuracy of model predictions of T_{2m} and RH_{2m}. The enhanced surface fluxes due to the model representation of the MIZ is partly offset by the lower model T_s in this region. In numerical weather prediction, there are competing errors where two or more problems sometimes coincidentally result in an apparently accurate prediction of a variable. This problem is apparent in the significantly lower bias scores for T_{2m} in the CM predictions compared to the UCM for all three case studies (Table 1). Bias scores for RH_{2m} are also lower for CAO1 and WAI1; but for CAO2, when the ship spent more time in the location of the outer MIZ predicted in the CM, there is a large positive bias for RH_{2m}, further evidencing the impact of the overly strong upward moisture transfer into the atmosphere. With the long fetch over the ocean for the airmass arriving at the ship in WAI1 the CM provides a marginally better forecast for the atmospheric variables.

Overall, whether under CAO conditions or not in the case study periods considered, the CM tends to do a better job of predicting T_{2m} and RH_{2m}. However, underlying competing errors undermine this result, and problems caused by the existence of a wide outer MIZ in the CM result in cold biased T_s and scalar roughness lengths being set too high where this ice is forecast.

3.6 Conclusions

Three cases studies have been examined in the Iceland and Greenland Seas, comparing numerical weather prediction output from the uncoupled Met Office global operational forecast system (UCM) and a coupled model version (CM) featuring ocean-ice-atmosphere interaction. The forecasts are evaluated with novel in-situ observations from the Iceland Greenland Seas Project (IGP), aiming to determine whether the dynamic sea ice field in the CM marginal ice zone (MIZ) leads to improved forecast skill.

A consistent wide outer MIZ of low concentration sea ice (<15% SIC) in the CM causes cold biased T_s. However, the high value of surface roughness over the MIZ (z_{0_MIZ} = 0.1 m) leads to elevated surface fluxes of heat and moisture compared to the UCM. Despite these competing errors, the CM does in fact show some improvements in forecasting near-surface air temperature (T_{2m}) and relative humidity (RH_{2m}). Overall, the significant differences in the CM meteorology that are due to its dynamic sea ice evidence that accurate simulation of the MIZ is of critical importance in subpolar North Atlantic region. However, further work is required to disentangle these problems and make specific suggestions for improvement. Another consideration not covered in detail in this study is the effect of feedback between the ocean and the atmosphere, for example the cooling of the ocean surface during a CAO period, and whether this is accurately represented by the CM. Despite the dynamically and thermodynamically evolving MIZ in the CM appearing qualitatively more accurate than the persistent sea ice in the UCM, there is more work to be done to verify the skill of the sea ice forecasts. This provides strong motivation for the following chapter, in which sea ice forecasts from a newer version of the CM are evaluated.

Further development of the CM ocean-ice modelling system to more accurately simulate ice dynamics would be beneficial. But this is limited by the accuracy of observations used to initialise the model, which are poorest over low concentration sea ice due to limitations of current microwave sensing technology. A useful approach in the short-term would be to implement a more representative parameterisation of scalar roughness values for heat and moisture over the MIZ. The evidence presented in this study clearly illustrates that the overly simplified assumption of a blanket z_{0_MIZ} value of 0.1 m is unsuitable for use in surface exchange

parameterisation of moisture and heat, particularly where the sea ice is of very low concentration.

The results presented in this chapter were conveyed to the Met Office through regular meetings and contact with Tim Graham (Manager of Global Coupled Model Development and Processes). The Met Office were keen to receive this feedback and benefit from the valuable insights from evaluation using the IGP observational dataset. The evidence that the simulated MIZ was consistently too wide, with bias in T_s and elevated surface fluxes, added impetus to plans for improved sea ice simulation in GC3.1. Building on this work, Tim Graham assisted by running experimental simulations using GC3.1 and continued to attend formal PhD review meetings in order to keep abreast of new analysis and results.

4 Quantitative analysis of short-range sea ice forecasts from the Met Office Global Coupled model (GC3.1)

4.1 Introduction

During cold-air outbreaks (CAOs) the location and concentration of the marginal ice zone (MIZ) has a strong influence on the distribution and intensity of surface fluxes of momentum, heat and moisture. These fluxes are greatest just downstream of the sea ice where the air-sea temperature gradients are strongest, demonstrated by observational evidence (e.g., Brümmer, 1997; Renfrew & Moore, 1999), in reanalysis datasets (e.g. Moore et al., 2012; Papritz and Spengler, 2017) and in numerical modelling (Liu et al., 2006; Spensberger & Spengler, 2021). In turn, these fluxes influence the atmospheric boundary layer and mesoscale weather system development. In model studies, the development of convective roll clouds has been shown to be dependent on the structure of the MIZ (Liu et al., 2006; Gryschka et al., 2008) and the development of polar lows is influenced by the location of the ice edge (Sergeev et al., 2018). Furthermore, climate change has already caused accelerating reductions in Arctic sea-ice extent, particularly in summer (Comiso et al., 2008; Yadav et al., 2020), and the retreating sea ice edge in winter in the Iceland and Greenland Seas is responsible for significant reductions in ocean-atmosphere heat exchange (Moore et al., 2015). The opening of trans-Arctic shipping routes is increasing demand for reliable short-range weather and sea ice forecasts (Melia et al., 2016). Improving sea ice prediction capability is also essential for global weather forecasting, particularly under the rapidly changing conditions in the Arctic and sub polar regions (Smith et al., 2015; Jung et al., 2016).

In the past, a persistent sea ice field for short-range weather forecasting was deemed a reasonable assumption. However, in the last decade a new generation of model systems featuring coupled ocean-ice-atmosphere interactions have been developed for short-range weather forecasting. The potential benefits of dynamic sea ice, such as more accurate prediction of the strongest turbulent heat fluxes near the ice edge, is a key motivation for coupled models (e.g., Keeley and Mogensen, 2018). The UK Met Office have been through several iterations of a coupled model configuration, aiming to transition to a coupled operational forecast in 2022. Their Global Coupled model 3.1 (GC3.1) evaluated here represents the Met Office's pre-operational test version, thus it is vital to verify its forecast skill to provide feedback. Previous

evaluations of GC3/3.1 typically take a large-scale approach at seasonal to annual time scales (e.g., Williams et al., 2017; Ridley et al., 2018; Storkey et al., 2018). This wide angled approach is common. Modelling efforts are often concerned with seasonal to interannual sea ice prediction and predictability (e.g. Stroeve et al., 2014; Blanchard-Wrigglesworth et al., 2016; Petty et al., 2017; Zheng et al., 2021), or long-range climate sensitivity (e.g., Kay et al., 2015; Notz et al., 2016; Meredith et al., 2019; Fox-Kemper et al., 2021), which have been particularly motivated by models inaccurately simulating the rate of sea ice loss in the Arctic (Stroeve et al., 2007; Vihma, 2014).

Here we focus on short-range sea ice forecasts, using several case studies where observational data are available from the Iceland Greenland Seas Project (IGP) in winter 2018 (Renfrew et al., 2019a). Short-range sea ice forecasting has only recently received significant attention as coupled models have started to demonstrate appreciable skill. A few notable coupled modelling systems developing useful sea ice prediction capability include the European Centre for Medium-range Weather Forecasting (ECMWF) Integrated Forecast System (IFS) (Sarojini et al., 2019), the Canadian Meteorological Centre's Global Ice Ocean Prediction System (GIOPS) (Smith et al., 2016), the U.S. Office of Naval Research's Marginal Ice Zone Modeling and Assimilation System (MIZMAS) (Schweiger & Zhang, 2015) and also the U.S. Navy Arctic Cap Nowcast/Forecast System (ACNFS) (Hebert et al., 2015).

Numerous sea ice verification techniques have been used by others, typically focusing on sea ice extent or volume (e.g., Smith et al., 2016). The MIZ width has been identified as a fundamental length scale for climate and polar ecosystem dynamics (e.g., Stroeve et al., 2016). Strong & Rigor (2013) found a 40% widening trend of the Arctic MIZ and a small narrowing in winter, motivating analyses of oceanic versus atmospheric and thermodynamic versus dynamic drivers of changes to the MIZ. The importance of the position of the ice edge has motivated some groups to use a metric that finds the mean distance between the forecast and observed ice edge (e.g., Posey et al., 2015; Dukhovskoy et al., 2015), however, this approach is overly sensitive to isolated patches of sea ice. This led Goessling et al. (2016) to develop a novel Integrated Ice Edge Error (IIEE) metric, which is calculated by finding the symmetric difference between the areas enclosed by the forecast and observed ice edge. The IIEE is particularly useful for end users for whom the ice-edge position is more important than a measure of ice extent (e.g., Tietsche et al., 2014).

Prediction of the ice edge position, and hence the location of the strongest heat fluxes, is dependent on the representation of sea ice dynamics in coupled numerical models. We evaluate GC3.1 in several different configurations, testing ocean model grid resolutions of 1/4° and 1/12°,

and with an alternative atmospheric drag setting over the MIZ. Two sea ice concentration products, AMSR2 and OSTIA, are for verification. In Section 4.2 the model versions and verification product characteristics are described, and the selection of case study periods are introduced. Section 4.3 features an evaluation of the verification products themselves using IGP observations, then presents the results of the IIEE analyses with decomposition into its components. Section 4.4 provides further discussion and concluding remarks are given in Section 4.5.

4.2 Data and Methods

4.2.1 GC3.1 Model Experiments

Three ten-day forecast periods are evaluated during February to April 2018, matching the time of the IGP field campaign. The model used to generate these is the Met Office Global Coupled 3.1 (GC3.1) science configuration with Global Atmosphere 7.1, Global Land 7.0, Global Ocean 6.0 and Global Sea Ice 8.1 (see Williams et al., 2017). The atmosphere has 85 vertical levels, with a top at 85 km, and a horizontal resolution of N1280, or around 10 km in the midlatitudes. In comparison to the GC2 science configuration evaluated in the previous thesis chapter, GC3.1 features the introduction of multilayer sea ice (4 layers), a new multilayer snow scheme, and various revisions to parameterisation schemes in all model components. The model was run at two ocean resolutions of 1/4° and 1/12° (ORCA025/ORCA12). The higher resolution ocean model permits a range of eddy activity (Marzocchi et al., 2015), while the 1/4° is too coarse to represent most eddies.

GC3.1 features a surface drag parameterisation scheme over the MIZ that employs a fixed value for aerodynamic roughness length of $z_{0\_MIZ} = 100 \times 10^{-3}$ m, which is the same as used in GC2. Using this value has been found to cause considerable initialisation shock in GC2, resulting in significant initialisation error (Johns et al., 2021). Our earlier findings suggested that this value for z_{0_MIZ} and the scalar roughness lengths for heat and moisture, which are fixed at $0.2 \times z_{0\_MIZ}$, were too high and partly responsible for elevated model T_{2m} and RH_{2m} predictions at the position of the IGP research vessel. To further investigate the transport of sea ice due to wind, an additional modified version of the ORCA025 model was run with a modified sea ice drag parameterisation scheme, which is taken from the global operational uncoupled model configuration (Global Land 8.0). This updated scheme represents a reduced drag coefficient over sea ice that peaks over the MIZ and more closely matches field observations (Elvidge et al., 2016). It has also been shown to have a beneficial impact on simulated T_{2m} and surface fluxes

near the MIZ and positively affects the entire atmospheric boundary layer (Renfrew et al., 2019b). It is planned that this drag parameterisation scheme will be employed in the next configuration of this coupled model, GC4, which is planned for operational forecasting, so testing its efficacy here is valuable.

In the coupled model forecasts the previous day's OSI-SAF 401 satellite sea ice concentration product (described further in Section 4.2.5) is used to initialise the ocean model, which is then spun up for 3 hours. The resultant ocean and sea ice fields are then supplied to the atmosphere model at T+0 hours. Thus, despite originating from the same data source, there is a 24-hour lag and some processing between the model sea ice field at T+0 hours and the OSTIA product used to verify at this time. We also analyse forecasts with a persistent sea ice field (as currently used in the operational system), to allow an estimate of the value of dynamic sea ice. As we are only evaluating model sea ice, this experiment is set up by taking the initial field at T+0 hours from the 1/4° model and fixing this throughout all time steps for each forecast.

In summary, the experiments evaluated here:

A) Persistent sea ice control experiment

B) 1/4° ocean model (ORCA025)

C) 1/4° ocean model with modified surface drag (ORCA025_mod)

D) 1/12° ocean model (ORCA12)

In all experiments the atmospheric model resolution and science configuration are identical.,

4.2.2 Forecast periods

Three 10-day forecast periods were selected from the IGP field campaign period initialised at 00Z: 17 February 2018, 1 March 2018 and 1 April 2018. For technical and computational reasons, only a limited number of forecasts were available for analysis. Hence, we employ this case study approach and investigate each case in detail. Earlier work (Chapter 3) described that during mid-February 2018, corresponding with the first leg of the IGP research vessel cruise, a southerly warm and moist airmass was flowing into the Iceland and Greenland Seas region, commonly called a Warm Air Intrusion (WAI; Pithan et al., 2018). From 1 March 2018 the synoptic pattern reversed with the outflow of a cold and dry airmass from the north. This cold-air outbreak (CAO) was weak to moderate in intensity but persisted for 10 days, allowing a wealth of atmosphere and ocean measurements to be made by the ship on its second leg, by a meteorological buoy and by numerous aircraft science flights. These observations enabled an evaluation of near-

surface meteorological predictions from the Met Office uncoupled operational forecast system and GC2 in Chapter 3 (also see Renfrew et al., 2021), which provided motivation for further verification of the coupled model sea ice forecasts presented here. A second brief but intense CAO occurred around 1-4 April 2018 suggesting a further forecast period for comparison, however, this was only observed by the meteorological buoy towards the end of the IGP field campaign. After the initial CAO phase, this forecast featured weak winds that fluctuated between northerly and southerly.

4.2.3 Spatial and temporal basis for case study analysis

The spatial area chosen for this analysis was also selected to be relevant to the IGP field campaign region. The northern boundary is set at 75° N, roughly level with the centre of the Greenland Sea Gyre. This point marks a change in the sea ice regime along the East Greenland coast, where the zonal distribution of the sea ice flowing out of the Fram Strait has been shown to approximately half in width from 79° N to 75° N, creating a local minimum in MIZ width and a change of velocity (Martin & Wadhams 1999). The southern boundary is set at 68° N, marking the beginning of the Denmark Strait and the end of the East Greenland Current's passage through the Iceland Sea. This relatively small domain is in contrast to most seasonal sea ice forecast evaluations which tend to evaluate the entire Arctic (e.g., Sigmond et al., 2013; Petty et al., 2017; Barton et al., 2021) or Antarctic (e.g., McLaren et al., 2006; Bushuk et al., 2021; de Vos et al., 2021). This geographic limitation allows us to attribute model biases in sea ice concentration with local air-sea-ice processes.

4.2.4 Aircraft observations

A further advantage of the temporal and spatial selections for this study is the availability of an observational sea ice concentration dataset from the IGP aircraft, which can be used to verify the two satellite sea ice products. Science flights took place during March 2018 over and near the MIZ in the northwest Iceland Sea, typically involving low level legs transiting the sea ice edge, stacked runs within the atmospheric boundary layer and sawtooth profiles. All the measurements used took place within the spatial region used in this analysis. Sea ice concentration, A, is calculated using a proxy based on surface albedo, α, from upwelling and downwelling short-wave radiation measurements ($\alpha = SW_U / SW_D$). This method, documented by Elvidge et al. (2016), relies on the sea ice being more reflective than sea water, with tie-points derived through careful review of onboard video footage for the *no ice transition* from open water to sea ice ($A \rightarrow 0$) and the *all ice transition* between continuous ice and some water appearing ($A \rightarrow 1$). From careful review of video footage onboard the aircraft the tie-points used

are $a_{A\rightarrow 0}$ = 0.15 and $a_{A\rightarrow 1}$ = 0.85. Thus, ice fraction can be calculated for each instantaneous measurement of albedo by

$$A_a = \begin{cases} 0 & \text{for } a \leq a_{A\rightarrow 0} \\ \dfrac{(a - a_{A\rightarrow 0})}{a_{A\rightarrow 1} - a_{A\rightarrow 0})} & \text{for } a_{A\rightarrow 0} < a < a_{A\rightarrow 1} \\ 1 & \text{for } a \geq a_{A\rightarrow 1}. \end{cases}$$

This technique has also been shown to be in good agreement with a parallel method using surface temperature (Elvidge et al., 2016). Detailed information on the British Antarctic Survey Twin Otter aircraft instrumentation, including the upward- and downward-facing pyranometers used to derive albedo, is available in Weiss et al. (2011) and Weiss et al. (2012). A description of the IGP flight campaign is provided by Renfrew et al. (2019) and further details on data quality control and processing are in Renfrew et al. (2021) and Elvidge et al. (2021).

4.2.5 Satellite sea ice products

The Operational Sea Surface Temperature and Ice Analysis (OSTIA) is produced by the Met Office. It uses the OSI-SAF 401 global sea ice concentration derived from remote sensing observations from the Special Sensor Microwave Imager/Sounder (SSMIS). Several SSMIS observation nodes are analysed on the 10 km OSI SAF grid with each observation having a radius of influence of 75 km using a Gaussian weighting scaled with the footprint spatial resolution (3-dB footprint size: 69 x 43 km at 19.35 GHz, 37 x 28 km at 37.0 GHz). This is regridded by OSTIA to produce a daily product with a 6.25 km grid resolution (Donlon et al., 2012). Recent work has demonstrated that the OSTIA sea-ice distribution is relatively smooth, compared to aircraft observations and other products (Renfrew et al., 2021).

The Advanced Microwave Scanning Radiometer 2 (AMSR2) sea ice concentration was obtained from the University of Bremen data archive (Melsheimer and Spreen, 2019). AMSR2 is retrieved from JAXA satellite GCOM-W1 brightness temperatures using the ARTIST Sea Ice (ASI) algorithm (Spreen et al., 2008). The resultant swath data (3-dB footprint size: 22 x 14 km at 18.7 GHz, 12 x 7 km at 36.5 GHz) is resampled onto a polar stereographic grid with 6.25 km resolution providing a daily analysis product that is higher resolution than OSI-SAF 401. In AMSR2 ice concentration is calculated using the Bootstrap algorithm (Comiso, 1986), which uses the 18 and 37 GHz channels as they have the lowest sensitivity to atmospheric phenomena over open water. The ASI algorithm adjusts this output by setting ice concentration below 5% to 0% due to the coarser sensor resolution using these microwave channels, which provides a sharper concentration gradient at the sea ice edge.

OSI-SAF also makes use of the Bootstrap technique, but due to evidence from Andersen et al. (2007) that using the Bristol algorithm (Smith 1996) at low frequency microwave channels gave best agreement with higher resolution Synthetic Aperture Radar (SAR) imagery, a hybrid of these two algorithms is used. Due to their relative strengths, the Bristol algorithm is given little weight at concentrations below 40% and the Bootstrap is given little weight at concentrations above 40%. The Bootstrap algorithm is based on the observation of linear clustering of brightness temperatures measured using the 19 and 37 GHz channels in the vertical plane, $T_{19v,}$ T_{37v}, to detect ice or open water, taking account of the variability to optimise the detection of low concentrations. The Bristol algorithm is similar, but also uses the brightness temperature in the horizontal plane of the 37 GHz channel, T_{37h}, to allow a three-dimensional view of the data using a transformed coordinate system.

4.2.6 The Integrated Ice Edge Error

Following Goessling et al. (2016), the Integrated Ice Edge Error (IIEE) method distinguishes between a forecast ice edge and a 'true' ice edge obtained from a verification product. The IIEE metric is defined as the area where the forecast and truth disagree on the ice concentration being above or below a defined threshold, typically taken as 15%. This is equivalent to the 'symmetric difference' between the areas enclosed by the forecast and verification ice edge. It is calculated by finding the areas where the local sea ice extent is overestimated (O) or underestimated (U) and then summing:

1) $$IIEE = O + U\,,$$

2) $$O = \int_A max(c_f - c_t, 0)\, dA\,,$$

3) $$U = \int_A max(c_t - c_f, 0)\, dA,$$

where A is the domain of interest, c = 1 where sea ice is above the prescribed concentration threshold (we use 0.01%, 15% and 50%), and c = 0 elsewhere, where c_f and c_t are c for the forecast and truth respectively. The IIEE can also be decomposed into an absolute extent error (AEE) and a misplacement error (ME):

4) $$IIEE = AEE + ME\,,$$

5) $$AEE = |O - U|,$$

6) $$ME = 2 \cdot min(O, U).$$

The AEE describes the absolute mean extent error and is comparable with the root mean square error metric of sea ice extent (e.g., Guemas et al., 2014). The AEE identifies situations where the forecasted sea ice extent is larger or smaller than the 'truth', i.e., when O >> U or U >> O the AEE is high. Conversely, the ME takes into account the position of the sea ice edge and the ice distribution separately from the total extent. Hence, the ME is particularly informative in situations where there are significant amounts of both overestimation and underestimation errors. If these errors are of similar magnitude, i.e., O ≈ U, while they cancel each other out to give a low AEE, the ME will be at a maximum. This highlights the issue where, despite the overall amount of forecasted sea ice being relatively accurate, it is misplaced and remains problematic for forecasting. Goessling et al. (2016) show that the often neglected ME makes up more than half of the climatological Arctic IIEE.

4.2.7 Methodology

Creating a single grid on which to transform the different sea ice and model products was a necessity. One option would be to pick one product's grid as the base, but whether to choose the verification product or the model to be tested is for debate. Thus, a new standard grid was established, set to be rectilinear with 0.06° grid length. During the evaluation, each product is regridded using bilinear interpolation to this common grid.

To evaluate the different sea ice products against each other a common land-sea mask was required due to significant differences in the representation of the coast and inland water regions (see Figure 4.1). This was created by taking the AMSR2 land-sea mask and converting any grid cell within a Von Neumann neighbourhood with a radius of five grid cells from a land cell to be also land. This created a 'conservative' land-sea mask that artificially extends the east coast of Greenland by approximately 30 km to the east. Additionally, several remaining water grid cells within the Scoresby Sund fjord were manually converted to land. This process also augmented the size of Jan Mayen Island, to remove any spurious sea ice that occurs along its coast. This land-sea mask was then applied to all the regridded datasets. This approach artificially reduces the area of sea ice in the domain. However, all of our results are based on comparing products, so the actual area is of no interest.

To compare the spatial similarity of each forecast timestep with that day's analysis the sea ice fields are first made binary. Where sea ice exists, the field is set to 1, otherwise open ocean grid cells are set to 0. The area enclosed by the forecast and the verification product is integrated by calculating the area of each grid cell for each criterion and summing (Equations 2 and 3).

A key decision is to decide what the minimum sea ice concentration threshold should be to determine whether a grid cell is assumed to be ice or not. This is typically taken as a threshold of 15% (Goessling et al., 2016) and this was used for the main part of the analysis. However, the procedure was also run with thresholds of 0.01%, to account for all sea ice, and 50% to account for the more 'solid' sea ice pack.

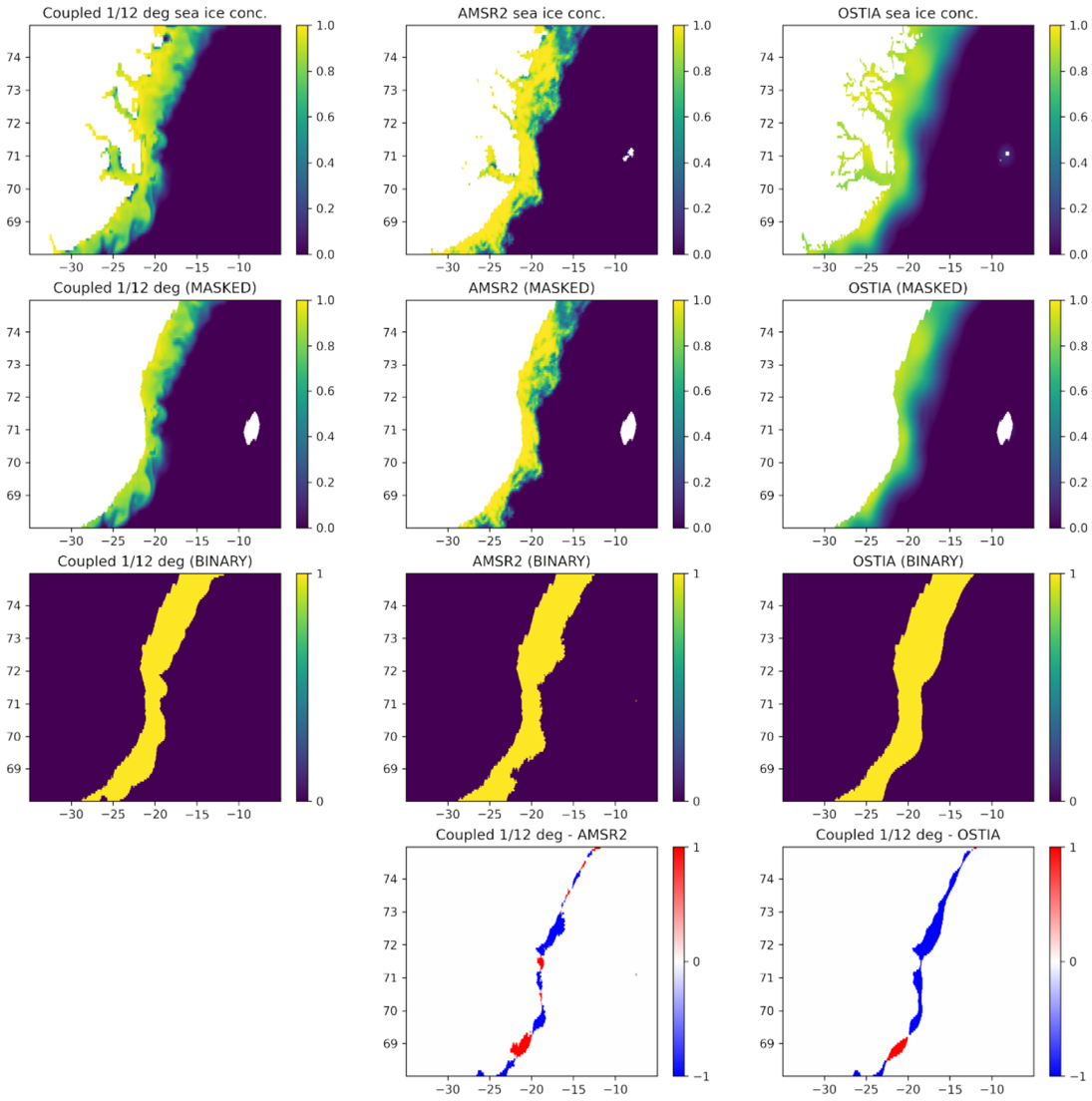

Figure 4.1 An example of the steps involved to process the initial sea ice fields from a forecast and verification product time step (row 1), by regridding and applying a common land mask (row 2), binarising the sea ice field depending on the selected minimum sea ice concentration threshold (row 3), then finding the over- and underestimated region of sea ice extent in the forecast for each verification product (row 4; red = overestimation, blue = underestimation). The example here is at T+84 hours from the 1 March 2018 forecast)

4.3 Results

4.3.1 AMSR2 and OSTIA verification

First, a verification of the AMSR2 and OSTIA products is presented using aircraft observations made during the IGP. Most of the aircraft measurements were made over or near the MIZ, particularly during science legs that transited the ice edge (Renfrew et al., 2019a), making the dataset ideal for comparison across the MIZ. The scatter plots of satellite derived sea ice concentration extracted by linear interpolation versus observations in Figure 4.2 illustrate that AMSR2 is generally more accurate than OSTIA. AMSR2 represents the variability significantly better than OSTIA with a closer standard deviation, lower RMSE and more accurate linear regression slope and correlation coefficient (see Table 4.1).

These results are corroborated by measurements made during the Aerosol-Cloud Coupling And Climate Interactions in the Arctic (ACCACIA) field campaign (Elvidge et al., 2016) as shown in Table 4.1. The low slope of the OSTIA regression line illustrates the problem caused by the Gaussian smoothing algorithm used to produce the OSI-SAF 401 product. The blurring of the sea ice edge results in less high concentration sea ice and more low concentration sea ice than observed. However, AMSR2 has a positive bias, while OSTIA has a slightly smaller negative bias. A cluster of points exist where AMSR2 estimates the sea ice concentration to be around 100%, while the measurements were up to 30% lower.

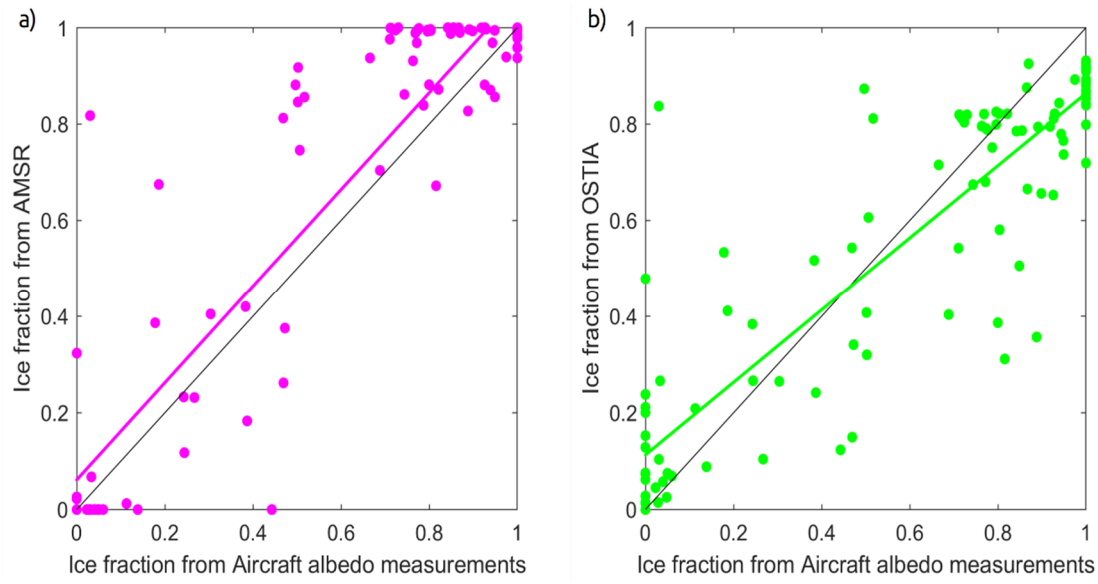

Figure 4.2 Scatter plots of aircraft observed sea ice fraction versus satellite derived fraction from AMRS2 and OSTIA, line shows a linear regression.

		Mean Obs.	Mean Prod.	Std. Dev. Obs.	Std. Dev. Prod.	Corr. Coeff.	Slope	Bias	RMSE
IGP	AMSR2	0.583	0.647	0.393	**0.426**	**0.927**	**1.004**	0.064	**0.171**
	OSTIA	0.583	**0.551**	0.393	0.333	0.885	0.751	**-0.032**	0.185
IGP and ACCACIA	AMSR2	0.595	0.65	0.366	**0.394**	**0.858**	**0.923**	0.055	**0.211**
	OSTIA	0.595	**0.55**	0.366	0.315	0.787	0.678	**-0.045**	0.231

Table 4.1 OSTIA and AMSR2 sea ice concentration verification statistics. Bold indicates a better performance compared to the observations.

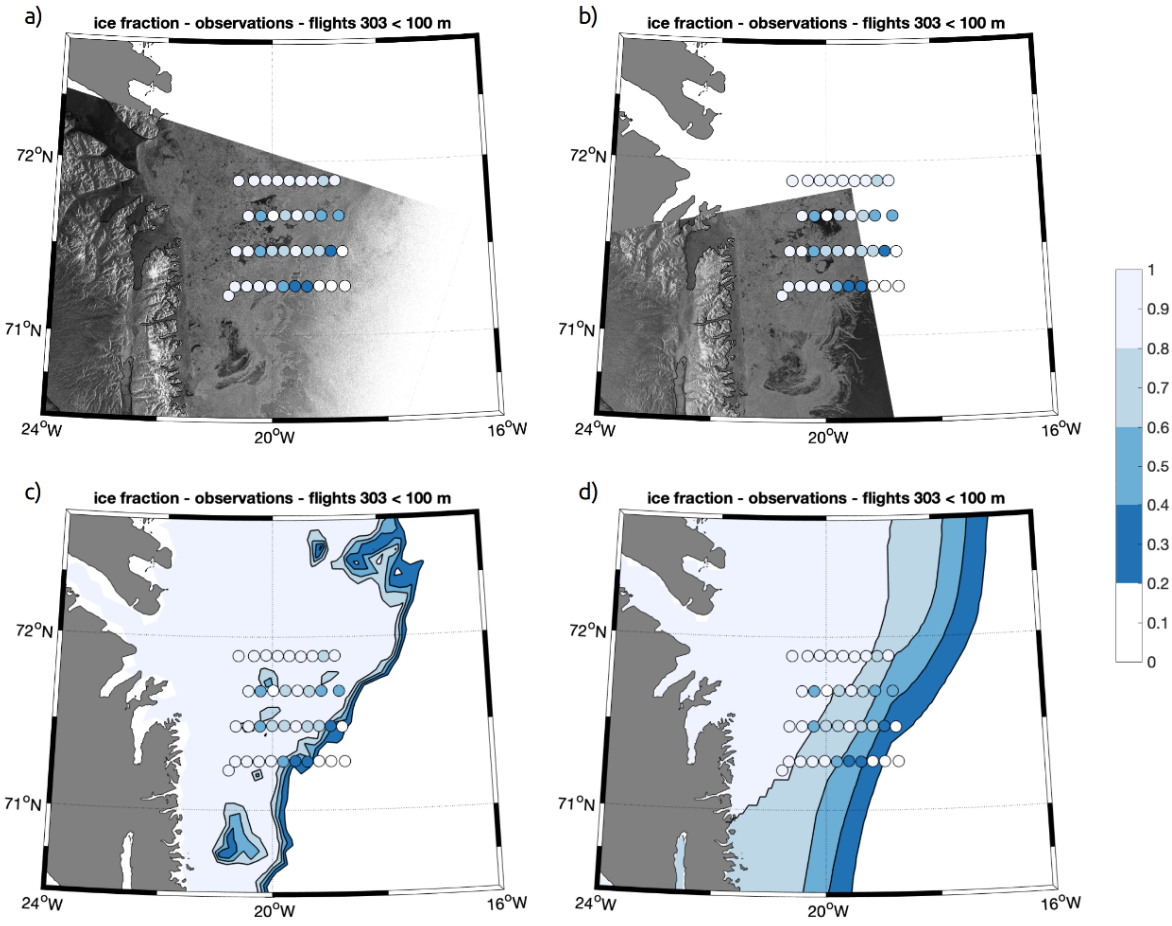

Figure 4.3 Sea ice fraction observations from flight 303 of the IGP aircraft campaign (shaded dots), with science legs taking place between 13:30 and 15:30 on 14/3/2018, overlaid on SAR satellite images from the same day at a) 08:20 and b) 18:51, and the day's sea ice analyses from c) AMSR2 and d) OSTIA. The SAR images show backscatter with high to low as light to dark, hence open water is darkest.

Figure 4.3 demonstrates the characteristics of AMSR2 and OSTIA under discussion. Displayed are two Synthetic-Aperture Radar (1 km resolution) satellite images of the study region with sea ice concentration measurements from IGP Flight 303 on 14 March 2018. Taking into consideration that the two images are taken roughly five hours before and three hours after the science legs of the flight respectively, the aircraft measurements accurately match with the SAR

imagery confirming their veracity. A clear visual agreement with both the observations and SAR image is displayed by the AMSR2 analysis for that day, in particular the ice edge gradient and its representation of polynyas. In contrast the OSTIA analysis provides a much poorer representation of the MIZ. The gradient of the ice edge is far too smooth, resulting in very little agreement with observations. Many of the other IGP science flights reinforce this result, as detailed by Renfrew et al. (2021). The ASI Bootstrap algorithm used to produce AMSR2, with a 5% ice concentration cut off, gives a sharper ice edge that is shown here to match observations far better than the smooth OSTIA field. However, the slightly smaller bias demonstrated by OSTIA suggests that the OSI-SAF hybrid Bootstrap/Bristol algorithm could be superior if the ice edge was better resolved. The Bootstrap algorithm has been previously shown to give higher ice concentration estimates compared to the NASA Team algorithm, particularly where surface snow or ice temperatures are relatively warm or new and young ice types are present (Comiso et al., 1997). Like the Bristol algorithm, the NASA Team algorithm utilises an extra brightness temperature channel, this time using the horizontal plane of the 19 GHz channel, in all using T_{19v}, T_{19h} and T_{37v}.Further evaluation of these two products with a larger number of observations over pack ice as well as the MIZ would be needed to confirm these findings Yet, as Comiso et al. (1997) do, by assessing the strengths and weakness of each technique for the purpose of the study in question, we can judge that AMSR2 is a better measure of the position of the sea ice edge and hence MIZ extent to verify the GC3.1 short-term model output.

4.3.2 Qualitative model analysis

Sea ice distribution

We start with a qualitative analysis of the simulated sea-ice distributions and a comparison to the sea-ice satellite products. In the AMSR2 satellite data from the 22 February 2018 (Figure 4.4) the sea ice edge is wavy with wind and ocean-eddy driven features, due to a combination of the eddy activity driven by the East Greenland Current flowing from the north and the wind from the south (see Johannessen et al., 1987). This coastward wind has also compressed the sea ice field resulting in a well-defined sea ice edge. This sharp gradient in sea ice concentration is not, however, visible in the OSTIA sea ice field.

The ORCA12 model at T+132 hours qualitatively replicates the sharp gradient of the sea ice edge reasonably well and has eddy driven features similar to those seen by AMSR2. The ORCA025 model is visibly similar to its higher resolution counterpart but displays smoother sea ice concentration gradients and less eddy-driven features.

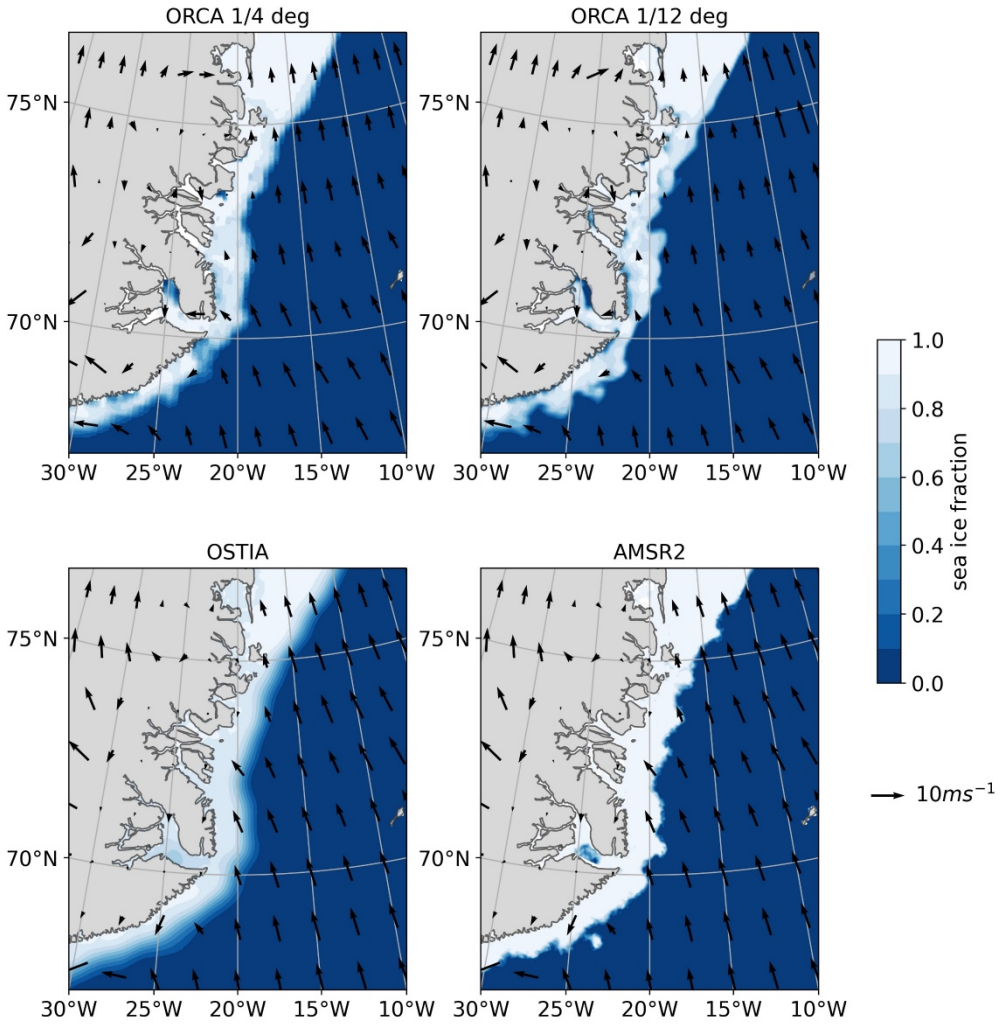

Figure 4.4 Sea ice concentration at 12 UTC 22/02/2018 the Iceland and southern Greenland Seas region. Panels show: a) and b) sea ice predicted by the coupled model with ocean grid resolution of 1/4° and 1/12° at T+132 hours respectively; c) and d) from OSTIA and AMSR2 satellite products from the forecast day respectively. Black arrows show 10 m wind vectors averaged over the duration of the forecast from each model in a) and b), and from ERA5 in c) and d).

This is to be expected with the coarser ocean resolution. Despite the common misplacement of eddy-driven features along the ice edge, the qualitative improvement that ORCA12 displays compared to ORCA025 should be commended, bearing in mind that inherent chaos in the system prohibits a perfect simulation. Yet, the problem of the sea ice distribution appearing morphologically correct and representative of the truth, but misplaced spatially, is a motive for further quantification of error using the IIEE metric and its components. For example, here the sea ice extent is roughly accurate, except for the displacement of eddy-driven mesoscale features, so that the regions of over- and underestimation will largely cancel each other to give a low absolute extent error, but the large symmetric differences in the model and verification sea ice fields will lead to a large misplacement error.

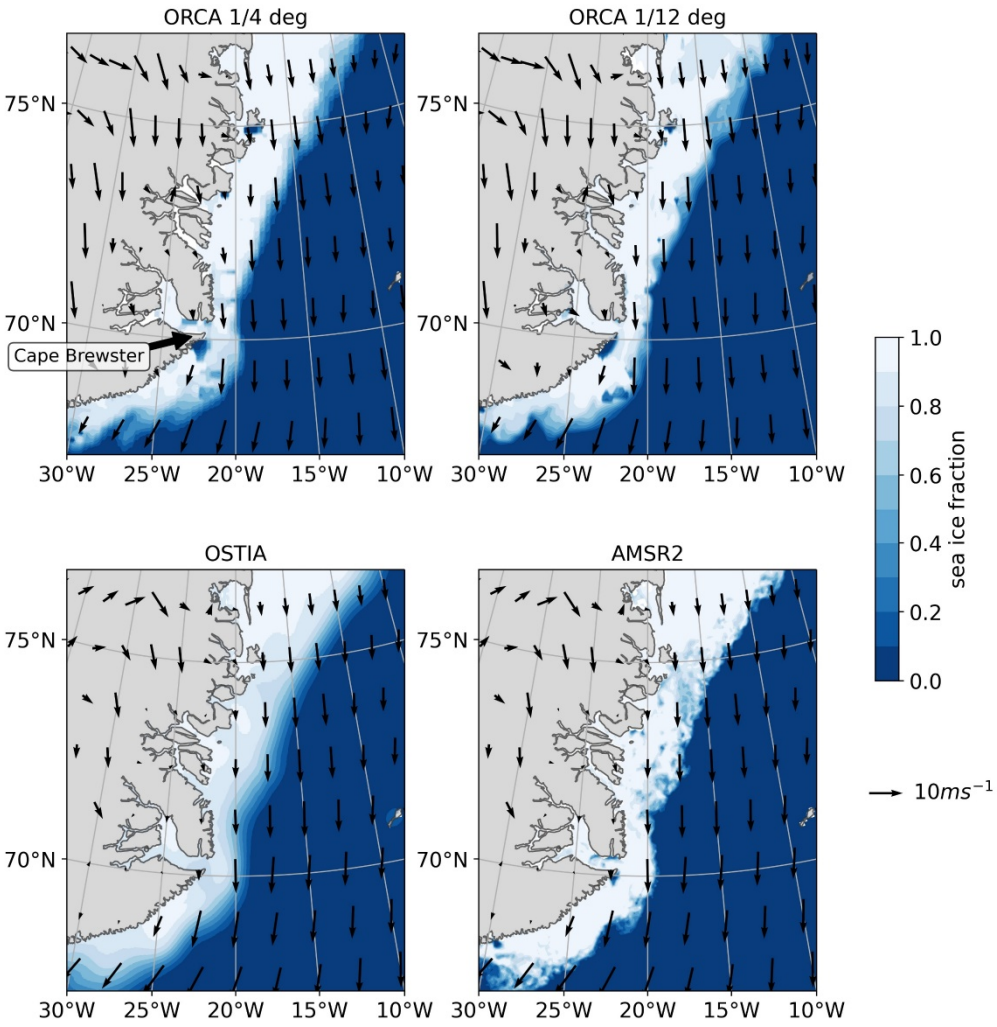

Figure 4.5 As Figure 4.4 for 12 UTC 06/03/2018 (forecast fields at T+132 hours).

On 6 March 2018 (at T+132 hours; Figure 4.5) the MIZ width has increased and is more diffuse due to the off-ice wind flow. The forecast sea ice fields also reproduce this divergence in the sea ice field, however, the ORCA12 version appears to display too much eddy activity with an undulating ice edge not seen in the verification products. In contrast, in this case the ORCA025 ice edge looks more representative of AMSR2, highlighting the problems caused by the 'grey zone' in eddy activity between these two ocean resolutions. Additionally, a small polynya can be spotted off Cape Brewster in the AMSR2 image (but not in OSTIA), which is successfully produced in both forecasts, though overestimated in spatial size suggesting that the atmospheric drag on the sea ice may be too strong.

Further evidence of potentially incorrect momentum exchange is given by the occurrence of this polynya on the 6 April 2018 (Figure 4.6), compared with the lack of any opening in the sea ice in AMSR2.

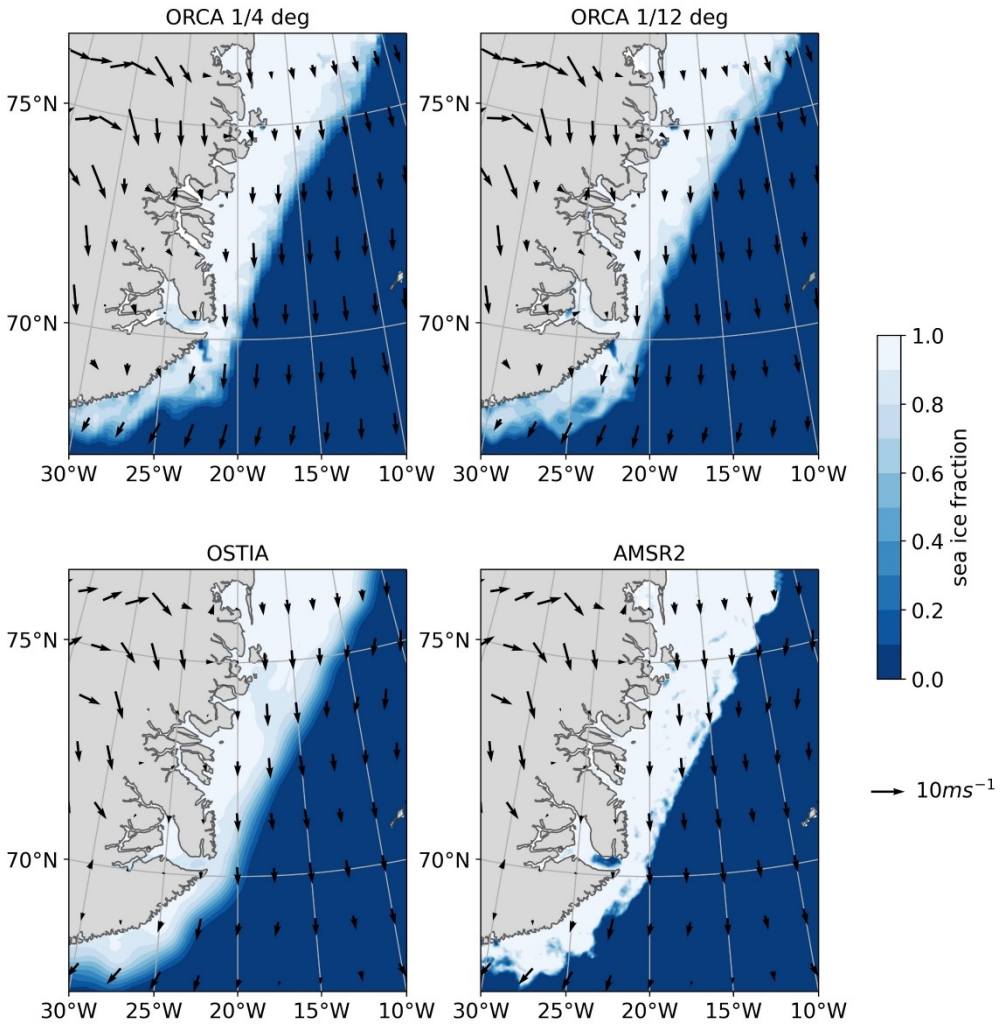

Figure 4.6 As Figure 4.4 for 12 UTC 06/04/2018 (forecast fields at T+132 hours).

Also at this time, the largest visual difference between these two forecasts and AMSR2 occurs south of Cape Brewster suggesting that this area is particularly difficult for the models to simulate for both the atmosphere and ocean fields. This can be attributed to the respective model resolutions not permitting accurate representation of the wind flow around the complex orography of the peninsula (c.f. Renfrew et al., 2008; Moore et al., 2016) and, likewise, the high dependency of the East Greenland Current on the bathymetry just offshore (c.f. Sutherland & Pickart, 2008; Håvik et al., 2017).

Wind fields

The 17 February 2018 forecast is dominated by a WAI regime, with persistent southerly winds bringing warm and moist air into the region from the Atlantic. This weather pattern was dominant for most of February (Renfrew et al., 2019). In contrast, the CAO forecast periods were dominated by northerly flow as shown by the 10-day mean wind in Figures 4.5 and 4.6. The 1

March 2018 case features stronger and more persistent northerly wind. The development of a barrier flow with local wind enhancement in the north Denmark Strait under these conditions is commonly found (Moore and Renfrew, 2005).

Having the same atmosphere configuration, the models displayed have mostly similar wind fields. There are some minor differences in wind speed over the sea ice, but it is unclear whether this is due to the representation of the sea ice at different ocean resolutions, or due to the model simulations naturally diverging due to intrinsic chaos.

4.3.3 Total IIEE Overview

In this section we evaluate the sea-ice distributions quantitatively using the IIEE metric. A summary of IIEE scores for all experiments using the typical sea ice concentration threshold of 15% (e.g., Goessling et al., 2016) is displayed in Figure 4.7. The average IIEE across all time steps for each experimental forecast was taken in an effort to reduce noise. Looking across the three forecasts, no one model configuration performs consistently better. Focusing on the AMSR2 (pink) verifications, the dynamic sea ice improves forecast skill for the 17 February and 1 March forecasts, but not the 1 April forecast when the persistent field displays the lowest overall error. Focussing on the OSTIA (green) verifications, the dynamic sea ice is only better than persistent sea ice for the 1 March case.

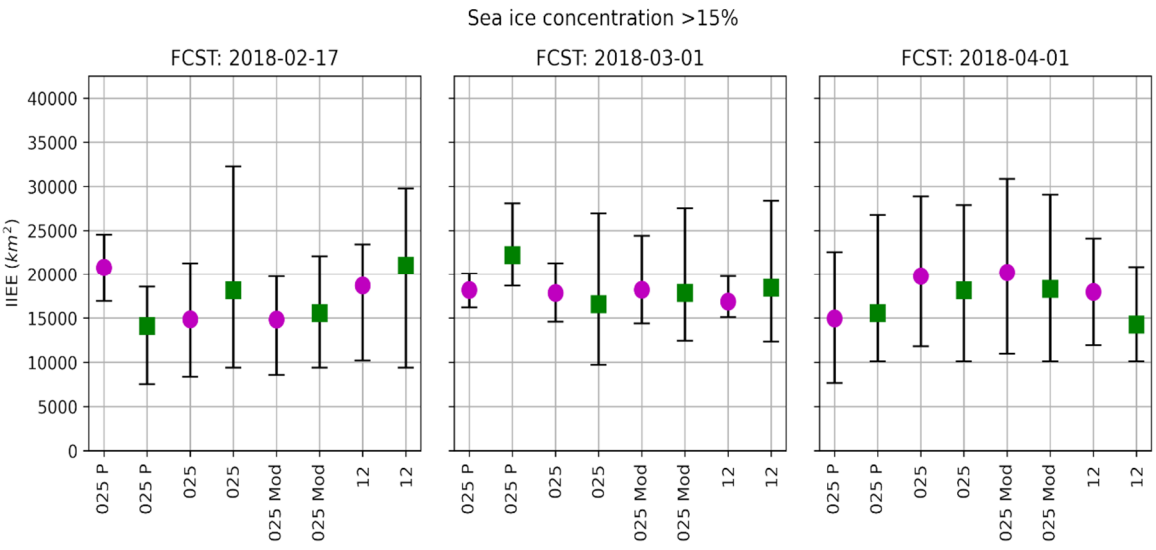

Figure 4.7 Overall mean IIEE scores, using a minimum sea ice concentration threshold of 15%, averaged over the duration of each forecast for all experiments. Error bars represent the range of errors across forecast time steps. Model configurations are indicated as: P for persistent sea ice; 025 for ORCA025; 025_mod for ORCA025 with modified atmospheric drag; and 12 is ORCA12. AMSR2 verifications are in pink, OSTIA in green.

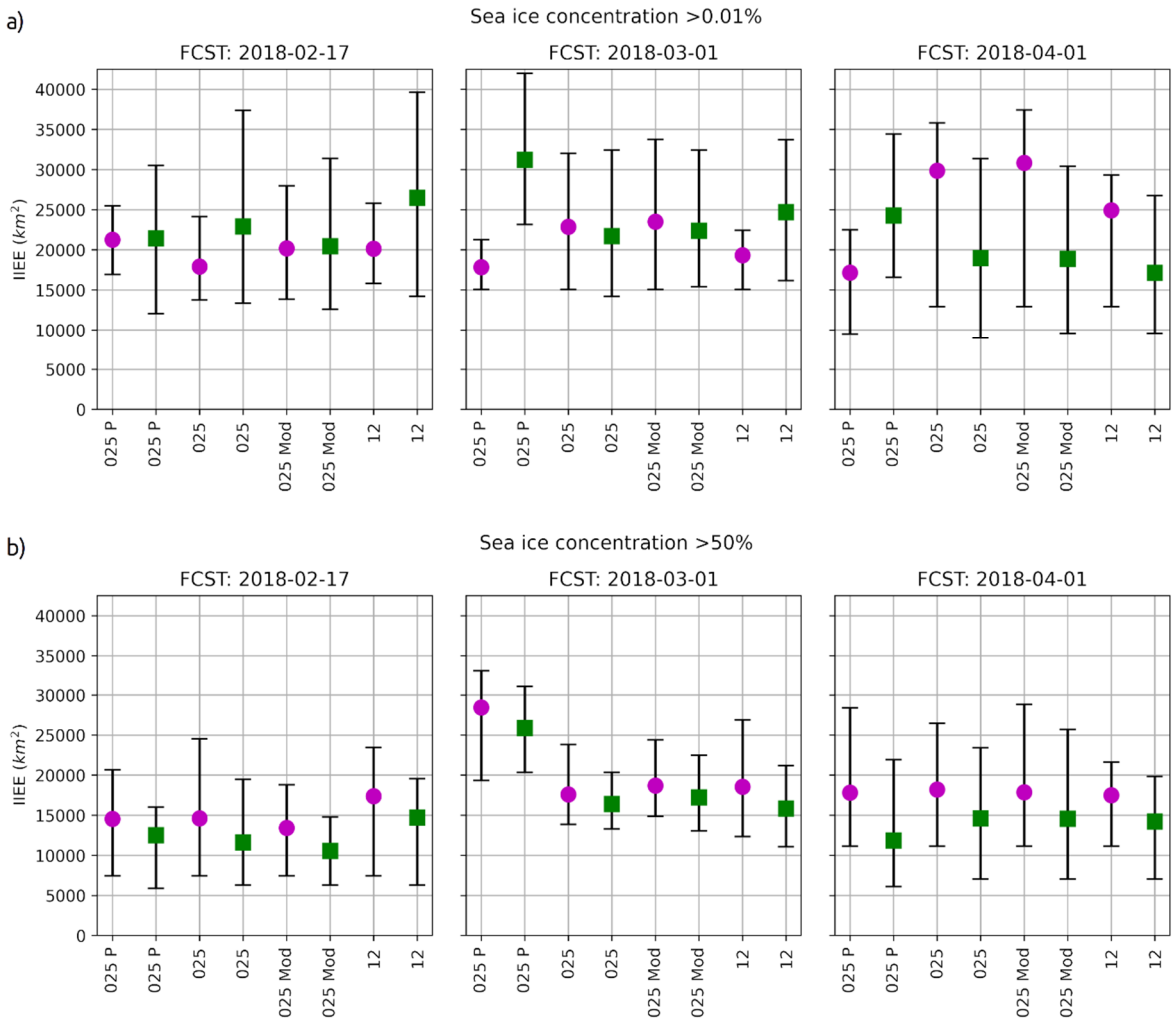

Figure 4.8 As for Figure 4.7 but for the analyses using minimum sea ice concentration thresholds of a) 0.01% and b) 50%.

The ORCA025 model and its counterpart with the modified drag scheme display remarkably similar overall error results, indicating that the difference between the schemes tested here is less significant than that of varying ocean resolution. That said, the ORCA12 simulations remain rather similar to the lower resolution ocean experiments, performing slightly worse in the 17 February forecast, almost the same in the 1 March forecast, and slightly better in the 1 April forecast.

Using a sea-ice concentration threshold of 0.01% provides further insight into the outer region of the MIZ (Figure 4.8a). When including the very low concentration sea ice in the analysis the IIEE is higher. This is likely due to these forecasts being initialised with the OSI-SAF 401 product, which contains too much low concentration sea ice. Verifying with AMSR2 finds that dynamic sea ice marginally improves upon persistent sea ice in the WAI case (17 February). However, under persistent CAO conditions from 1 March, the dynamic sea ice configurations perform

slightly worse than the persistent field. Yet more so, the 1 April forecast that features a mix of northerly CAO conditions and southerly winds shows the coupled models to perform substantially worse. These results are generally an amplified reflection of those at the 15% sea ice concentration threshold for AMSR2.

Despite similar results for the 17 February and 1 March cases when verifying against OSTIA at the 0.01% and 15% thresholds, for the 1 April case at the 0.01% threshold there is much greater difference between AMSR2 and OSTIA verifications, with an almost inverse judgement of which models perform best. This finding should be noted as a warning: despite the seemingly appropriate comparison of a forecast and a verification product that both originate from the same satellite product (OSI-SAF 401), the resulting measurement of sea ice extent error can give a misleading understanding of model performance.

Only considering sea ice above the 50% concentration threshold (Figure 4.8b) also reveals another difference between the two verification products. Using OSTIA for verification gives consistently lower estimates of error than AMSR2. In this part of the MIZ the ice is more 'solid' and spatially isotropic, so AMSR2's greater ability to resolve sharp gradients and small-scale features becomes less beneficial over OSTIA. Instead, we believe that this systematic difference is at least in part due to AMSR2's retrieval algorithm typically giving higher concentration values over the inner MIZ compared to OSTIA (Figure 3.2). As outlined in Section 3.1, OSTIA displays a lower overall ice fraction bias versus in-situ aircraft observations of around –0.04, compared to around +0.06 for AMSR2. Nonetheless, the differences between AMSR2 and OSTIA verifications are less than that shown between the forecast periods, suggesting that the synoptic conditions seem to be this most important factor when evaluating forecasts for the inner MIZ.

4.3.4 Spatial evolution of IIEE components

As stated by Equation 1., the IIEE error is found for each forecast time step by summing the areas of overestimation (O) and underestimation (U), and these components are illustrated here by red and blue regions, respectively. Remember that the sea ice product used to initialise the model lags the verification product by 24 hours, leading to differences between the simulations and OSTIA product even when evaluated at T+0 hours. This instantly highlights that compared to AMSR2 the models tend to overestimate the MIZ extent, while compared to OSTIA the models tend to underestimate, particularly during the CAO cases. This pattern is obvious from day 1 of each forecast, demonstrating that initial sea ice error pattern is often a governing influence on how error develops over time during these short-term forecasts.

Figures 4.9a and 4.9b illustrate the development of ice edge error between T+1 day and T+10 days for the 17 February forecast using AMSR2 and OSTIA for verification respectively. Although the region analysed is relatively small, these charts demonstrate the strengths of taking a magnified approach, as many details are noticeable that are not visible when viewing a similar Arctic wide analysis. This level of detail is necessary to gain an understanding of the sources of error over short-range forecasts.

Under the WAI conditions, the initial overestimation in the models becomes largely an underestimation by day 10 compared to AMSR2 (Figure 4.9a). The important factor in this case is that ocean current and the wind affecting the sea ice are acting in near opposite directions. This suggests that either the wind is pushing the model ice too far towards the coast, or the simulated EGC is not transporting enough ice southwards. The reduced wind drag experiment offers some insight, and in fact this case shows the largest difference between the two versions of the 1/4° models. Below 70° N the lower drag version displays a wider MIZ, suggesting that the higher drag in the original version is partly to blame for the ice being too compressed towards the coast.

However, the 1/12° version shows the lowest error in the same region with the same higher wind drag scheme, presumably due to increased transport by the better resolved ocean. This case demonstrates the interplay between the ocean and the wind forcing on the sea ice, and that the balance between the two must be fine-tuned when changing the ocean resolution.

In contrast, verification with OSTIA suggests that the WAI case is almost ubiquitously dominated by underestimation in the models (Figure 4.9b). Here the initial forecast field almost matches OSTIA, illustrating their shared connection to the OSI-SAF 401 product. Any difference is explained by the fact the model uses a 24-hour older analysis, and the processing that occurs between the OSI-SAF product and OSTIA or GC3.1 output. Nonetheless, using OSTIA to verify incorrectly suggests that the models are all performing poorly and in a similar manner, unlike the more nuanced AMSR2 evaluation of this case.

MIZ extent errors in the two CAO cases are relatively similar in their spatial development. AMSR2 determines that both feature an overly wide MIZ on initialisation and that this error generally persists throughout the forecasts (Figures 4.10a and 4.11a). The 1/12° ocean model version performs better than its 1/4° peers in both of these cases (recall the wind and ocean are flowing in a similar direction).

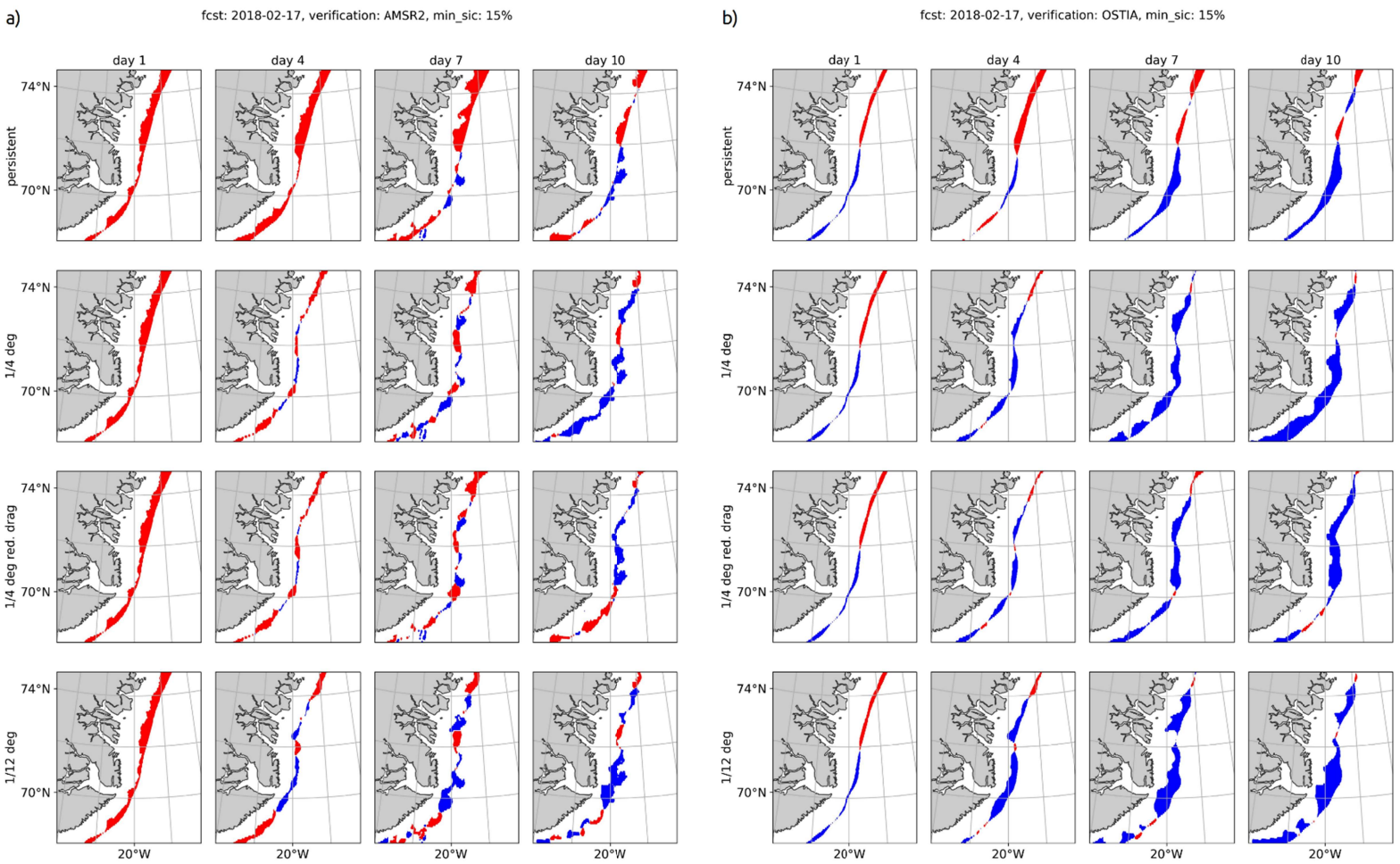

Figure 4.9 Spatial IIEE development during the 17/02/2018 forecast period using a) AMSR2 and b) OSTIA for verification. Red areas show where a model has overestimated the MIZ extent, while blue areas show underestimation.

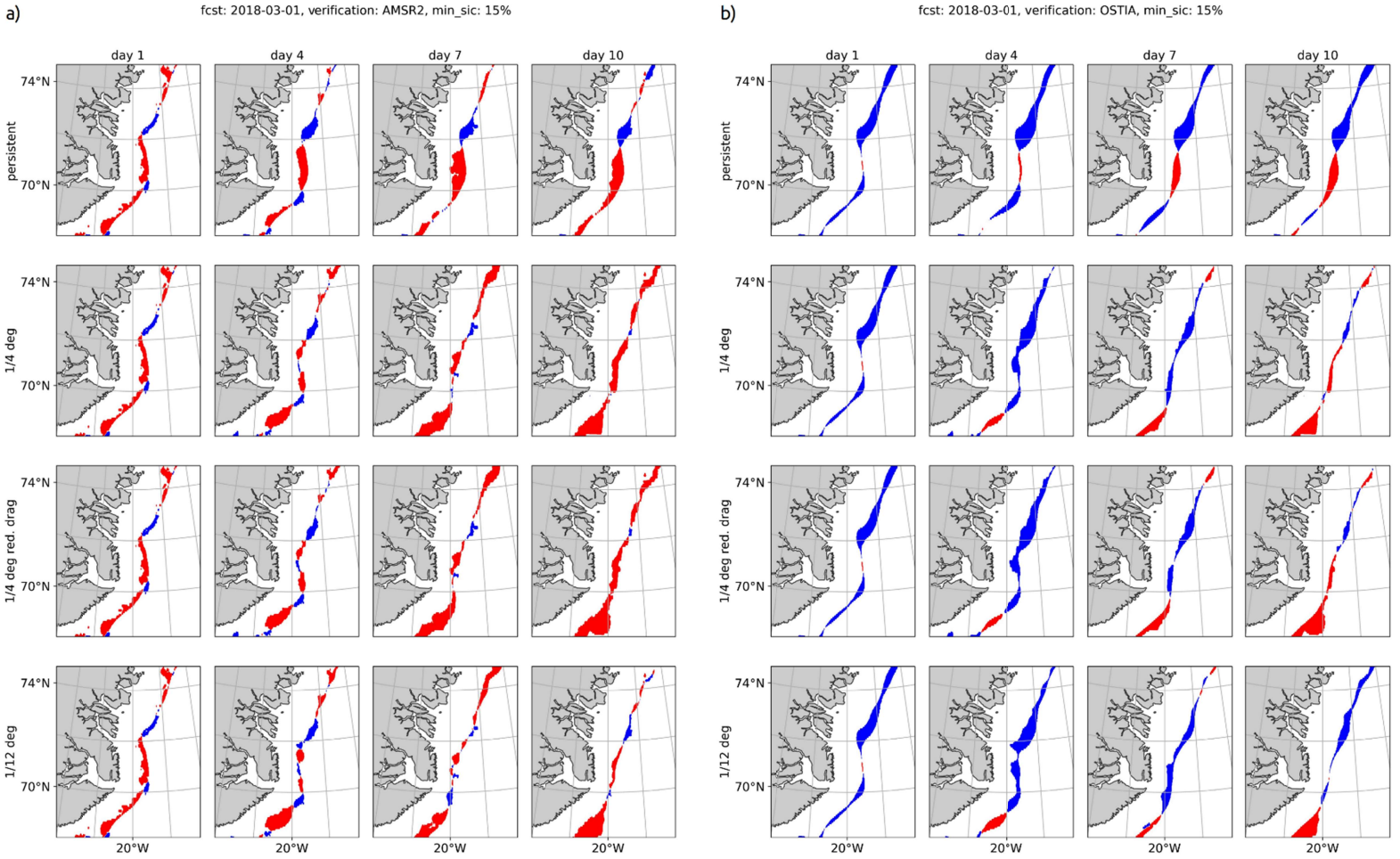

Figure 4.10 Spatial IIEE development during the 01/03/2018 forecast period using a) AMSR2 and b) OSTIA for verification. Red areas show where a model has overestimated the MIZ extent, while blue areas show underestimation.

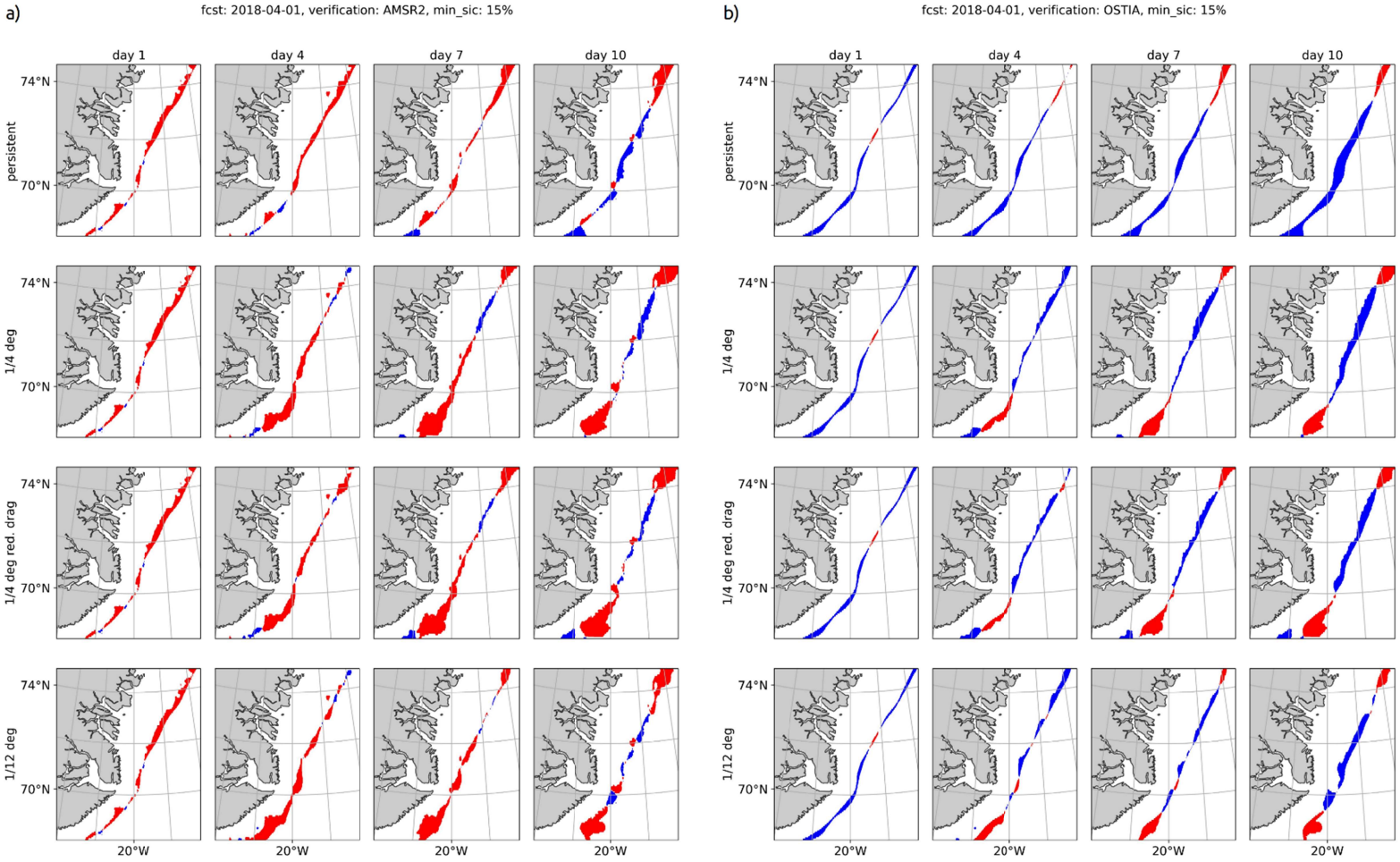

Figure 4.11 Spatial IIEE development during the 01/04/2018 forecast period using a) AMSR2 and b) OSTIA for verification. Red areas show where a model has overestimated the MIZ extent, while blue areas show underestimation.

Further, the different surface drag schemes applied to the 1/4° ocean have negligible influence on the error amount or distribution in both cases, despite the winds being significantly stronger during the March CAO. From this we deduce that the higher resolution ocean offers the best potential for improvement in short-term sea ice forecasting in this region. As illustrated during the WAI case, OSTIA determines an underestimation of MIZ extent to be the dominant error during these two forecast periods (Figures 4.10b and 4.11b).

An important feature develops in all the model versions in both CAOs that both OSTIA and AMSR2 agree on, suggesting it is consistent and remarkable, which is a build-up in sea ice that occurs at near the southern boundary of the domain, south of Cape Brewster at the entrance to the Denmark Strait. There are several plausible factors involved. There is a significant surplus of sea ice on initialisation that is transported southward. The point at which the sea ice patch develops is concurrent with the point at which the EGC commonly bifurcates. While the main portion of the EGC continues off the shelf break, a significant portion of the current typically splits towards the coast over the shelf, named the East Greenland Coastal Current (EGCC; Sutherland & Pickart, 2008). This delicate small-scale process is difficult for the ocean models to accurately capture and may result in incorrect dynamic forcing on the sea ice from the ocean. Bacon et al. (2014) suggest that an ocean model with 1/12° grid resolution is sufficient to resolve the EGCC, yet confidence in model simulations is low due to sparse observations (Håvik et al., 2017). Nonetheless, looking carefully at Figures 4.10a and 4.11a shows that the ORCA12 simulations produce a smaller patch of excess ice than ORCA025. With the same atmospheric dynamical configurations in all the models, the ubiquitous nature of the problem hints that atmospheric forcing on the sea ice is also an issue. Under barrier flow conditions due to convergence against Greenland's orography – typical of northerly flow regimes in this region (Moore and Renfrew, 2005) – enhanced low level wind is commonly observed south of Cape Brewster (Harden & Renfrew, 2012). Despite the atmospheric model being relatively high resolution in this region (10 km), such small-scale wind features can be misrepresented spatially or in magnitude. A further issue that arises from the complexity of the ocean dynamics and wind driven mixing in this area is the resulting high variability in sea surface temperatures. This thermodynamic issue could cause the sea ice to not melt sufficiently in the models due to a cold bias.

4.3.5 IIEE component timeseries

Figure 4.12 displays timeseries of the over- and underestimation contributions to the IIEE for each experiment during the three forecast periods. The amount of error tends to increase with time for each forecast, but the breakdown significantly differs between the AMSR2 and OSTIA

verifications. Compared to AMSR2, the CAO forecasts generally overestimate the MIZ extent when using the minimum sea ice concentration threshold of 15%. During the 17 February forecast, after being initialised with a significantly greater MIZ extent than observed by AMSR2, the similar over- and underestimations signify a misplacement of the sea ice. However, for the same case, comparing to OSTIA would suggest that the models substantially under predicted the amount of sea ice. Comparing to OSTIA, although the models are initialised from a similar analysis product just 24 hours earlier, the CAO forecasts are judged to universally under predict the MIZ extent early in the forecast periods. The differences between the parallel verification analyses exemplify the issue that using OSTIA analysis to verify sea ice forecasts may give false representation of model performance and poor understanding of the sources of error.

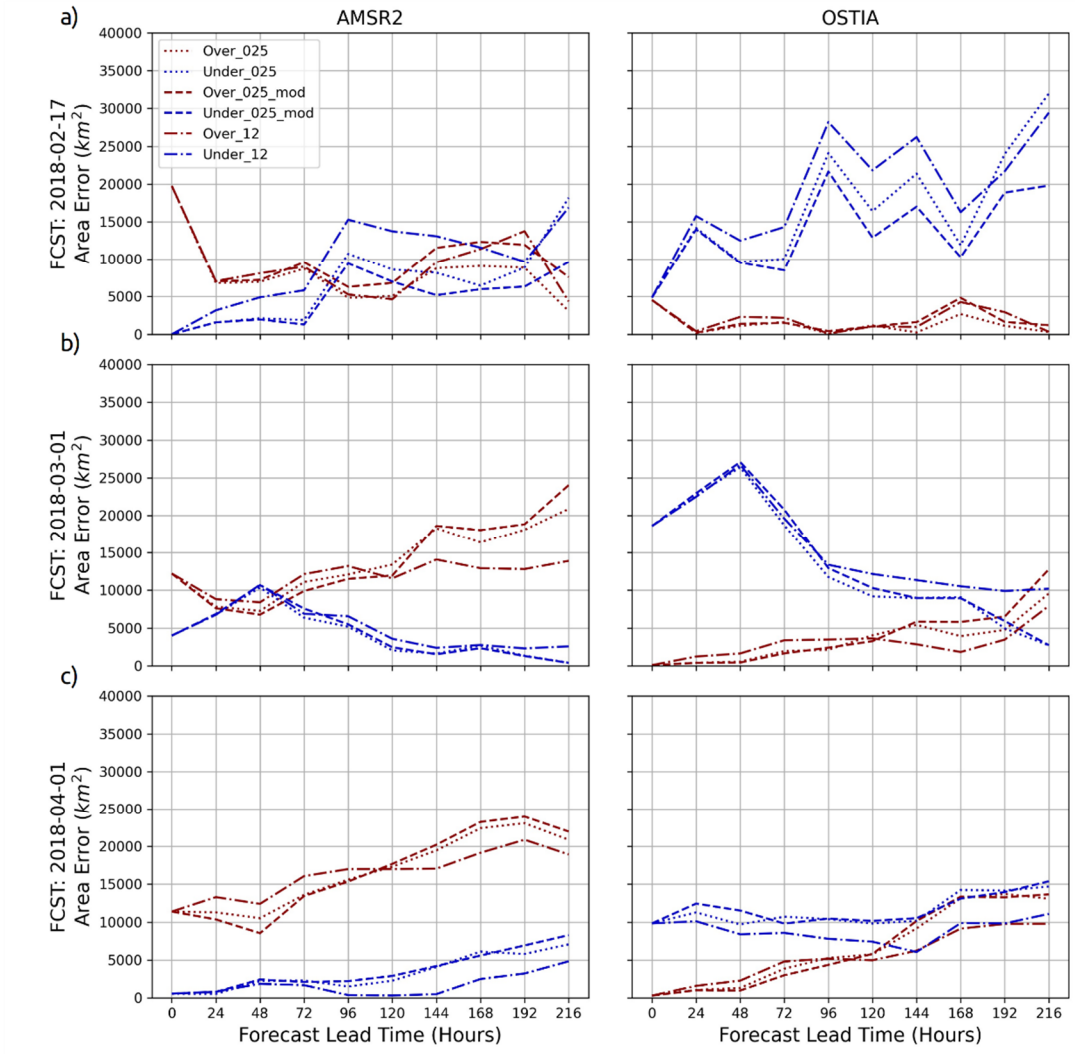

Figure 4.12 Time series of over- and underestimation for 3 forecasts using a sea ice threshold of 15%.

In addition, when looking at sea ice above 50% concentration (not shown), the IIEE error is lower and predominantly due to a misplacement rather than absolute extent error. This is to be expected as the more coastward mostly sea ice covered region is inherently more predictable. Also noteworthy is that the CAO forecasts begin with a significant underestimation of the MIZ extent, with both verification products in agreement. This discrepancy may be partly attributed to the relatively rapid divergence of the sea ice underway in these cases, associated with the off-ice wind flow, and the time delay between the forecast time step and the satellite analysis.

Given the similarity of the over- and underestimation time series between the experiments, their IIEE components were averaged over each forecast, for each verification product and sea ice concentration threshold. Then, using Equations 5 and 6, the over and underestimation time series can be converted into absolute extent error and misplacement error (AEE; ME; Figure 4.13). Using the 0.01% threshold the three forecasts are typically dominated by AEE on initialisation, and this error then persists during the forecasts. This finding reflects earlier discussion on the large amount of initialisation error due to the existence of too much low concentration sea ice However, due to the model sea ice field evolving under wind and ocean stress, a significant contribution of ME tends to grow.

When only considering the sea ice above 50% concentration, the two components are more equal on initialisation in the OSI-SAF 401 product. The initial error using the 15% threshold is also primarily AEE. But at T+72 hours the ME grows substantially larger than AEE for all forecast periods, and surpasses the ME found using the two lower thresholds. These findings are in line with those of Goessling et al. (2016), who show that ME typically dominates pan-Arctic IIEE, particularly at short lead times.

What can we learn from this breakdown into AEE and ME? First, a significant amount of extent error on initialisation will tend to persist throughout the forecast. Starting the models with an incorrect sea ice edge position, particularly when the amount of low concentration sea ice is incorrect due to blurring of the ice edge, will cause a persistent error. This will affect the spatial distribution of local maxima in surface fluxes and the boundary layer development.

Second, ME tends to grow across the entire MIZ in all model experiments. This highlights that there is room for improvement in the sea ice dynamics, with a combination of wind and ocean forcing errors responsible. Pulling these apart is difficult without considering further model diagnostics, but some suggestions can be made. Figure 4.12 shows that, during the CAO cases, the overestimation of MIZ extent on initialisation, dominates throughout the forecasts and grows by day 10. During these cases the wind and ocean forcing on the sea ice are acting largely

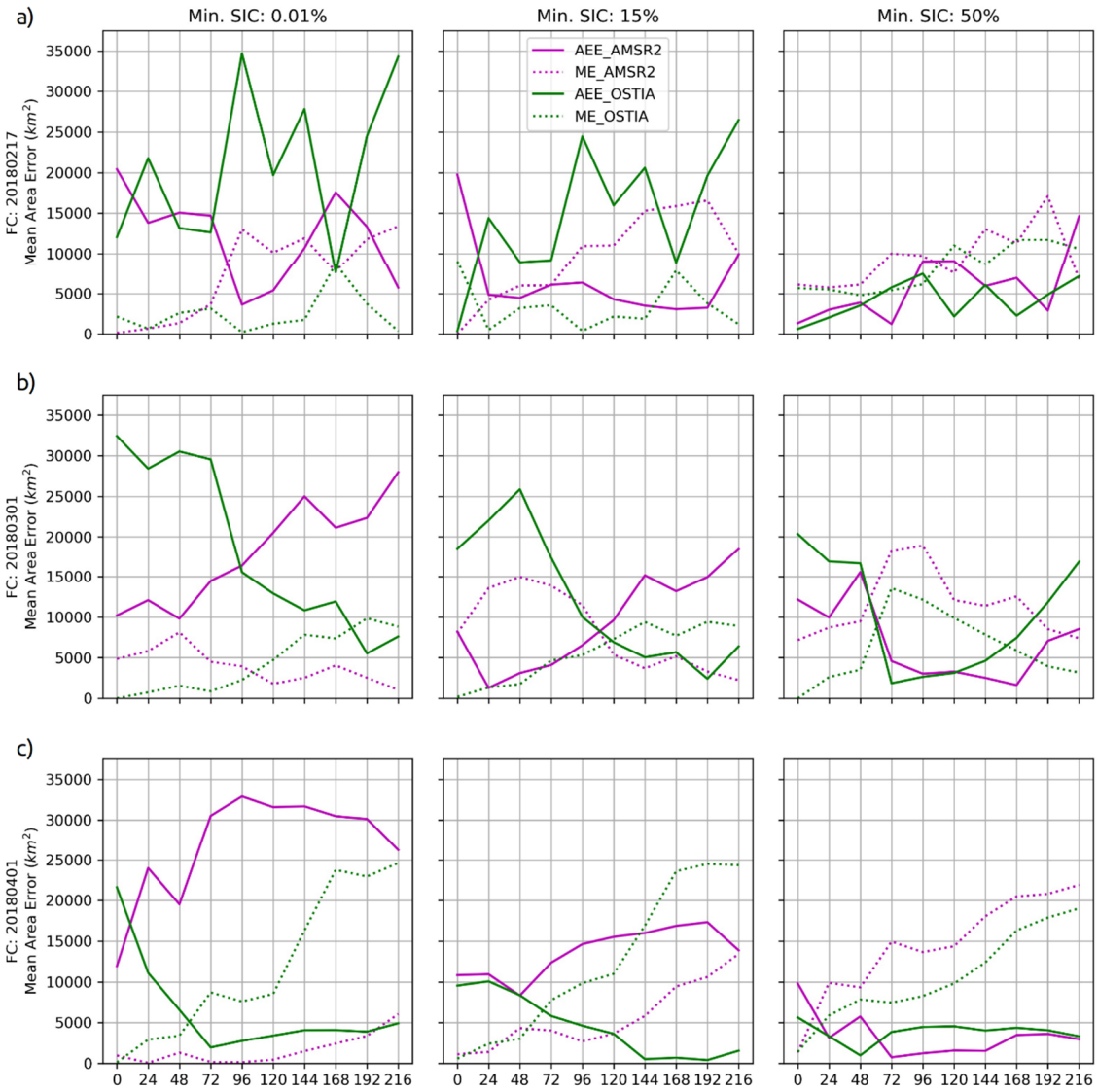

Figure 4.13 Development of Absolute Extent Error (AEE) and Misplacement Error (ME) averaged over the three experiments for each forecast, using sea ice concentration thresholds of >0%, 15% and 50%.

in the same direction and the 1/12° ocean version performs better. Thus, imperfect parameterisation scheme for sub-grid scale ocean dynamics, i.e., ocean eddies, in the 1/4° ocean model may not be dissipating enough energy resulting in overly high current velocity.

4.4 Discussion

The choice of sea ice product for verification is critical

The OSTIA sea-ice concentration product is shown to be poorer in spatial distribution than AMSR2 compared to in-situ aircraft observations and SAR images. The Gaussian smoothing applied to each grid cell in the OSI-SAF 401 product, which OSTIA is based on, results in a lack of

sharp gradients at the ice edge. The resultant excess of low concentration sea ice widens the OSTIA MIZ extent. AMSR2 provides a more accurate representation of the sea ice edge and extent due to its sharper gradients and cut-off of sea ice <5% concentration. However, AMSR2 does display a small positive bias, possibly due to its retrieval being solely based on the Bootstrap algorithm, in contrast to a smaller bias in OSTIA which uses the hybrid Bootstrap-Bristol algorithm. This suggests that hybrid retrieval method could be preferred. However, this finding points to the need for a more substantial investigation of MIZ representation in sea ice products.

It is also demonstrated that there is a significant repercussion from the choice of verification product. Using two separate sea ice analysis products for evaluation can lead to opposing results (i.e., a large under- or overestimation of MIZ extent). Hence, there is a high degree of sensitivity in this kind of analysis to the verification product selected. Despite the marginally better overall bias score for OSTIA, for the purposes of a local short-term forecast the better spatial reproduction of the sea ice field in AMSR2 is more suitable.

Initialisation problem

A key finding is that there is a significant error in the sea ice field used for initialisation. Consideration must be given to the delay between the forecast time (00Z) and the satellite product verification time (12Z). Though, due to technical limitations the satellite products are in fact a composite of many individual measurement swaths throughout the day, hence can only be considered accurate to around ± 12 hours. In addition, the forecast uses an already 12 hours old sea ice analysis.

Those caveats considered, the error on initialisation as assessed by AMSR2 and OSTIA are far from in agreement. Most strikingly, comparing the two evaluations of the full initial sea ice fields (>0.01 %) in Figure 4.12 illustrates that the findings are almost opposite; validating with AMSR2 finds the models to be overestimating sea ice extent, while validating with OSTIA finds them to be underestimating. This disagreement originates from the OSTIA product being overly smooth, failing to accurately represent a distinct ice edge and thus producing an extended band of low concentration sea ice. The findings here further evidence OSTIA's weaknesses for use in forecasting and verification.

The significant amount of sea ice extent initialisation error hampers the forecast skill, adding to research by Day et al. (2014) who found sea ice thickness initialisation error reduces forecast capability. By the end of each forecast the error amounts in the AMSR2 and OSTIA evaluations tend to converge as the effects of the initial sea ice fields diminish. This translates into a change

from AEE, introduced by the OSI-SAF 401 product, to ME as the erroneous areas of sea ice are transported by the ocean and wind model components.

Mobility of ice

The spatial evolution of sea ice in all the coupled model simulations suggests that sea ice transport is too strong. In the WAI case (Figure 4.9), with southerly wind, the sea ice is pushed too far towards the Greenland coast resulting in a general underestimation of sea ice extent. In the CAO cases (Figures 4.10 and 4.11), with northerly winds, the largest amount of error in each simulation tends to take the form of a patch of overestimation in the south of the domain shown. These findings suggest that excessive sea ice transport may be due to wind stress that is too strong. However, the surface drag experiments do not consistently agree with this suggestion, and it is difficult to discern the differences between ocean and wind effects within the scope of this analysis. Typically, the 1/4° ocean reduced wind drag experiment has slightly higher error than the 1/4° ocean version with higher wind drag, albeit with very small differences. The 1/12° ocean version tends to perform best, suggesting that its ability to resolve a greater range of ocean features is beneficial., But these results are not always consistent. Further analysis of the separate ocean and wind momentum flux on the sea ice components is needed to decide if this evaluation corroborates that surface roughness over the MIZ is set too high in GC3.1 and the updated surface drag scheme after Lupkes et al. (2012) and Elvidge et al. (2016) will be beneficial for GC4. Tuning of other parameterisation schemes, such as the ocean drag on sea ice, is likely needed. The significant growth in ME in all the cases analysed certainly proves that there is room for improvement in the dynamic sea ice schemes. We suggest that further work would include evaluation of the model values for oceanic and atmospheric drag against observations.

4.5 Conclusions

We have demonstrated the value of the IIEE metric for use at short-range local forecast scale, building on previous large scale long-term forecast studies. In particular, close analysis of the IIEE component terms illuminates complex underlying processes responsible for model error. By decomposing the IIEE metric here, we illustrate dramatic differences between using AMSR2 and OSTIA sea-ice forecast verification and that the choice of observational sea ice product is critical for short-range forecast evaluation. The overly smooth sea-ice distribution in the OSTIA product can result in an expanded MIZ extent. AMSR2 provides a better representation of the sea-ice edge and appears more suitable for the type of focussed analysis presented here. A more

comprehensive comparison study of satellite sea ice products, incorporating more observations over a greater spatial extent, would be needed to confirm this finding.

The lack of sharp gradients in the OSTIA sea ice product originate from the OSI-SAF 401 satellite product from which its data is sourced. We demonstrate that initialising coupled models using the OSI-SAF 401 product introduces significant error, particularly due to it containing too much low concentration sea ice. The amount of error in initial conditions in the experiments here is larger than the difference between the ORCA025, ORCA025 with reduced atmospheric drag, or the ORCA12 configurations. Nonetheless, the experiments displayed here show that there are improvements to be made in momentum exchange at the atmosphere-ice and ocean-ice boundaries for short-range sea-ice forecasting. The ability of ORCA12 to resolve a wide range of ocean features, such as eddy activity, suggests that using a higher resolution ocean model is worthwhile for sea ice prediction and coupled weather forecasting in the high latitudes.

5 Projected changes to wintertime air-sea turbulent heat fluxes over the subpolar North Atlantic

5.1 Introduction

Air-sea fluxes over the subpolar North Atlantic (SPNA) play a crucial role in atmosphere and ocean circulation. The largest portion of this energy and moisture transfer is due to sensible and latent heat fluxes that occur during cold-air outbreaks, which account for 60% to 80% of wintertime oceanic heat loss (Papritz & Spengler, 2017). These turbulent heat fluxes cool the surface waters and promote convective overturning, thus playing a crucial role in the Atlantic Meridional Overturning Circulation (AMOC) - a key component of the global climate system. The AMOC brings warm, salty water from the Gulf of Mexico northwards into the SPNA, which becomes colder and denser and sinks, to be exported southwards as North Atlantic Deep Water (Buckley & Marshall, 2016; Figure 1.1). The release of ocean heat into the atmosphere has a profound effect on the climate of northwest Europe, raising air temperatures by as much as 6°C compared to Pacific maritime climates at a similar latitude (Palter, 2015).

Aagaard & Carmack (1989) suggested that the Greenland and Iceland Seas were, at the time, 'delicately poised' in their ability to sustain convection. Since their publication, conditions in the Arctic and nearby subpolar regions have changed substantially. Most notably, a rapid decline of sea ice has been observed (Comiso et al., 2008; Figure 1.8), raising concern that in summertime the Arctic will be ice free (<1 million km^2) within a couple of decades (Overland & Wang, 2013). Parkinson & Cavalieri (2008) showed that while summer sea ice has declined in the Greenland, Iceland and Irminger Seas by 11.4% (+/- 4.3%), winter sea ice has also declined by 10.0% (+/- 2.5%) over 1976-2006. A more recent assessment found that annual mean Arctic sea ice area has reduced by around 20% over the period 1979-2014 (Sévellec et al., 2017). Moore et al. (2015) showed that wintertime sea ice retreat in the Iceland and Greenland Seas, along with different rates of warming for the ocean and the atmosphere, has resulted in reductions of around 20% in the magnitude of air-sea fluxes in these seas since 1979. They also demonstrate that further decreases in atmospheric forcing will likely reduce ventilation of mid-depth waters in the Greenland Sea and decrease the supply of the densest waters into the lowest limb of the AMOC. However, the retreating ice cover from the region's boundary currents is also responsible

for changes in the spatiotemporal variability of air-sea heat fluxes. Moore et al. (2022) find that a reorganisation of where water mass transformation occurs is underway, with increased turbulent heat fluxes observed over key boundary currents in the SPNA where retreating sea ice has exposed them to the atmosphere (e.g., Våge et al., 2018).

There is evidence to suggest that the AMOC has already slowed to some extent. The AMOC has been measured by the RAPID array at 26.5°N since 2004, and despite significant variability this data set shows a recent weakening in volumetric transport of approximately 15% compared to the period 2004-2008 (Smeed et al., 2018). Other studies have also found via proxies or models that a gradual slowdown of the AMOC appears underway (e.g., Rahmstorf et al., 2015; Caesar et al., 2018). Coupled climate models have suggested it is likely to continue declining in response to anthropogenic climate change over the 21st century (Fox-Kemper et al., 2021). Strikingly, the observed pattern of changing sea surface temperatures and air-sea fluxes in the North Atlantic is comparable to the response to a declining AMOC predicted by coupled climate models (Smeed et al., 2018). The possibility that the AMOC may suffer a catastrophic collapse in the not distant future is often referred to in popular culture. This is generally thought to not be an immediate concern, yet it cannot be ruled out (Weijer et al., 2019).

Recent modelling efforts enable further investigation into the future of the AMOC. In the state-of-the-art multi-model, multi-resolution ensemble, the Coupled Model Intercomparison Project Phase 6 (CMIP6) High Resolution Model Intercomparison Project (HighResMIP), the AMOC and northward heat transport to the SPNA tends to become stronger (and agree better with RAPID observations) as ocean model resolution is increased (Roberts et al., 2020; Chassignet et al., 2020). Roberts et al. (2020) suggest these differences in AMOC strength are mainly due to the different ocean model resolutions, as changes to the atmospheric resolution alone give generally smaller changes and are more model dependent. Further, these higher resolution ocean models (1/12° to 1/4°) predict larger declines in the AMOC than typical resolution climate models (1° to 2.5°), suggesting a potentially greater risk posed by climate change for the Northern Hemisphere. Higher resolution models also enable analysis of more complex smaller scale changes to air-sea interactions. For example, Wang et al., (2020) identified in high resolution ocean simulations a mechanism where sea ice retreat leads to intensified heat transport to the Arctic Ocean through Fram Strait, potentially contributing to the 'Atlantification' of the Arctic.

This study makes use of output from HadGEM3-GC3.1, one of the better performing CMIP6 members in terms of AMOC representation (Roberts et al., 2020; Hirschi et al., 2020; Heuzé,

2021) and Arctic sea-ice mass budget (Keen et al., 2021), to explore the future of air-sea turbulent fluxes in the SPNA. Note however, there is a large spread in sea-ice area and mass across the CMIP6 ensemble, both in historic and future simulations (Notz et al., 2020). We investigate output from several single CMIP6 members (MM and HH resolution), taking a storyline approach in order to compare several plausible and physically consistent simulations of the future (Shepherd et al., 2018).

We address several key questions:

- How well does the model simulate climatological sea ice and air-sea fluxes, and how does this vary with increasing ocean resolution from 1/4° to 1/12°?
- How are these fluxes projected to change over the course of the 21st century with retreating sea ice?
- What are the potential impacts for ocean convection and the formation of dense waters that feed into the AMOC?
- And how might this affect atmospheric circulation and the climate of northwest Europe?

First, we describe the model configuration in detail, the methods used to evaluate the simulations against climatological data, and the forcing used to drive the models into the future. Then we discuss the strengths and weaknesses of the historic simulations, before discussing the projected changes later this century. Last, we probe the implications of these changes for the SPNA and attempt to elucidate ramifications for the AMOC.

5.2 Data and Methods

5.2.1 ERA5

To provide a quasi-observational data set by which to evaluate the historic model runs we use the ECMWF Reanalysis version 5 (ERA5), accessed using the Copernicus Climate Data Store service. We use monthly averaged data to calculate extended winter (here defined as December to March) mean values, denoted henceforth by the year in which the winter started. At the time of writing, the data is available in two parts: 1979-present, which has significantly more satellite observations available (Hersbach et al., 2019); and the 1950-1978 preliminary back extension, which has greater uncertainty due to fewer available observations (Bell et al., 2020). ERA5 offers several advantages compared to its predecessor, ERA-I, which was used by Moore et al. (2012) to document the climatological air-sea fluxes over the SPNA. These include an improved model configuration (IFS Cycle 41r2), increased resolution (~30 km), and, not least, the extended record

back to 1950 that conveniently matches the available period for the HadGEM3-GC3.1 HighResMIP historical simulations. An evaluation of ERA5 against in-situ observations in the Iceland and Greenland Seas showed that it generally performs very well in the region, albeit with less accuracy over the marginal ice zone than over the open ocean (Renfrew et al., 2021).

5.2.2 HadGEM3-GC3.1

To investigate the future evolution of air-sea turbulent heat fluxes over the course of the 21st century we use output from the Hadley Centre Global Environment Model 3 – Global Coupled version 3.1 (HadGEM3-GC3.1) at medium-medium (MM; Roberts et al., 2017a) and high-high (HH; Roberts et al., 2017b) atmosphere-ocean resolutions of 60 km - 1/4° and 25 km - 1/12° respectively. This model output was configured for submission to the Coupled Model Intercomparison Project Phase 6 (CMIP6) (Eyring et al., 2016), and is described in detail by Williams et al. (2017) and Roberts et al. (2019). Model data was accessed from CEDA (www.ceda.ac.uk) using the JASMIN supercomputing service.

The atmospheric component has science configuration GA/GL7.1 (Walters et al., 2019), with 85 vertical levels to a height of 85 km and a rectilinear grid. The grid resolutions of the model atmosphere used are comparable to the 30 km grid spacing in ERA5. The ocean component, GO6 (Storkey et al., 2018), has 75 vertical levels and a curvilinear tripolar grid. At MM resolution the ocean can be described as eddy-permitting, while the HH is eddy-rich. The sea ice component, GSI8.1 (Ridley et al., 2018) is output on the same grid as the ocean. Data on the tripolar grid system, particularly at high resolution, poses a nontrivial challenge to utilise. Hence, all model output was transformed onto a regular latitude-longitude grid of resolution 0.25° by 0.25° to match that of ERA5. The Climate Data Operator (CDO) suite of tools was used to perform this task. This facilitated direct comparison of products on a grid cell by grid cell basis and statistical analyses.

The model simulations analysed are listed in Table 5.1. Verification of HadGEM3-GC3.1 output is performed through comparison of historic simulations (1950-2014 with observed historical climate forcing applied; see Andrews et al., 2020) against climatological values from ERA5. The higher resolution HH model is near the computational limit for long-range climate prediction, hence has received less evaluation and tuning at the time of writing. Thus, we also include the HH control run (1950-2050 with constant 1950 climate forcing; see Roberts et al., 2019) in our evaluation for further comparison. The future runs are forced using the standardised time varying CMIP6 forcings detailed in Eyring et al. (2016). The future projections incorporate forcing specified by alternative future societal development pathways (SSPs).

HadGEM3-GC3.1 Configuration	Atmosphere grid size	Ocean grid size	Run length (years)	Period
MM-historical	60 km	1/4°	64	1950-2013
HH-historical	25 km	1/12°	64	1950-2013
HH-control	25 km	1/12°	100	1950-2049 (nominal)
MM-SSP1-2.6	60 km	1/4°	85	2015-2099
MM-SSP5-8.5	60 km	1/4°	85	2015-2099
HH-future-(SSP5-8.5)	25 km	1/12°	35	2015-2049

Table 5.1 Overview of the HadGEM3-GC3.1 model simulations evaluated.

These narratives are described quantitively in terms of population growth (Samir & Lutz, 2014), economic growth (Dellink et al., 2015), and urbanisation (Jiang & O'Neill, 2015). In this study only two of the five pathways are analysed, SSP1-2.6 and SSP5-8.5. Qualitatively they can both be described as "optimistic trends in terms of human development", meaning that education and health is well funded, societal institutions function well and economic growth is rapid. However, SSP1-2.6 involves increasing deployment of sustainable technologies, while SSP5-8.5 assumes an intensively fossil fuel-based economy (O'Neill et al., 2015). The key factor in each scenario is their long-term global average radiative forcing levels of 2.6 Wm^{-2} and 8.5 Wm^{-2} respectively, as denoted in the acronyms. These two pathways represent the low and high ends of the suggested range of possible future scenarios. For the MM configuration both pathways are evaluated to 2100, but the HH future run is only available using SSP5-8.5 forcing and to 2050. As only one model integration, known as a realisation, is available for the HH future simulation, we primarily use the first realisation of the other model configurations, despite multiple realisations being available. To ensure the validity of this decision four realisations of the MM historical model were compared, finding little difference between them when considering climatological winter means (not shown).

5.2.3 Methodology

For the purpose of this study the SPNA is defined as the non-land area that lies between 70°W to 60°E, and 50°N to 85°N. The distribution of turbulent heat fluxes across the SPNA in different simulations can be illustrated with spatial charts. However, to gain a deeper understanding of the changes in important subregions we define seven study areas (similar to Papritz & Spengler, 2017) that are used in a quantitative assessment. These are the Iceland, Greenland, Irminger, Barents and Norwegian Seas, and Fram Strait west of Svalbard, see Figure 5.1.

To analyse sea ice conditions, we compute the average grid cell sea ice concentration as output by the model for each study region. This is not converted to sea ice area as we are most interested in the fraction of sea ice cover in each region, not the absolute area of sea ice. The

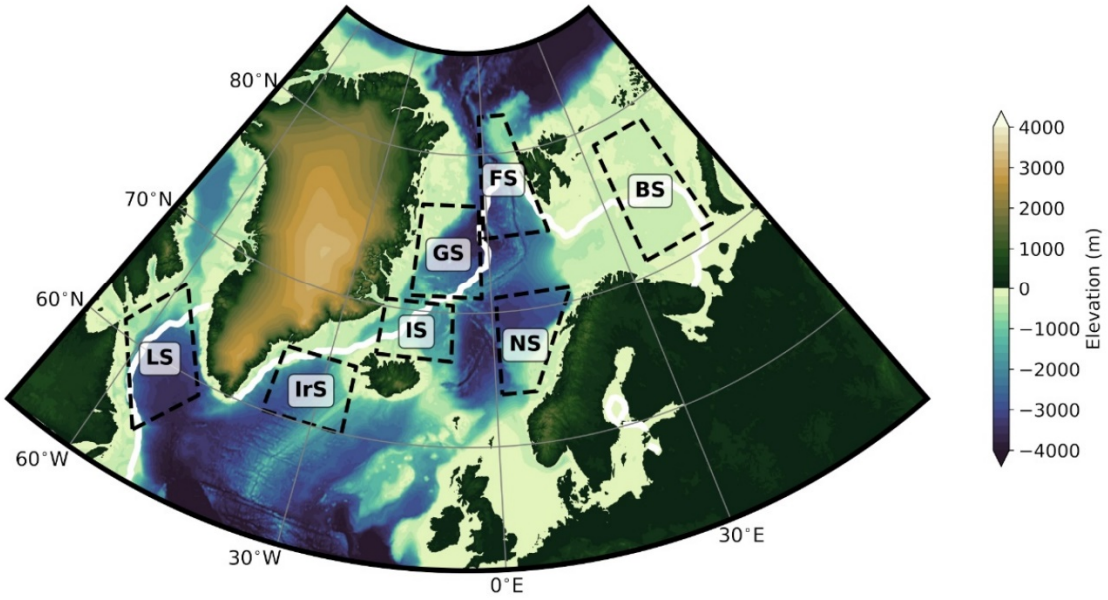

Figure 5.1 Map of the subpolar North Atlantic, with bathymetry and topography shaded. The study regions outlined by the black dashed lines are Labrador Sea (LS), Irminger Sea (IrS), Iceland Sea (IS), Greenland Sea (GS), Fram Strait (FS), Norwegian Sea (NS) and Barents Sea (BS). The thick white line represents the ERA5 winter mean (1950-2020) 15% sea ice concentration contour.

regions differ in total area, so this information is more useful to draw comparisons and to evaluate changes over time. Further insight into the performance of the historic simulations is provided by conditionally sampling the data sets based on the total wintertime sea ice area over the SPNA. Composites of 'low ice years' and 'high ice years' are created by selecting the years in each data set where the total sea ice extent is below the first quartile (<Q1) and above the third quartile (>Q3) respectively.

5.3 Evaluation of historic simulations

5.3.1 Spatial distribution of sea ice and turbulent heat fluxes

Figure 5.2 displays the spatial distribution of wintertime mean surface meteorological fields over the climatological period of 1950-2013 for ERA5, and the HadGEM3-GC3.1 HH and MM models (HH historical; MM historical). As ERA5 is very similar to its predecessor ERA-I, it follows that there is very close agreement in the spatial distribution of 2 m air temperature (T_a), mean sea level pressure (*MSLP*) and total turbulent heat flux (*THFX*) with previous climatologies (e.g., Moore et al., 2012, see Figure 1.5). The HH historical simulation shows generally good spatial agreement with ERA5, however it exhibits too much low concentration sea ice in the Iceland and Greenland Seas. This is due to the existence of years in the model when these regions were

largely covered by sea ice, hence the mean 25% sea ice concentration contour lays further east than seen in ERA5. Conversely, the ice edge is situated reasonably accurately in the Fram Strait and Barents Sea regions in the HH historical model, though the ice concentration is too low east of Svalbard. Mean sea level pressure in the HH historical run agrees very well with ERA5 in the position and depth of the Icelandic Low. The near-surface air temperature field also agrees very well with the ERA5 climatology. The spatial distribution of total turbulent heat flux corresponds reasonably well with ERA5. However, the magnitude of fluxes is incorrect in places with fluxes too high near the ice edge in the western Labrador Sea, Fram Strait and the northern Irminger Sea, and a little too low in the Iceland and Greenland Seas.

The MM historical run is significantly different to the HH run in places. It simulates far too much sea ice in the Iceland and Greenland Seas, with these regions being mostly ice covered; although, in contrast to the HH historical run, the northward position of the ice edge in the Barents Sea is in good agreement with ERA5. The Icelandic Low is too shallow, with its centre around 3 mb higher than ERA5 representing a significant difference in the representation of the atmospheric circulation and wind speeds over the SPNA. Under representation of extratropical cyclones is a feature of lower resolution atmospheric models (e.g., Jung et al., 2006). The surface air temperature field in the MM historical model is very similar to the HH model and agrees well with ERA5. The magnitude of peak turbulent heat fluxes in the Labrador Sea and Fram Strait is slightly lower than the HH model and closer to ERA5. However, the substantial amount of extra ice in the Iceland, Greenland and Irminger Seas leads to incorrect surface heat fluxes in these regions. In both models the fluxes are too low in the Iceland and Greenland Seas, and too high in the Irminger and Labrador Seas and the Fram Strait. In the Barents Sea the models show good agreement with ERA5, though the concentration of sea ice east of Svalbard is too low in the HH historical simulation. Both resolutions simulate the magnitude of Norwegian Sea flux reasonably well but with an incorrect east-west gradient due to the overly low fluxes to the west.

5.3.2 Regional means

Analysis of regional climatological winter means (and interquartile ranges) enables a more detailed evaluation of the simulations' veracity (Figure 5.3). The MM historical model produces far too much sea ice in the Greenland and Iceland Seas with a median sea ice concentration over the regions of approximately 90% and 65% respectively, compared with 50% and 10% in the ERA5 record. In the Fram Strait sea ice is also overestimated by the MM historical yet underestimated in the Barents and Labrador Seas.

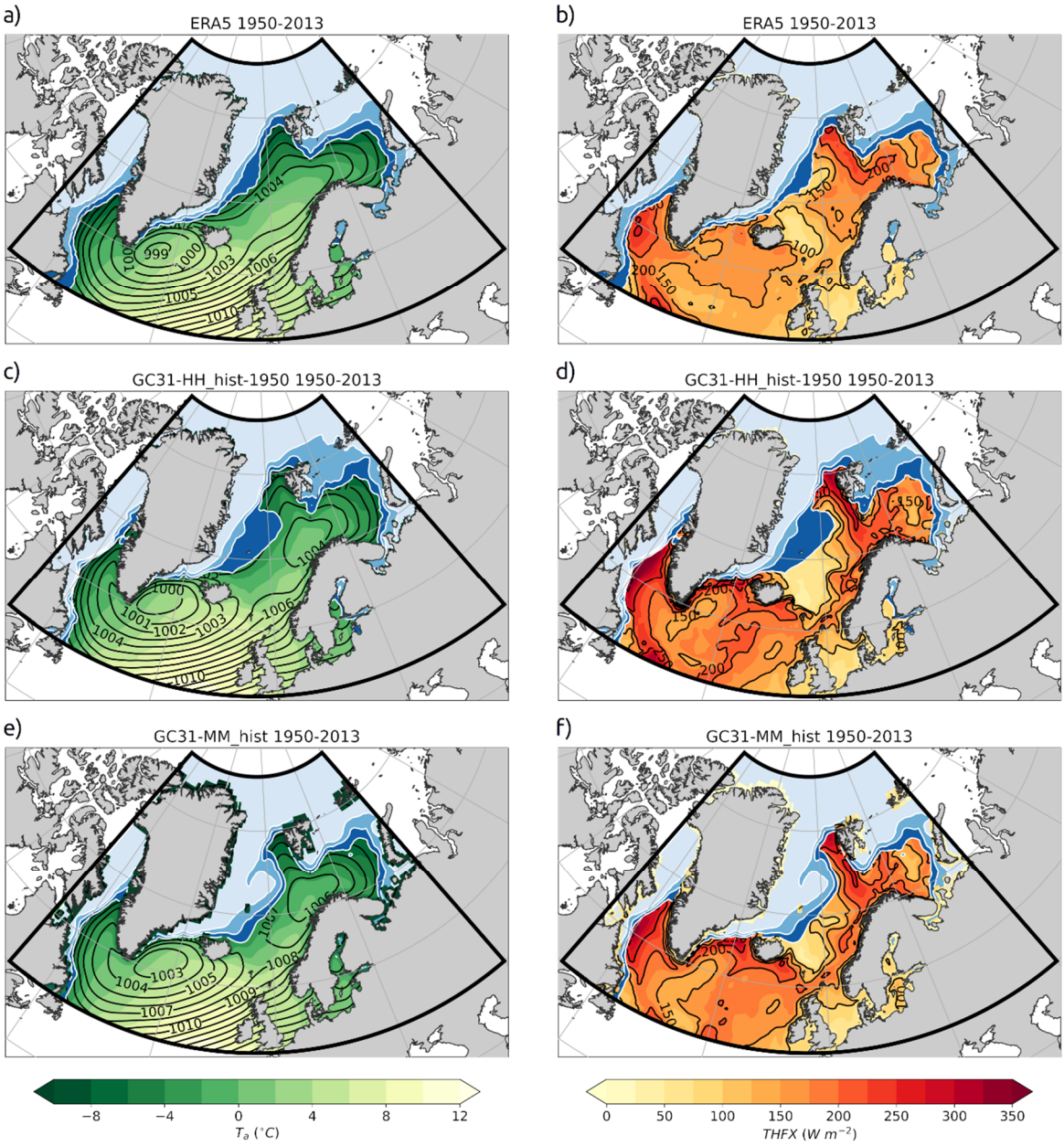

Figure 5.2 Spatial distribution of climatological (1950-2013 DJFM) sea ice contours (25%, 50%, 75%), sea-level pressure (black contours) and 2m air temperature (coloured shading) in the left column and sea ice and total turbulent heat flux (coloured shading) in the right column for ERA5 reanalysis in a) and b); HadGEM3-GC3.1 HH historical in c) and d); and HadGEM3-GC3.1 MM historical in e) and f).

The advanced sea ice extent causes substantial bias in the MM historical in the Iceland and Greenland Seas with a cold bias in T_s of approximately 5 – 10 °C. It follows that the MM historical simulation exhibits poor skill in these regions for linked variables, and indeed T_a and *THFX* are significantly lower than ERA5. Despite reasonable agreement with ERA5 in the other regions, overall, the MM historical appears to provide a relatively poor reproduction of air-sea interactions in the SPNA.

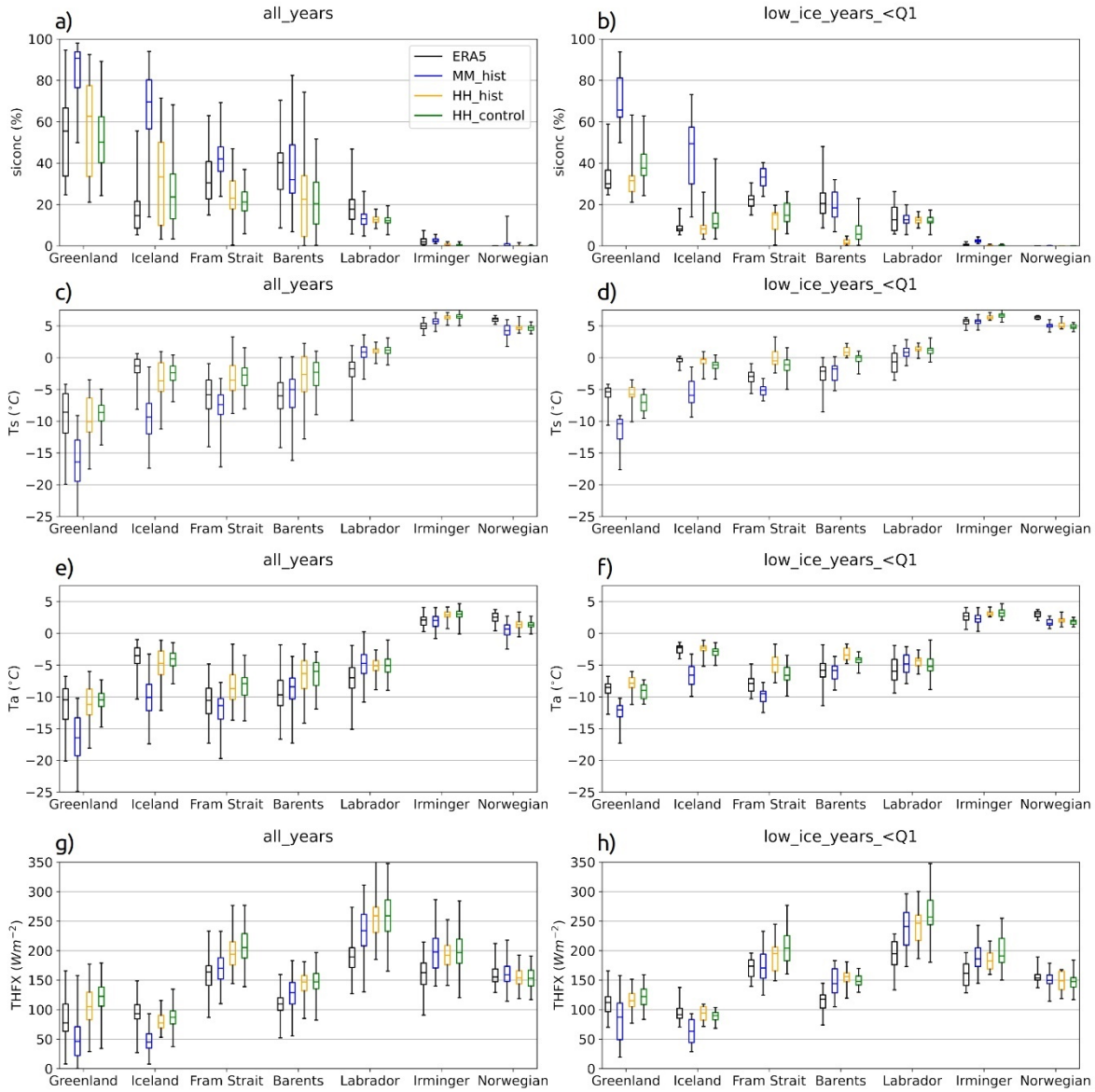

Figure 5.3 Box and whisker plots for surface variables across seven regions, using output from ERA5 (1950-2013), and the models MM historical, HH historical and HH control (see Table 1). The variables are for DJFM, with the left column displaying data for all years and the right column displaying data for low ice years.

In contrast, the HH historical run displays improved agreement with ERA5 in sea ice over the Greenland and Iceland Seas, though the interquartile range is too large and somewhat biased towards higher ice concentrations. As seen in the spatial plots, the HH model tends to underestimate the amount of sea ice a little in the Fram Strait and Labrador Sea, but the interquartile range largely overlaps with ERA5. Sea ice is more significantly underestimated in the Barents Sea due to the ice edge lying too far to the north. Again, the result is elevated *THFX* in these regions in the HH historical run. The Norwegian and Irminger Seas are mostly ice free, which the models reproduce well.

The discrepancies in T_s, T_a and *THFX* for both model resolutions are qualitatively the same and clearly related to errors in sea ice distribution. However, the HH model displays notably warmer T_s in all regions compared to the MM simulation, likely linked to the increased northward heat transport into the SPNA in the higher resolution configuration (Roberts et al., 2020). The result is enhanced *THFX* in the HH historical and the HH control simulations, with a larger bias in the Fram Strait and Barents and Labrador Seas than the MM historical. Furthermore, the distribution of T_s biases also suggests that current pathways are not perfectly simulated. However, overall, the HH surface variables correspond more closely to ERA5, i.e., the higher resolution improves the fidelity.

5.3.3 Conditional sampling by sea ice extent

As the representation of sea ice is the largest source of variability and error in the model simulations of *THFX*, one wonders how the relative influence of sea ice will change as it declines over the 21st century. Is it possible that retreating sea ice will improve the fidelity of simulated air-sea interaction? We address this question by conditionally sampling the historic simulations using quartiles of winter mean sea ice extent to evaluate model performance during 'low' and 'high' ice years.

Low and high ice years are defined for each simulation, rather than from the observational record, to enable a statistical assessment. Each simulation is conditionally sampled to select winters that have lower (<Q1) or higher (>Q3) than average sea ice extent in the whole SPNA. A spatial illustration for low ice years is provided in Figure 5.4 and high ice years in Figure 5.5 via difference plots between the historical model simulations and ERA5 for sea ice and *THFX*.

The HH historical simulation shows very good agreement the in the Iceland and Greenland Seas in low ice years, while the MM historical has far too much sea ice. The HH control run also corresponds well to ERA5 in these regions. In the Fram Strait the HH historical does not produce enough sea ice, while the MM historical model produces too much. Both the HH historical and control runs do not simulate enough ice in the Barents Sea, suggesting that ocean heat transport into this region may be too high. Indeed, surface temperature in the Barents Sea and Fram Strait is on average too high in the HH simulations (Figure 5.3). All the simulations are accurate during low ice years in the Labrador Sea, albeit with insufficient variability.

Generally, the HH control configuration tends to produce more sea ice in each region compared to HH historical as would be expected with constant 1950s climate forcing compared to imposed warming in the historical simulation. Overall, the HH historical simulation represents *THFX* over

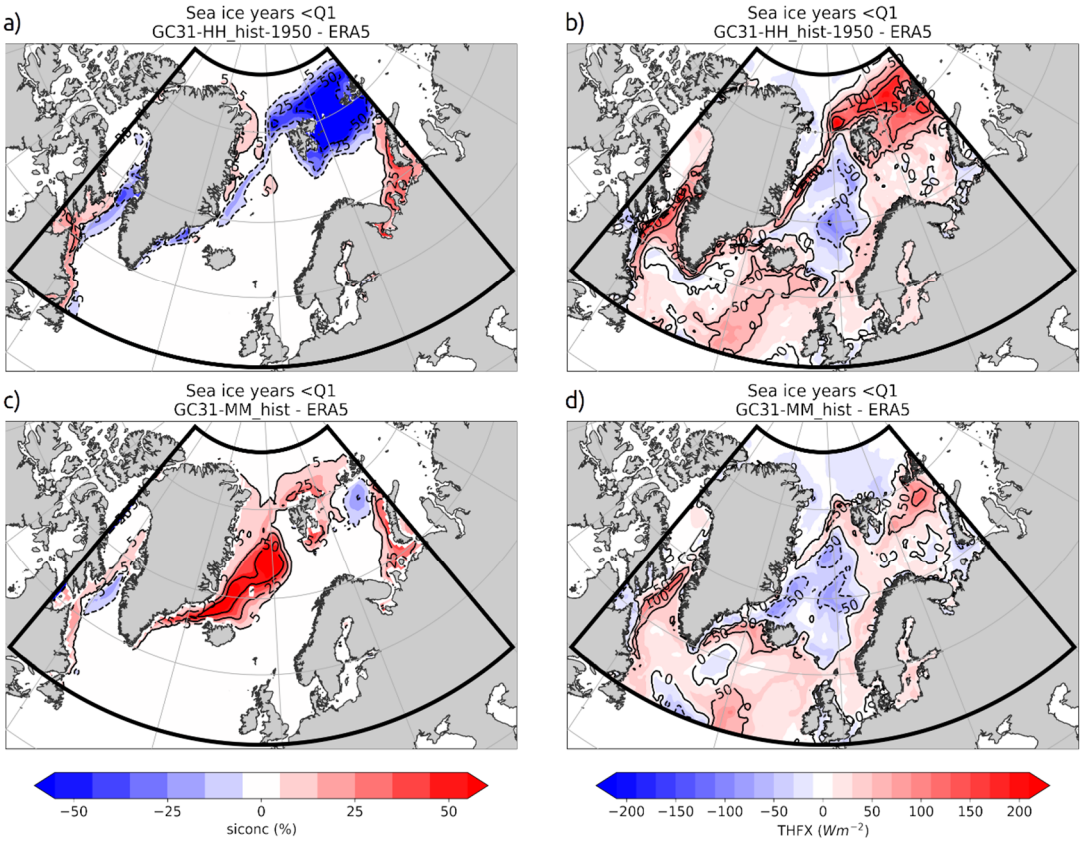

Figure 5.4 Spatial difference plots compared to ERA5 for DJFM HadGEM3-GC3.1 HH historical in a) and b) and HadGEM3-GC3.1 MM historical in c) and d). The left column displays sea ice concentration and the right column is THFX. Each product has been conditionally sampled based on winter mean sea ice concentration in the subpolar North Atlantic region in each model, so that the lower quartile represents the composited 'low ice years'.

the SPNA closer to ERA5 than the MM historical during low ice years, though slightly too high in Fram Strait and Barents Sea due to a retreated sea ice edge.

In the high ice years, the MM historical model invariably produces near-continuous ice cover over the Greenland Sea study region, however, in ERA5 the wintertime mean ice cover is typically 60% to 80% (not shown). The insulative layer of sea ice mostly prevents model air-sea interaction in this region. This problem is also exhibited over the Iceland Sea region: the MM historical model simulates the range of mean sea ice concentration to be 70% to 90%, while in ERA5 the value ranges between 10% and 50%. This is a result of an Odden Ice Tongue feature (e.g., Wadhams et al., 1996) occurring too often in the MM historical model and causes large errors in the turbulent heat fluxes (Figure 5.5).

The more accurate simulation of sea ice in low ice years by the HH historical in the Iceland and Greenland Seas translates to a much more accurate representation of T_a and T_s than the MM resolution. For the other regions the HH historical is more accurate apart from Fram Strait and

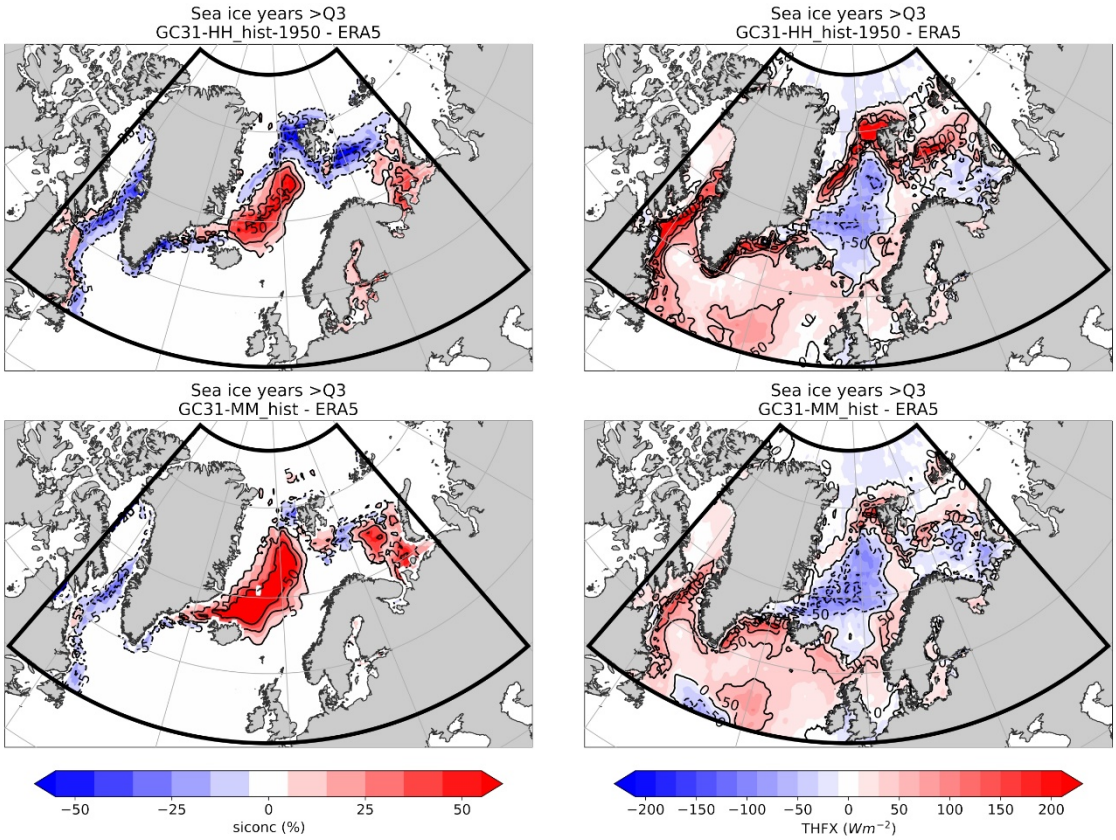

Figure 5.5 As Figure 5.4 but for the 'high ice years', in which winter mean sea ice concentration in the subpolar North Atlantic was in the upper quartile.

Barents Sea where sea ice is too low. Nonetheless, the HH historical simulates THFX more accurately or on par with the MM historical in all regions.

The HH historical displays a substantial lack of sea ice in the Barents Sea region, with the model tending to produce open water north of Svalbard (Figure 5.4). We suggest this may be the result of too much ocean heat transport into this region. Otherwise, the HH historical is generally in good agreement with ERA5, however, biases in *THFX* are shown to be closely related to biases in sea ice. A slightly retreated ice edge around Greenland results in a misplacement of *THFX* maxima, and the missing ice north of Svalbard and in the Barents Sea results in excessive *THFX*.

A difference between the lower and upper quartiles of sea ice in the HH historical run is the clear stamp of an overly frequent occurrence of the Odden Ice Tongue in the upper quartile, with the model producing too much ice in the Iceland and Greenland Seas on average and *THFX* that is too low (Figure 5.5). However, elsewhere the ice edge is retreated during the high ice years in the HH historical simulation. This leads to sizeably elevated *THFX* in these areas compared to ERA5 and could be another signal of that ocean heat transport into the SPNA is too strong in the HH model.

In comparison, the MM historical simulation produces the Odden Ice Tongue feature even in the low ice years, representing a significant error in the model sea ice in the Iceland and Greenland Seas (Figure 5.4). However, elsewhere the sea ice is in good agreement with ERA5, with the position of sea ice edge more accurately reproduced than the HH historical in the Barents and Labrador Seas. The correlation between sea ice and *THFX* biases is clear, with large overestimation of ice extent in the Iceland and Greenland Seas resulting in a lack of *THFX* in these regions.

Far too much sea ice is simulated by the MM historical run in the Iceland and Greenland Seas during the high ice years (Figure 5.5). This results in a wide area of *THFX* that is lower than ERA5. Also, this model configuration also produces a large amount of sea ice in the southern Barents Sea. Elsewhere the ice edge is closer to ERA5 than simulated by the HH historical run, which results in less extreme bias in *THFX* maxima.

Overall, the boxplots appear to show that the HH model simulates *THFX* more accurately than the MM model in all the study regions except for the Barents Sea (Figure 5.3); yet the spatial difference plots reveal that there are both strengths and weaknesses in the HH simulation (Figure 5.4). The sea ice extent in the Iceland and Greenland Seas is comparatively accurate during low ice years, but this is countered by a substantial lack of sea ice in the Barents Sea. Both model resolutions exhibit a tendency to produce a sea ice edge that is too far retreated in the Labrador Sea.

5.4 Decadal trends to 2100

5.4.1 Decadal time series

To analyse the future trends on a regional basis, time series of decadal means and decadal standard deviations are presented for each product. This provides not just insight into the model trends but also the degree of variability during each decade.

Winter sea ice is projected to almost entirely retreat from the SPNA over the course of the 21st century under SSP5-8.5 forcing (Figure 5.6a). The HH and MM resolution simulations under this forcing generally agree from the 2030s, however, during the 2020s, the large bias in sea ice extent seen in the MM historical simulations in the Iceland and Greenland Seas appears to persist. The result is an unrealistic deviation from the decreasing trend in sea ice since the 1970s in ERA5. However, as sea ice reduces in subsequent decades the MM simulations project sea ice extent much more similar to the HH simulation and the trends seen in ERA5 if extrapolated.

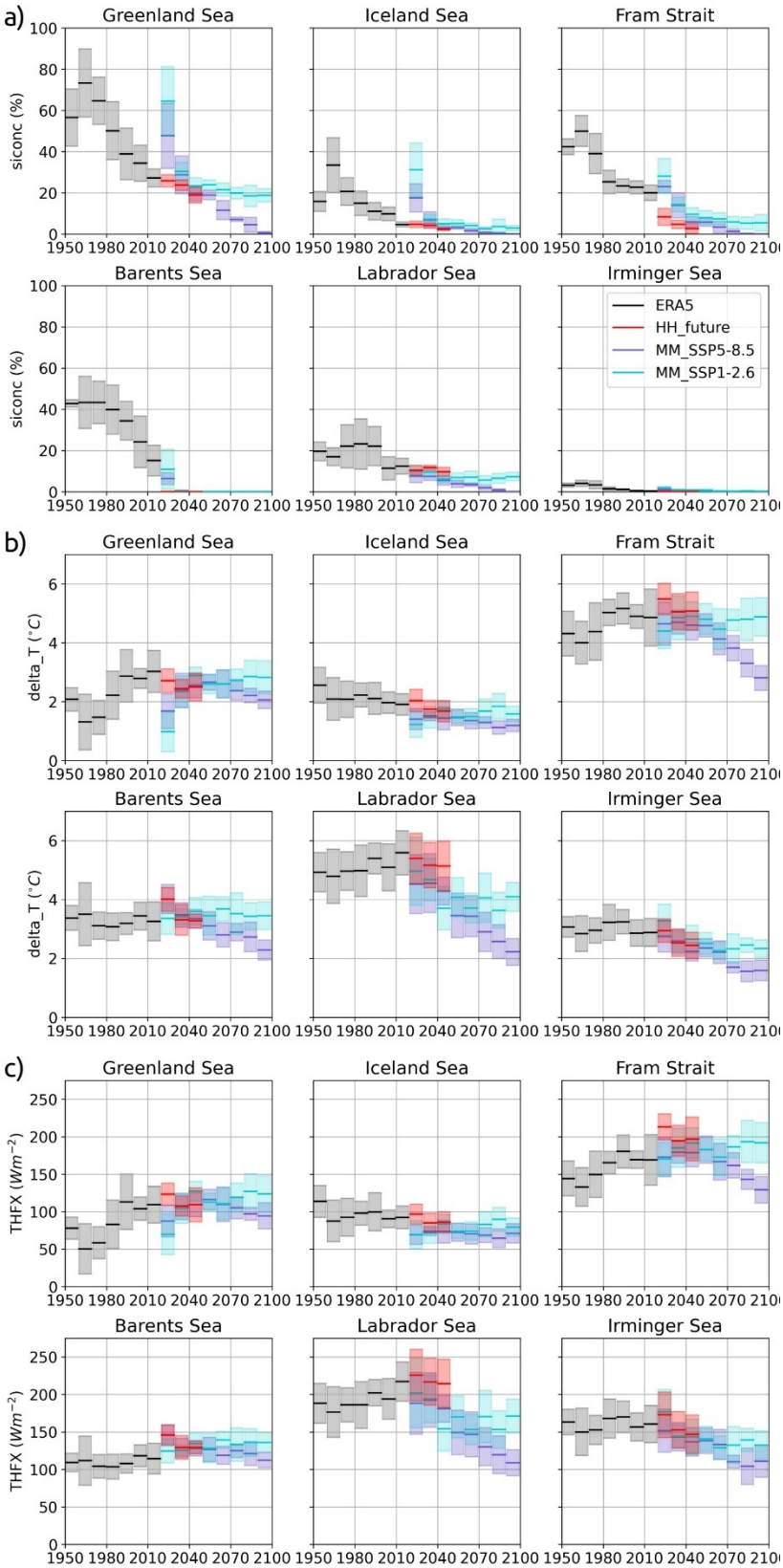

Figure 5.6 Regional time series of decadal means (thick lines) and decadal variability indicated by +/- 1 standard deviation (shaded regions) for the historical ERA5 record (1950-2020; black), and the future simulations from HadGEM3-GC3.1: HH future (2020-2050; SSP5-8.5 forcing; red), MM SSP1-2.6 (2020-2100; cyan), and MM SSP5-8.5 (2020-2100; purple) for DJFM where a) sea ice concentration, b) ΔT (°C), and c) total turbulent heat flux (Wm^{-2}).

We have suggested that as atmosphere and ocean temperatures increase, resulting in reduced winter sea ice, climate projections may benefit from reduced uncertainty associated with predicting sea ice variability. This is consistent with the mean CMIP6 ensemble prediction, in which the Arctic is predicted to become ice free (<1 million km^2) in summer under emissions scenarios SSP2-4.5 and above, with wintertime sea ice falling substantially (Notz et al., 2020). Under SSP1-2.6, CMIP6 ensemble mean Arctic sea-ice area stabilises at around 13 million km^2 in the second half of the 21st century (Notz et al., 2020). This is reflected by the slowing rate of decline and stabilisation of sea ice towards 2100 in the MM SSP1-2.6 simulation for the Greenland, Iceland and Labrador Seas and the Fram Strait region (Figure 5.5a).

The impact of the influence of differential warming in the atmosphere and the ocean is illustrated via $\Delta T = T_s - T_a$. Projected changes in the air-sea temperature gradient provides a useful measure of the changing atmospheric forcing for ocean convection, particularly when T_a and T_s are both projected to strongly increase. Under the high emissions scenario, SSP5-8.5, ΔT shows generally good agreement between the HH and MM models in a downward trend to 2050, with substantial further decreases to 2100 (Figure 5.6b). In the Greenland Sea and Fram Strait sea ice has been the dominant control of air-sea temperature gradients in the ERA5 record. As sea ice decreased since around 1970, the uncovering of the warmer ocean surface beneath resulted in an increase in ΔT. However, as atmospheric warming is projected to increase at a faster rate compared to ocean temperature in the future, this trend will become reversed and result in reducing air-sea temperature gradients. In the Iceland, Barents, Norwegian and Irminger Seas the gently declining trend of reducing air-sea temperature gradient in the ERA5 record is projected to continue as the atmosphere warms. The overall result of declining ΔT values in the future will have a direct impact on the ability of the atmosphere to extract heat from the ocean. Under the less severe SSP1-2.6 emissions scenario ΔT is projected to remain relatively stable during the period 2050 to 2100 across the subpolar North Atlantic.

The subpolar North Atlantic appears to be entering a new, more homogeneous regime, whereby the disappearance of ice results in increasingly similar T_a and T_s across the spatial regions. In regions where more ice is lost, the more dramatic the change in temperature over the 21st century, particularly in the Greenland Sea and Fram Strait, where, compared to 1950s observations, T_a is projected to be roughly 10°C to 15°C warmer by 2100 between SSP1-2.6 and SSP5-8.5. Such a temperature increase represents a drastic change in atmospheric forcing on the ocean. The HH model out to 2050 corroborates the MM SSP5-8.5 simulation.

Overall, *THFX* over the SPNA is projected to decrease through the 21st century under SSP5-8.5, with pronounced reductions in the Labrador and Irminger Seas under SSP1-2.6 as well (Figure 5.6c). The HH future simulation generally corroborates the MM SSP5-8.5 simulation from the 2030s, as for sea ice, though with slightly higher *THFX*. As such, a significant reduction in dense water formation in the SPNA is anticipated under SSP5-8.5. However, in the Greenland and Barents Seas and Fram Strait the different future warming scenarios have divergent implications. These regions see a small increase in *THFX* under SSP1-2.6 over the course of the century, while SSP5-8.5 results in a significant reduction. This difference arises from the interplay between the retreating sea ice exposing relatively warm currents to the atmosphere (Moore et al., 2022) and the degree to which overall air-sea temperature difference decreases. In all areas, the more stable sea ice conditions and global mean temperature under SSP1-2.6 in the latter half of the 21st century result in stable *THFX*, which in turn would limit the impact on atmospheric warming on dense water formation for the AMOC.

Further, loss of wintertime sea ice leads to a noticeable reduction in the decadal variability of ΔT and *THFX*. This can be seen in comparison of the high and low warming scenarios. Again, this suggests that the SPNA will undergo a process of homogenisation with the loss of sea ice under strong anthropogenic climate change. The loss of the historically dynamic and varied environment represents a huge challenge for the native flora, fauna and human communities that live in the SPNA (Meier et al., 2014).

As sensible heat fluxes are directly proportional to the air-sea temperature gradient, it follows that sensible heat trends closely mirror those of ΔT. Sensible heat fluxes are predicted to significantly decline in under SSP5-8.5 forcing and remain relatively stable towards the end of the 21st century under SSP1-2.6 forcing (not shown). In contrast, increasing latent heat fluxes are projected under both warming scenarios in the Greenland and Barents Seas and in Fram Strait. We suggest that increasing latent heat fluxes in these regions is a 'fingerprint' of the exposure of current pathways to relatively dry cold-air outbreak airmasses.

5.4.2 Spatial distribution during the mid and late 21st century

In the decade 2040-2049 there is good qualitative agreement between the model simulations in the retreat of the ice edge in the Iceland and Greenland Seas, and to the north of Fram Strait and Barents Sea (Figure 5.7). The T_a field is also similar between the three projections, though with the warmer contours advanced further north in the simulations under SSP5-8.5 forcing. Warming air temperature in the SPNA is increased with higher latitude, up to 5 °C where sea ice

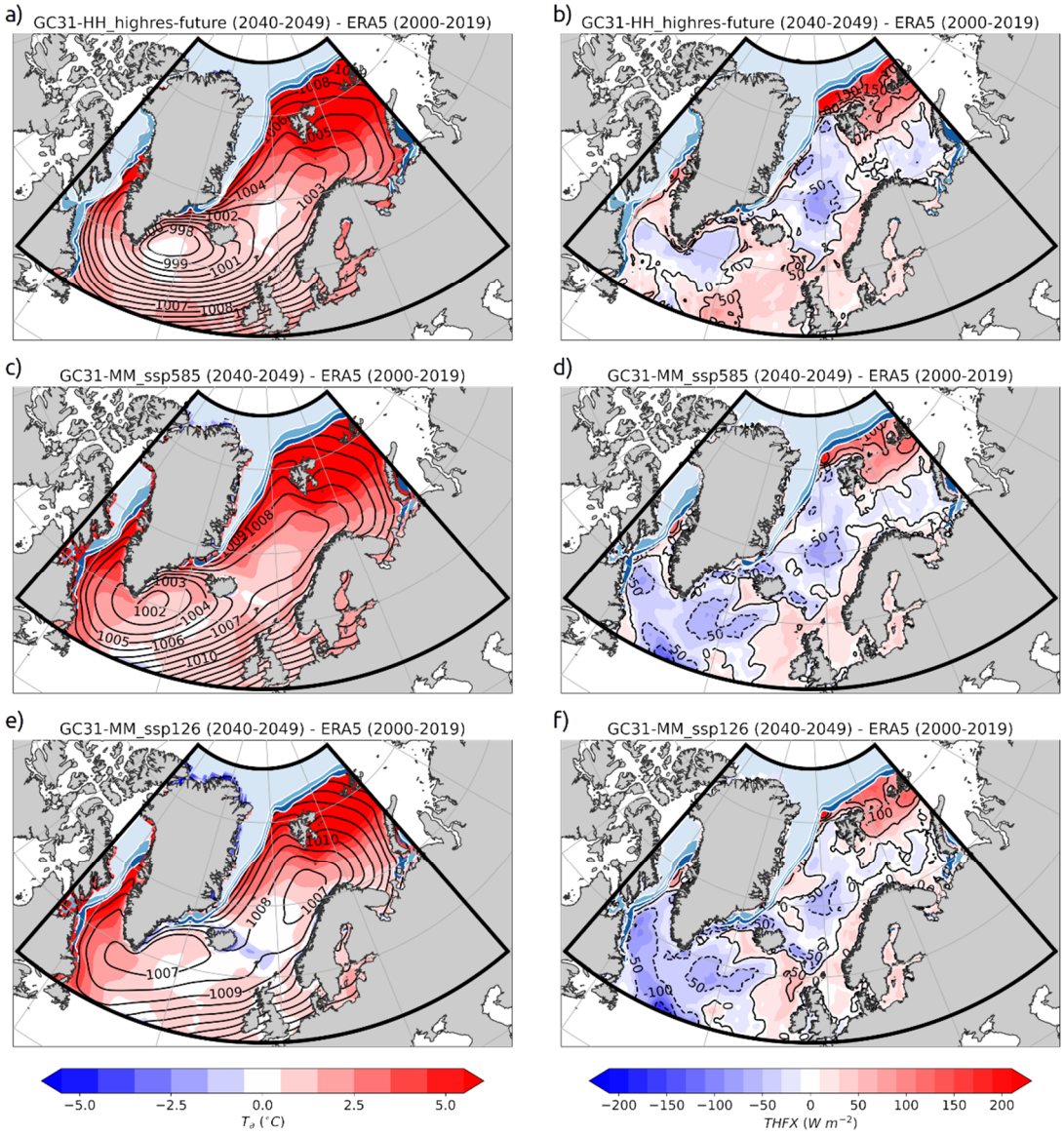

Figure 5.7 Spatial distribution of mid-century (2040-2049) sea ice, sea-level pressure with 2 m air temperature anomaly using the ERA5 base period (2000-2019) in the left column; and sea ice with total turbulent heat flux anomaly using the same base period in the right column for HadGEM3-GC3.1 HH future in a) and b); HadGEM3-GC3.1 MM SSP1-2.6 in c) and d); and HadGEM3-GC3.1 MM SSP5-8.5 in e) and f).

has retreated north of Svalbard relative to the ERA5 base period of 2000-2019, representing a strengthening of Arctic Amplification (Serreze & Barry, 2011).

The *MSLP* fields display significant differences between simulations. HH future features a deep Icelandic Low of around 998 mbar, MM SSP5-8.5 is shallower at around 1002 mbar, but MM SSP1-2.6 is much shallower at 1007 mbar. As discussed earlier, the *MSLP* field in the HH historical simulation is much closer to ERA5 than the MM historical simulation, due in part to orographic processes being better resolved. Nonetheless, increased atmospheric forcing under SSP5-8.5 appears to result in a strengthening of the Icelandic Low around the middle of the 21st century

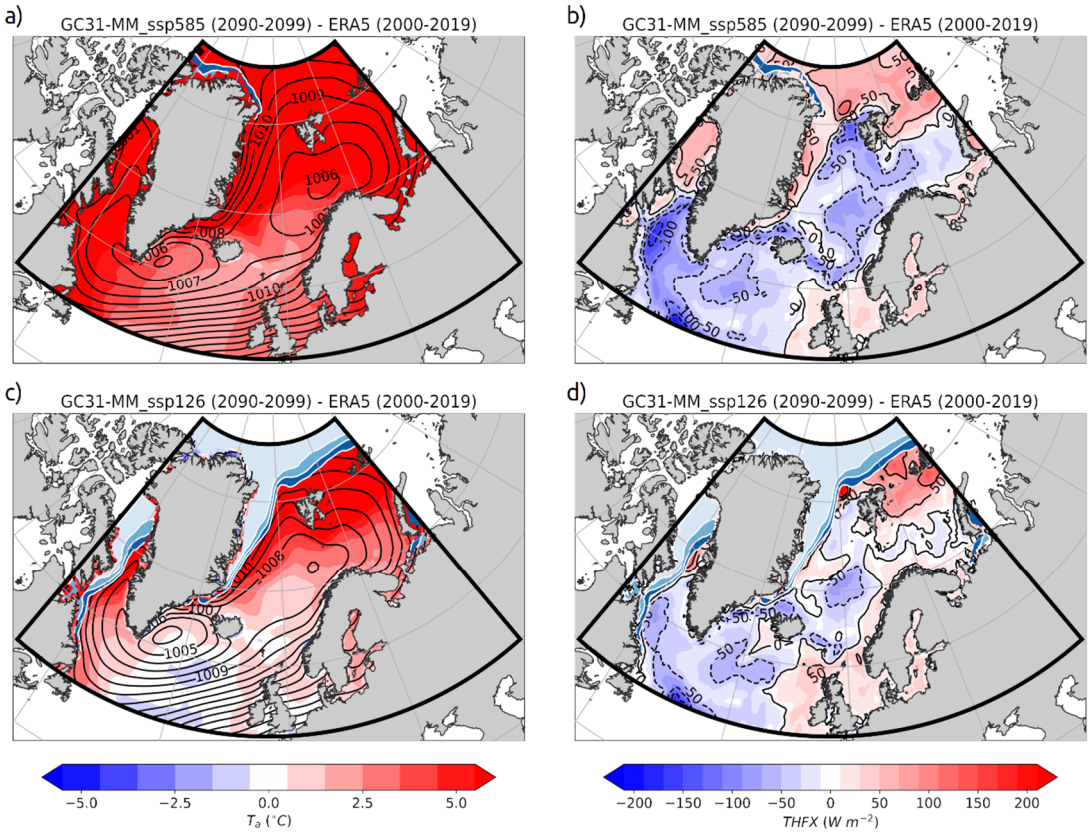

Figure 5.8 Spatial distribution of the late 21st century (2090-2099) sea ice, sea-level pressure with 2 m air temperature anomaly using the ERA5 base period (2000-2019) in the left column; and sea ice with total turbulent heat flux anomaly using the same base period in the right column for HadGEM3-GC3.1 MM SSP1-2.6 in a) and b); and HadGEM3-GC3.1 MM SSP5-8.5 in c) and d).

in both HH and MM simulations, whereas the climatological low is weaker in the MM SSP1-2.6 simulation.

Over the interior of the Nordic Seas basin, winter mean *THFX* is projected to decrease in all of the simulations by the 2040s, by over 50 Wm^{-2} in the centre of the basin. Conversely, a small increase is projected in the boundary regions along the Norwegian coast and where sea ice has retreated towards Greenland. Likewise, to the north of Fram Strait and the Barents Sea there is a substantial increase in *THFX* with sea-ice retreat in all the simulations, associated with a dipolar reduction in *THFX* to the south in these regions as found by Moore et al. 2022 in historic sea ice decline. The two model resolutions most notably diverge around the Irminger and Labrador Seas, where the HH future projects a small reduction in *THFX* away from coasts but the MM simulations under both warming scenarios project a substantial and more widespread reduction. The HH and MM historic simulations were relatively similar in this region, hence weaker mean winds in the MM simulations related to the shallower Icelandic Low is probably the primary reason for lower heat fluxes, though reduced ocean heat transport may also be a

factor. Overall, the model resolutions are qualitatively similar in spatial distribution of sea ice and *THFX* increasing confidence in the MM model's ability to project further into the future.

Late in the 21st century (2090-2099; Figure 5.8) the two MM simulations diverge considerably, with the high radiative forcing in SSP5-8.5 causing dramatic atmospheric warming and a total retreat of sea ice from the SPNA. In contrast, MM SSP1-2.6 distribution is reasonably unchanged compared to the MM projections for the decade around the mid-21st century, most closely resembling that of SSP5-8.5 in the 2040s. This suggests that should anthropogenic emissions be kept to a minimum over this century and atmospheric warming limited, the wintertime SPNA may reach a new state of relative equilibrium.

However, under a runaway warming scenario due to a fossil fuel intensive economy, the MM SSP5-8.5 simulation projects a radically different regime for the SPNA with virtually no remaining wintertime sea ice, even in the 'Last Ice Area' north of Greenland where the oldest and thickest sea ice typically occurs (Moore et al., 2019). In northwest Europe, the climate would be much warmer than at present, with any reduction in warming effect from a slowing AMOC strongly outweighed by the substantially warmer global mean T_a. The substantially reduced air-sea temperature gradients result in a reduction in *THFX* over the majority of the SPNA, though with increased *THFX* where sea ice no longer exists. This translates to a substantial reduction in

atmospheric forcing of water mass transformation in the region. After deepening by the mid-21st century, the Iceland Low in MM SSP5-8.5 at the end of the century has reduced in strength, while for MM SSP1-2.6 the reverse is true. This hints that with increasing climate warming the NH polar jet will continue the trend of increasing strength observed in the historical record over the North Atlantic (Hallam et al., 2022) up until a point, but thereafter a decline will occur.

5.4.3 Integrated turbulent heat fluxes

We find a projected overall decrease in the magnitude of *THFX* in the SPNA over the 21st century, however, large reductions in sea ice will open more of the ocean to be in direct contact with the atmosphere. Thus, a simple quantification of the total effect on overall air-sea heat exchange can be calculated by integrating every non-land grid cell in the defined SPNA region over area and time during each winter. Figure 5.9 shows trends in the heat exchange from the 1950s-2100 from ERA5 and the historical and future simulations. ERA5 shows a positive trend in upwards air-sea heat exchange from 1950-2021 of 0.11 x 10^{21} J decade^{-1} linked in part to the observed reductions in sea ice extent (Moore et al., 2015, 2022), but also shown to be partly the result of increased atmospheric forcing (Li et al., 2022). This trend is simulated well in HH historical (0.08 x 10^{21} J decade^{-1}), though with higher total heat exchange due to sea ice extent that is too low

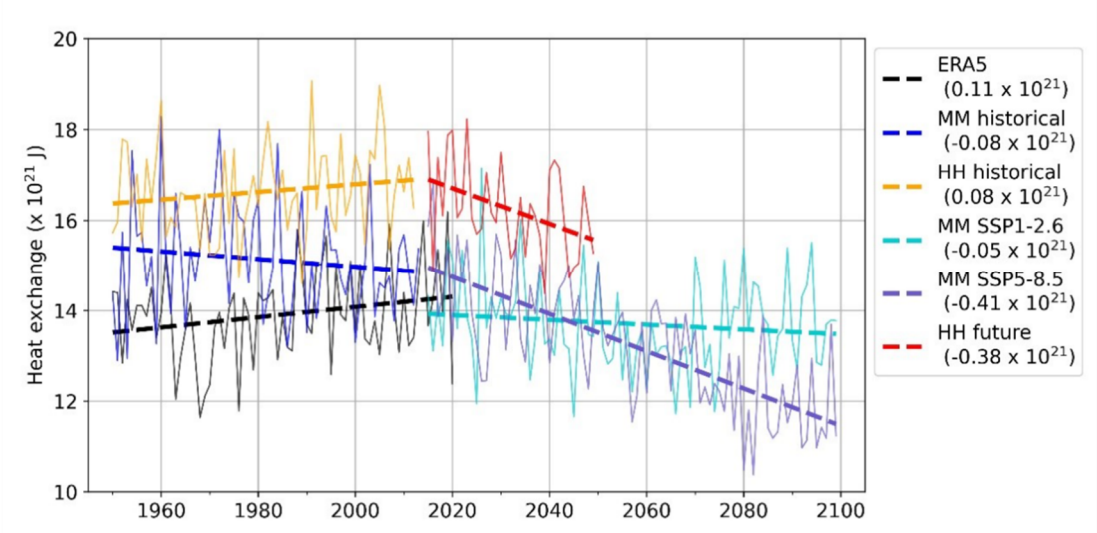

Figure 5.9 Time series of integrated wintertime heat exchange (positive upward) over the subpolar North Atlantic. The integrated ocean heat loss is calculated from the surface turbulent heat flux, with annual values (thin lines) and linear fits (thick dashed lines) shown for ERA5 (black), MM historical (blue), HH control (green), HH historical (orange), MM SSP1-2.6 (cyan), MM SSP5-8.5 (purple) and HH future (red). Decadal trend values (J decade^{-1}) are noted in the legend.

in the Barents and Labrador Seas and Fram Strait (c.f. Figure 5.3). The HH control also simulated a heat exchange that is systematically biased high (not shown). In contrast, MM historical simulates a negative trend, though is closer to ERA5 towards the end of the simulation. We hypothesise this is linked to its initially poor representation of sea ice (e.g., its persistent Odden ice tongue) which significantly affects its *THFX* distribution. The HH future simulation predicts a relatively sharp decline in the heat exchange trend from THFX to 2050 (-0.38 x 10^{21} J decade^{-1}). Under the same climate forcing, MM SSP5-8.5 predicts a remarkably similar trend (-0.41 x 10^{21} J decade^{-1}), resulting in a substantial reduction in heat exchange towards 2100. The trend for MM SSP1-2.6 is also negative but is weaker. The simulated decreases in ocean heat loss are due to changes in sea-ice distribution and the temperatures of the atmosphere and ocean. The different climate forcing scenarios directly affect the sea ice and T_a, while T_s is also affected by the declining strength of the AMOC in these simulations (Roberts et al., 2020). The implications of this reduction in ocean heat loss would be a reduction in the formation of dense waters that feed into the lower limb of the AMOC.

5.5 Discussion

Broadly the HH and MM historical simulations agree reasonably well with the ERA5 climatology in the subpolar North Atlantic in terms of their mean spatial distribution of sea ice concentration, *MSLP*, T_a, T_s and *THFX* in wintertime during the period 1950-2013. However, there are some

regional issues, largely related to errors in the model production of sea ice. The Iceland and Greenland Seas are a critical area where it is common for the models to simulate too much sea ice cover due to the overly frequent development of the Odden Ice Tongue, particularly at the MM resolution. This has a negative impact on the performance of other modelled variables. To see if the model performance is better in some scenarios, we conditionally sample for low sea ice years and find a general improvement. In this low ice regime, the models benefit from improved means and reduced uncertainty due to reduced sea ice variability. The implication is that for future simulations, when there is less sea ice in the SPNA, the models will be comparatively accurate.

The Odden Ice Togue feature that develops too often in the MM historical simulation provides insight into the representation of physical mechanisms in the model. From observations, the Odden Ice Tongue is formed in one of, or a combination of, two modes: from locally formed frazil and pancake ice over the pre-cooled Jan Mayen current that splits eastward off the East Greenland Current; or from older sea ice advected from the coast of Greenland eastwards by the Jan Mayen current (Wadhams & Comiso, 1998). Both modes are dependent on the hydrographic properties of the Jan Mayen current, thus a signature is decipherable that the MM historical simulation must be poorly representing the current pathways and ocean heat redistribution in the region. The HH simulation on the other hand, with the ability to resolve fluid motion to a finer degree, provides a more representative realisation of the subpolar North Atlantic.

The recent Physical Science Basis report by the Intergovernmental Panel on Climate Change (Lee et al., 2021) states that, compared to 1850-1900, global surface temperature averaged over 2081-2100 is very likely to be higher by 1.3°C to 2.4°C under the low emissions scenario (SSP1-2.6), or 3.3°C to 5.7°C warmer under the very high emissions scenario (SSP5-8.5). Here we show the effects of these two scenarios on sea ice and air-sea turbulent heat fluxes in the SPNA later in the 21st century. The MM and HH simulations have been shown to project a stronger decline in the AMOC to 2050 under SSP5-8.5 forcing than coarser CMIP6 models (Roberts et al., 2020). It has been suggested that this is due to a larger decrease in dense water formation in the subpolar gyre and Labrador Sea (Jackson et al., 2020). Here we show that this is concurrent with a substantial reduction in atmospheric forcing by turbulent heat fluxes.

Roberts et al. (2020) found that of the HighResMIP models, the eddy-rich HadGEM3-GC3.1 HH and CESM1-3 HH (Small et al., 2014) models reproduce AMOC depth profiles, zonal mean temperature and salinity the best. Here, we add that HadGEM3-GC3.1 HH generally produces a

qualitative better sea ice and turbulent heat flux distribution for the SPNA compared to the MM configuration. However, despite the improved AMOC and hydrographic properties in the SPNA, the HH has too little sea ice in the Barents Sea and north of Fram Strait. This may be linked to an increased northward heat transport, and the current pathways in the model.

As the global climate changes, so too will the fringe areas of sea ice. Strong & Rigor (2013) found that over 1979-2011 the Arctic MIZ has widened by 39% in summer and narrowed by 15% in winter. With further warming the MIZ will continue to change in location and characteristics, eventually disappearing northwards from the coasts of Greenland entirely. We suggest that, through the evaluation of below (and above) average sea ice years in historic model simulations against ERA5, the models perform better in winters when sea ice is reduced. From this we gain confidence in the MM resolution simulations from the 2030s as sea ice becomes less prevalent in the SPNA, corroborated by the MM simulations converging with the HH simulation towards 2050.

The projections presented suggest that wintertime sea ice later in the 21st century will be consistently closer to the Greenland coast and farther north of Svalbard. Positive winter air-sea temperature gradients, driven by cold-air outbreaks, will reduce over the 21st century, particularly under SSP5-8.5 forcing. Overall, turbulent heat fluxes decrease over the SPNA region, reducing atmospheric forcing of ocean convection. In CMIP6 models, AMOC decline is associated with a decline in North Atlantic Deep Water formation (Weijer et al., 2020). However, significant THFX over northward flowing Atlantic water west of Svalbard and over the East Greenland Current (EGC) complicates the projected future for water mass transformation along key branches of the subpolar AMOC. In the western Iceland Sea re-ventilation and a deepening mixed layer has been observed along the EGC made possible by the retreat of the ice edge in recent years (Våge et al., 2018). Further, change in sea ice near key current pathways in the Nordic and Barents Seas has been shown to be affecting where and how water mass transformation occurs.

Over the EGC a significant increase in *THFX* has been observed since 1950 due to the current's orientation being perpendicular to the axis of sea ice retreat, therefore the entire current system has been exposed to the atmosphere at the same time; however, the northward flowing currents to the east of Svalbard and in the Barents Sea have seen dipolar changes along the current length due to their orientation parallel to the axis of sea ice retreat (Moore et al., 2022). Here we show that this pattern of *THFX* changes due to sea ice loss over these key currents is expected to continue in the future, though local increases will be dwarfed by the wide scale

reduction in *THFX* over the SPNA due to differential warming in the atmosphere and the ocean under strong anthropogenic climate forcing.

Higher resolution atmospheric models typically perform better, in part due to more realistic orography (Jung et al., 2012). This issue is pertinent for the SPNA due to the large barrier of Greenland that influences large-scale atmospheric circulation and generates smaller-scale phenomena, such as topographic jets and mesoscale cyclones. Further, improved representation of mesoscale atmospheric forcing on the ocean in a high-resolution atmosphere model has been shown to increase the strength of wind driven gyres in the North Atlantic and the AMOC by around 5-10% compared to a coarse resolution (Jung et al., 2014).

We illustrate that in the MM historical simulation the Icelandic Low is too shallow by around 3 hPa, demonstrating that at 60 km atmospheric resolution it is underrepresented, while in the HH historical it is around 1 hPa too shallow. The HH future simulation suggests a 2 hPa deepening of the Icelandic low by the 2040s, while the MM simulations predict that it will become shallower by the end of the 21st century. In projections from the CMIP6 ensemble, it has been suggested that the NAO will not change substantially in respect to historical conditions (Cusinato et al., 2021). It appears that changes to air-sea interaction over the SPNA and their impacts on the weather of northwest Europe are far outweighed by the impacts of increasing global mean surface temperature and the associated worsening of hot weather and intense precipitation events (Seneviratne et al., 2021).

5.6 Conclusions

We evaluate historical simulations from the HadGEM3-GC3.1 model at medium-medium resolution (MM; 60 km atmosphere – 1/4° ocean) and high-high resolution (HH; 25 km – 1/12°), finding that both show reasonably good spatial agreement in sea ice and total surface turbulent heat fluxes (*THFX*) over the subpolar North Atlantic (SPNA). Overall, the HH model performs better than the MM, mainly due to a more representative ocean and more accurate sea ice. A particular problem for the MM historic is the simulation of too much sea ice in the Iceland and Greenland Seas, resulting in an inaccurate *THFX* distribution there. Our results demonstrate that the representation of sea ice is a major source of model variability and error in the SPNA. However, when conditionally sampling the MM historic output for winters with low ice extent in the SPNA, we show that its performance is improved in winters with less sea ice, which increases confidence in future projections as sea ice declines.

We show that winter sea ice is projected to substantially reduce in the SPNA over the 21st century, particularly under the high greenhouse gas emissions scenario, SSP5-8.5. This will affect the location and magnitude of peak turbulent heat fluxes, generally tracking the ice edge poleward. Also, rapid warming of the atmosphere will reduce the air-sea temperature gradient and the extraction of heat from the ocean. We find a negative trend in *THFX* in the Labrador Sea, Irminger Sea, and interior of the Nordic Seas. Under low emissions forcing (SSP1-2.6), these reductions in sea ice and changes to air-sea interactions are less severe than under high emissions forcing (SSP5-8.5), but still considerable.

Reduced *THFX* in winter will reduce the formation rate of dense waters that feed into the AMOC. This has the potential to compound the decreasing strength of the AMOC seen in recent years, with greater impacts possible from climate warming. However, changes in the position of *THFX* maxima near key ocean currents, such as over the East Greenland current (as it is increasingly exposed to the atmosphere), will have more complicated impacts on water mass transformation that require further investigation. Future work should also include investigation into the accuracy of AMOC pathways in high resolution models, specifically the inflows and outflows of the Nordic Seas basin and the mechanisms by which ocean heat is redistributed around the SPNA.

6 Conclusions

6.1 Thesis overview

Air-sea interaction in the subpolar North Atlantic region plays an important role in global atmospheric and oceanic circulation, and its simulation in both short- and long-range numerical weather and climate prediction models is critical for accurate forecasts. The region is partly responsible for some of the largest sources of uncertainty in model simulations due to a lack of observational data and weaknesses in the representation of physical air-sea-ice processes. Thus, the objective of this thesis has been to investigate and improve understanding of air-sea interaction and the influence of the marginal ice zone (MIZ) during cold-air outbreaks over the subpolar North Atlantic and their simulation in coupled ocean-ice-atmosphere numerical weather prediction models. This chapter summarises the research findings and conclusions drawn over the course of this thesis, as well as discussion on these results and recommendations for future research.

First, a brief synopsis of the research presented in this thesis. A comprehensive set of atmospheric and oceanic observations was collected as part of the Iceland-Greenland Seas Project (IGP). These data were quality controlled and synthesised to provide a rich data set for research (Chapter 2). Several case study periods within the IGP observational period were then outlined and used to investigate experimental coupled forecasts from the UK Met Office Global Coupled model version 2 (GC2; Chapter 3). This highlighted problems in the model representation of the MIZ with significant impacts on forecasted surface layer meteorology.

Next, as an updated model version became available from the Met Office, the Global Coupled model version 3.1 (GC3.1), a detailed analysis of its representation of the MIZ was performed (Chapter 4). Despite improvements over its predecessor, GC2, significant error in the representation of the MIZ remained in GC3.1. Sensitivity tests with ocean grid resolution and the surface momentum exchange parameterization scheme over the MIZ showed that the primary cause of error in the model simulations was due to the quality of the sea ice input field to the model.

In Chapter 5, the understanding of the influence of the MIZ on air-sea interaction developed in previous chapters was employed to evaluate long-range climate simulations of surface turbulent heat fluxes in the subpolar North Atlantic from the UK Met Office available as part of the Coupled Model Intercomparison Project Phase 6 (CMIP6). Weaknesses in historic simulations (1950-

2013) are shown to be strongly associated with inaccurate model sea ice. Future changes in the magnitude and distribution of turbulent heat fluxes over the region are shown to be dramatic and will have important implications for the location and magnitude of the formation of dense waters that feed into the lower limb of the Atlantic meridional overturning circulation (AMOC).

6.2 Research summary and limitations

Analysis of forecasts from GC2 using observations during three case studies in the Iceland and Greenland Seas showed that the MIZ was rather poorly simulated by this model configuration. A particular issue is the existence of too much low concentration sea ice in the outer MIZ, resulting in a simulated MIZ that is systematically too wide. Qualitative investigation into the development of the sea ice distribution during forecasts from GC2 suggested that it somewhat mirrored that observed by satellite sea ice analyses from OSTIA, hence appears to improve upon the persistent sea ice field in the uncoupled model. However, a problem arises from the coupled model MIZ being too wide with its surface temperature at sea water freezing point (-1.8 °C). This leads to an erroneous surface temperature field, which is evidenced using the in-situ observations made during the IGP. In all three case studies investigated, when the IGP research vessel was surveying near the MIZ, GC2 exhibits substantially larger T_s bias compared to uncoupled (atmosphere only) global operational forecasts.

A further issue of the wide outer MIZ is that the model surface roughness (z_{0_MIZ}) value is too high. The value of z_{0_MIZ} is set uniformly to 0.1 m, which has been shown to be too high over low concentration sea ice (Elvidge et al., 2016) and results in surface exchange that is too strong. Thus, the existence of too much low concentration sea ice (<15% SIC) in GC2 causes cold biased *SST* and over-estimated z_{0_MIZ}. However, in spite of these competing errors, the GC2 does in fact show some improvement over the uncoupled model in forecasting near-surface air temperature (T_{2m}) and relative humidity (RH_{2m}). It must be noted that a more sophisticated surface momentum exchange parameterisation scheme over the MIZ following Lüpkes et al. (2012) and Elvidge et al. (2016) has been implemented in the operational global forecast model by the Met Office since 25 September 2018 and has been shown to have positive effects for the entire atmospheric boundary layer (Renfrew et al., 2019b). Further work could have included evaluation of the full atmospheric boundary layer in GC2 with comparison against the uncoupled model, and deeper investigation into the modelled surface exchange rates of heat and moisture. Indeed, preliminary cross-sectional charts of the models' ABL were created and investigated, but the differences were found to be unsubstantive. Furthermore, under the cycle of continuous

model improvements at the Met Office, GC2 became ‘out of date’ while carrying out this research. Nonetheless, the results presented in Chapter 3 provide clear evidence of the importance of accurate MIZ simulation in coupled models.

This provided the key motivation for Chapter 4, in which an evaluation of the simulated MIZ is performed for the successor to the coupled model used in Chapter 3, GC3.1, as it became available for research. The Integrated Ice Edge Error (IIEE; c.f. Goessling et al., 2016) metric was employed to quantify the amount of error in forecasts for the same three case study periods investigated in Chapter 3. The IIEE score measures the accuracy of the position of the ice edge, using a prescribed minimum sea ice concentration threshold (typically 15%), by comparing each forecast step to a verification product. Experience gained in Chapter 3 and from Renfrew et al. (2021) informed the use of two satellite-based verification products for comparison and greater insight: OSTIA and AMSR2. To gain a deeper understanding of the sources of error several model experiments were run, including two ocean model resolutions (1/4° and 1/12°) and another version of the 1/4° ocean model modified to employ the updated surface momentum exchange parameterisation from the operational global forecast system mentioned above, i.e., with a reduced drag coefficient over the MIZ.

Before evaluating the sea ice forecasts, a brief analysis of the two satellite sea ice products was carried out using aircraft observations made during the IGP derived from surface albedo measurements. The observational data set is limited both spatially and temporally, yet it is relevant to this focused study having been made around the same region and timing as the forecast domain and periods analysed. The higher resolution AMSR2 product was shown to provide a more accurate representation of the sea ice edge compared to OSTIA, despite a slightly large overall bias in sea ice concentration. This bias, however, is small for both products (roughly 5%), and of less importance when using a metric that only considers the ice edge position. Also, for AMSR2 the bias appears to predominantly originate from overestimation of sea ice concentration in the interior of the ice pack. The OSTIA sea-ice concentration product is poorer in spatial distribution than AMSR2 compared to the in-situ aircraft observations and SAR images. This may be due to the Gaussian smoothing being applied to each grid cell in the original OSI-SAF 401 product that OSTIA is based on, resulting in a lack of sharp gradients at the ice edge.

Comparing the forecast scores to those of a persistent sea ice field, taken as the output from the 1/4° ocean model version fixed at the T+0 hours time step, the GC3.1 configurations with dynamic sea ice showed no clear improvement across the three case study periods. The signature of eddy-driven features along the ice edge qualitatively matches satellite observations

from AMSR2 more accurately in the 1/12° ocean model than the 1/4° ocean model forecasts. The IIEE metric can be decomposed into an absolute extent error and a misplacement error, which helps to identify to sources of error in the model simulations. This shows that despite the realistic appearance of the sea ice field in the 1/12° ocean model, it suffers from similar problems in sea ice extent and misplacement as the lower resolution configurations. Likewise, the 1/4° ocean model with modified atmospheric drag over the MIZ performed very similarly to the 1/4° ocean model with the less advanced MIZ drag scheme that is also used in GC2. This suggests that the drag force exerted on the sea ice by the ocean below is more significant in these case studies than the atmospheric drag from above. It should be noted that due to the inherent chaos of the air-sea-ice dynamics there is a strong dependence on initial conditions fed into the model, hence a perfect simulation of sea ice development is impossible. As such, the morphological accuracy of the 1/12° simulation can be judged as progressive, and greater focus is given during the evaluation to the sea ice extent or MIZ width.

The IIEE scores and their components across the forecasts are most notably different when switching between AMSR2 and OSTIA as verification product. The diffuse ice edge in OSTIA leads to an excess of low concentration sea ice and a representation of the MIZ that is too wide. A significant repercussion of this problem is that OSTIA tends to suggest that the models' MIZ is too narrow, even when verification using AMSR2 finds the model MIZ to be too wide. These opposing results demonstrate a high degree of sensitivity to the verification product used over short-range sea ice forecasts, which should be a critical consideration for future sea ice forecast verification studies. The problem of an overly smooth gradient in sea ice concentration at the ice edge in the OSI-SAF 401 product and those derived from it is often overlooked in larger scale studies, though less important when longer averaging periods are used.

A further key finding is that the most significant amount of error in the forecasts is due to the sea ice field used to initialise the forecasts that is also based on the same OSI-SAF 401 product. This is shown by the large overestimate in sea ice extent in all of the model simulations at T+0 hours verified by AMSR2. A caveat to consider is that the daily satellite sea ice analyses are composited from a range of swaths each day, hence only accurate to +/- 12 hours, and are already 'out of date' by up to 24 hours when ingested by the ocean model. As found by Day et al. (2014) for sea ice thickness analysis, the error introduced by the source sea ice product reduces the forecast capability. Typically, the result is an initial large absolute extent error that then translates to a growing misplacement error over the duration of each forecast as it is advected by the simulated ocean and atmosphere. The recommendation that arises from these results is that it would be beneficial to incorporate higher spatial resolution satellite data with a

more accurate representation of the sea ice edge, such as available from AMSR2, into the operational sea ice product used for model initialisation.

Due to the similarity between the 1/4° ocean model versions with different atmospheric drag parameterisation schemes, further analysis of the separate ocean and wind momentum flux on the sea ice components is needed to decide if the updated surface drag scheme after Lüpkes et al. (2012) and Elvidge et al. (2016) will be suitable for the successor coupled model configuration, GC4. Necessary further improvements are indicated by the significant growth in misplacement error in all the cases analysed. Further work should include evaluation of oceanic and atmospheric drag parameterisations against observations. Existing observational data sets are limited, thus further field campaigns to obtain such specialised measurements would be very advantageous.

Chapter 5 expands on the findings of the previous work, moving from detailed evaluation of short-range forecasts to a wider analysis of long-range climate projections for the subpolar North Atlantic. Historic simulations (1950-2013) and future projections (2015-2100) from the HadGEM3-GC3.1 model (produced as part of CMIP6) were evaluated in terms of their sea ice and total turbulent heat flux (THFX) distribution and trends. The use of simulations that employ the high-resolution ocean grid size (1/12°) evaluated in Chapter 4 for long-range climate projections is a relatively recent advancement at the time of writing. Hence, we take the opportunity to investigate the simulations using the grid configurations named high-high (HH) and medium-medium (MM) with atmosphere - ocean resolutions of 25 km – 1/12° and 60 km – 1/4° respectively. The direct link between the model configurations used in Chapter 4 and Chapter 5, that largely employ the same physical schemes and components, provides two perspectives on the Met Office's state-of-the-art coupled model development. In the earlier chapter it was noted that the 1/12° ocean grid provided potential qualitative improvements in the representation of the ice edge and eddies, yet over the 10-day forecast periods analysed no overall quantitative improvement was realised compared to the 1/4° ocean grid simulations. However, when evaluating the model resolutions over the much longer HadGEM3-GC3.1 historical simulation period (1950-2013), using ERA5 for verification, clear differences in performance emerge.

A key caveat must be underlined in that, due to the limited scope of a single doctoral thesis chapter, we consider projections from only a single modelling centre. However, reliable studies have found that the Met Office – Hadley Centre model is one of the best performing CMIP6 members over a range of grid scales compared with observed AMOC structure and Arctic sea ice

(e.g., Notz et al., 2020; Roberts et al., 2020; Heuzé, 2021). Several key lines of inquiry are outlined in this study: how well the models simulate climatological sea ice and air-sea turbulent heat fluxes; how these fluxes are projected to change over the course of the 21st century as sea ice retreats; what the potential impacts on the formation of dense waters and ocean convection are; and what might be the implications for atmospheric circulation and the climate of Northwest Europe.

While both the HH and MM simulations agree relatively well with the ERA5 climatology (1950 - 2013) in terms of sea ice, mean surface layer pressure, air temperature, surface temperature and total turbulent heat flux, there are some significant regional issues. Most notably, the simulations tend to produce too much sea ice in the Greenland and Iceland Seas, though the HH configuration offers a substantial improvement over the MM. The MM historical simulation produces median sea ice concentrations of approximately 90% and 65% for the Greenland and Iceland Seas respectively, while in the ERA5 record the values are around 55% and 10%. In contrast the respective medians in the HH historical simulation are closer to ERA5 at around 65% and 30%. The over production of sea ice in the MM historical model in the Greenland and Iceland Seas is due to an overly frequent occurrence of an Odden Ice tongue feature. Overestimated sea ice extent causes a substantial cold bias in surface temperature for these regions of approximately 5 - 10 °C for the MM simulation, which leads to substantially reduced near-surface air temperature and turbulent heat fluxes. In contrast, the HH historical simulates the meteorological variables much closer to ERA5 for the Greenland and Iceland Seas due to its better representation of the sea ice.

In light of the issues in the historical simulations - and remembering that we did not compare with other available models – a further effort was made to assess the veracity of the simulations. To this end the 'low ice years' were also evaluated, taken as the years in which sea ice extent in the subpolar North Atlantic was in in the lower quartile in the climatological period for ERA5, or each historic simulation. This removes the time dependency for evaluating model winters, allowing a statistical comparison of each product in a low ice regime. This scheme was devised with the knowledge that Arctic sea ice is very likely to continue to decline in the coming decades. During winters when complexity is reduced with a smaller sea ice extent the models' performance is significantly improved, with the HH simulation performing very well in most regions.

As wintertime sea ice extent reduces in the projections towards 2050, the MM simulation under high emissions forcing, SSP5-8.5, tends to converge with the HH simulation under the same

forcing, further increasing confidence in the MM projections later in the 21st century. The simulations predict that winter sea ice will continue to retreat in the subpolar North Atlantic, particularly rapidly under the high emissions scenario. This is shown to have a substantial impact on the distribution and magnitude of turbulent heat fluxes, with particularly large reductions in the Labrador, Irminger and the interior of the Nordic Seas. However, maxima in turbulent heat fluxes near the sea ice edge will relocate, with a possible intensification over the East Greenland current as it becomes more exposed to cold-air outbreaks. This has the potential to increase ocean convection and mixed layer depths along the East Greenland current, as observed by Våge et al. (2018) and Moore et al. (2022). In Fram Strait and Barents Sea, a dipolar change in turbulent heat flux is predicted to occur, with peak fluxes moving northward into the Arctic Ocean. In general, reductions in sea ice and turbulent heat flux are less severe under the low emissions scenario, SSP1-2.6, reinforcing the urgent need to decarbonise energy systems and global practices to minimise climate impacts.

The projected conditions during the latter decades of the 21st century under the high emissions scenario represent a drastically different subpolar North Atlantic, in which winter sea ice will be significantly diminished, heat extraction from the ocean will be much reduced, and the peak fluxes that remain will be significantly moved. Even under the low emissions scenario, turbulent heat fluxes over the subpolar North Atlantic are projected to decrease, reducing the formation of dense waters that feed into the lower limb of the AMOC in either case. This could help to slow the AMOC, reinforcing the tentative observations of a decreasing trend in strength recent decades (Smeed et al., 2018; Caesar et al., 2018). Indeed, in other CMIP6 models AMOC decline is associated with a decline in North Atlantic Deep Water formation under anthropogenic climate change (Fox-Kemper et al., 2021), however, a shutdown of the AMOC remains very unlikely (Weijer et al., 2020). The implications for atmospheric circulation and the climate of northwest Europe are an overall reduction in the supply of heat into the atmosphere from the subpolar North Atlantic due to air-sea interaction, however, crucially this effect will be dwarfed by the global atmospheric temperature increase under a warming climate, particularly under the high emissions scenario. The projections suggest that latent heat fluxes may form an increasingly larger portion of turbulent heat fluxes due to the greater moisture capacity of a warmer atmosphere, while sensible heat flues are reduced due to the diminishing air-sea temperature gradients, though this could be a topic of further research. Nonetheless, the predicted significant increase in atmospheric temperature and precipitation extremes over northern Europe and globally in CMIP6 models (Almazroui et al., 2021) are of greater concern over the 21st century.

In summary, coupled models' skill at simulating sea ice is a key issue for accurate weather and climate prediction in the subpolar North Atlantic. Important aspects that have been investigated in this thesis include model sea ice extent and the impact on peak fluxes just off the ice edge; the parameterisation of air-sea fluxes in the marginal ice zone and their influence on surface layer meteorology; the ability of models to simulate the distribution of sea ice in the marginal ice zone; and the impacts of retreating sea ice with climate change. In each study in this thesis, it has been demonstrated that errors in the simulation of sea ice can have a dramatic influence on air-sea interaction. This work provides a wealth of evidence that sea ice remains a critical area in need of improvement in numerical weather and climate prediction.

In Chapter 3 GC2 was shown to provide improved forecasts of surface layer meteorology near the MIZ compared to the operational uncoupled model. However, it was also found that in the case studies analysed the apparent improvements may have been the result of competing errors. A simulated MIZ that was consistently too wide resulted in a region where the model surface temperature was biased low and the surface roughness was set too high, yet increased upwards fluxes of heat and moisture were shown to improve forecasted atmospheric temperature and humidity compared with in-situ observations.

In Chapter 4 the skill of GC3.1 forecasted sea ice was similarly difficult to unpick. It did not consistently perform better than a persistent sea ice field, however, particularly in simulations with a 1/12° ocean (compared to a 1/4°), the model was able to reproduce polynyas and eddy-driven mesoscale features. Notably, the largest source of error in these forecasts was shown to be the sea ice product used to initialise the model.

Chapter 5 differed from those preceding in that it contained analysis of several configurations of a long-range climate model, HadGEM3-GC3.1. Yet, like Chapter 4, simulations that employ a 1/12° ocean model displayed improvements compared to a 1/4° ocean model in its climatological distribution of sea ice. Yet issues remained in the position of the ice edge, particularly in the Barents Sea and Fram Strait where ice extent tended to be too low.

Together, the results from each chapter suggest that in GC3.1 provides a useful advantage over GC2, and that increasing the resolution of the ocean model component from 1/4° to 1/12° is beneficial, despite the substantially increased computational cost. However, further work is needed to verify and improve the ocean and sea ice model components, both at a local scale as highlighted in Chapter 3 and 4, and across the entire subpolar North Atlantic in terms of the ocean current pathways, redistribution of heat and sea ice distribution in Chapter 5.

Overall, substantial biases are common in model simulations of the subpolar North Atlantic region, especially in or near the marginal ice zone. This has been demonstrated across this thesis for sea ice extent, modelled surface layer meteorology, temperature at the air-sea-ice boundary and turbulent heat fluxes. Also, the availability of high-quality satellite-based sea ice products is a problem for accurate initialisation of models and their verification. The findings in this thesis provide a clear demonstration of the need for more high quality observations in the polar and subpolar regions that can be used to drive models and inform further development in numerical weather and climate simulation.

6.3 Further work

This thesis comprises several quite different pieces of work, including field campaign based observational study; short-range meteorological forecast evaluation; sea ice prediction and verification; and assessment of long-range climate projections. These topics represent an exploration of air-sea interaction in the subpolar North Atlantic and how it is influenced by the marginal ice zone and are bound together by their focus on wintertime cold-air outbreaks and the improvement of air-sea-ice coupled models for numerical weather prediction. The variation in topics across the duration of the PhD is not by accident, but rather due to a wide range of intrigue and opportunity. As such, the list of ideas, preliminary investigations, trial projects, offshoots and asides that have arisen during the course of this research project is long and has only been curtailed by the feasible scope and time limits of a PhD.

The novelty of the Iceland-Greenland Seas Project (IGP) dataset and the simultaneous measurement of the atmosphere and the ocean provides the opportunity for observational based investigation of the physical air-sea interaction. Indeed, an investigation of the response of the ocean during an IGP cold-air outbreak was carried out (Renfrew et al., 2022). Similarly, intense periods of observations using radiosondes, and continuous atmospheric boundary layer profiling aboard the research vessel *Alliance* has facilitated a publication by Duscha et al. (2021) on the characterisation of coherent boundary layer structures during cold-air outbreaks, yet there is wealth of observational data yet to be utilised. The wide range of data sets, such as the synthesised shipboard meteorological data by Barrell & Renfrew (2020), is available at www.ceda.ac.uk. One such side project that was investigated during this PhD project involved the use of combined atmospheric and hydrographic measurements to constrain boundary layer mass, heat and moisture budgets and investigate their development through the course of a CAO event. Building on work such as that by Brümmer (1996), such a budget analysis could

provide valuable insight into the thermodynamic forcing on the surface waters during cold-air outbreaks and the development of clouds and boundary layer characteristics to inform model development.

In Chapter 3 an evaluation of the Met Office Global Coupled model 2 (GC2) was performed making use of IGP observations. As mentioned, this piece of research was partly drawn to a close due to the arrival of the model's successor configuration, GC3.1. However, the same analysis was not resumed for the new version. This is due to the limited scope of conclusions that could be drawn for global weather models by investigating a relatively small domain for just a few forecast periods. Despite Renfrew et al. (2021) carrying out an evaluation of the ERA5 reanalysis using the IGP data set, efforts to disentangle the effects of the complex competing errors in GC2 of sea surface temperature bias and surface roughness parameterisation on forecasted near-surface meteorology were restricted by the temporal and spatial limits of the data set. Further observations were in fact investigated from several land-based stations on Greenland, Iceland and Jan Mayen Island, but the scope of observational datasets remained too small to gain an in depth understanding of the coupled models' successes and failures. This highlights the longstanding problem of sparse measurement networks in the high latitudes due to their difficult access, testing conditions and high operation costs. However, the IGP was a partner of the Year of Polar Prediction (YOPP) project (https://www.polarprediction.net/), which encompassed several intense observation periods across a large range of instrument platforms in the Arctic and subpolar regions. A valuable extension of the work in this thesis would be to make use of the broad YOPP data sets to verify GC3.1, and its upcoming successor GC4, to gain a deeper understanding of the coupled model's skill and sources of error in their representation of physical processes.

The verification of short-range sea ice forecasts in Chapter 4 was intentionally focused on a small area to enable a focused comparison of the model configurations. As we understand, this is a relatively novel approach as the vast majority of sea ice prediction studies focus on large spatial areas (e.g., the Arctic) at a seasonal to annual time scale (e.g., Goessling et al., 2016). A useful extension to this work would be to study the simultaneous drag forces on sea ice from the ocean and the atmosphere using modelling and observations to gain a better understanding of the sea ice dynamics. The exciting outcome of this research is the stark difference between verifications using two commonly used satellite sea ice products. Moreover, a number of significant problems are highlighted in the OSI-SAF 401 (OSTIA) product, mostly due to a smoothing algorithm that blurs the ice edge. Yet this product is still commonly used to initialise weather models at the Met Office and others, and regularly used for model verification. Our evidence clearly suggests

that there is much work to be done to provide reliable sea ice analyses to feed into models and that there could be substantial benefits for weather forecasts in regions where sea ice plays a role. The stand-out issue is clearly the lack of space infrastructure to provide regular and reliable sea ice measurement. However, incorporation of currently available higher resolution products, such as that of the AMSR2 instrument, into forecast initialisation could be beneficial.,

In Chapter 5 a brief analysis of several long-range climate simulations is performed for the subpolar North Atlantic that were produced as one small part of the cyclical Coupled Model Intercomparison Project. The work presented here barely scratches the surface of the mammoth collaborative effort by researchers across the globe to produce predictions of our future climate. Yet, by taking a relatively focused approach that interrogates historic and future simulations for seven small regions elucidates some key model problems involving sea ice and its influence on turbulent heat fluxes. It is shown that problems in sea ice representation can cause some substantial errors in air-sea interaction in the subpolar regions and getting sea ice right is crucial for accurate projections of the future. This highlights the potential advantages of focusing on a region and attempting to gain a detailed understanding of the interactions between the atmosphere, ocean and ice. This work could be furthered by taking a deeper look into the ocean current pathways and their relationship with sea ice and how they are represented in the climate simulations. Some of the largest biases in climate models remain in the polar regions and reducing these errors should be a priority for further research, particularly with the eye watering pace of climate change already underway in the Arctic.

7 References

Aagaard, K., Foldvik, A., and Hillman, S. R. (1987). The West Spitsbergen Current: disposition and water mass transformation. Journal of Geophysical Research: Oceans, 92(C4), 3778-3784.

Aagaard, K. and Carmack, E. (1989). The role of sea ice and other fresh water in the Arctic circulation. Journal of Geophysical Research, 94(C10), 14485.

Achtert, P., Brooks, I. M., Brooks, B. J., Moat, B. I., Prytherch, J., Persson, P. O. G., and Tjernström, M. (2015). Measurement of wind profiles over the Arctic Ocean from ship-borne Doppler lidar. Atmospheric Measurement Techniques, 8, 4993-5007.

Andersen, S., L. Toudal Pedersen, G. Heygster, R. Tonboe, and L Kaleschke (2007). Intercomparison of passive microwave sea ice concentration retrievals over the high concentration Arctic sea ice. Journal of Geophysical Research 112, C08004.

Andrews, T., Andrews, M. B., Bodas-Salcedo, A., Jones, G. S., Kuhlbrodt, T., Manners, J., Menary, M. B., Ridley, J., Ringer, M. A., Sellar, A. A., Senior, C. A. and Tang, Y. (2019). Forcings, feedbacks, and climate sensitivity in HadGEM3-GC3. 1 and UKESM1. Journal of Advances in Modeling Earth Systems, 11(12), 4377-4394.

Asbjørnsen, H., Årthun, M., Skagseth, Ø., and Eldevik, T. (2020). Mechanisms underlying recent Arctic atlantification. Geophysical Research Letters, 47(15), e2020GL088036.

Atkinson, B. and Wu Zhang, J. (1996). Mesoscale shallow convection in the atmosphere. Reviews of Geophysics, 34(4), 403-431.

Bacon, S., A. Marshall, N. P. Holliday, Y. Aksenov, and S. R. Dye (2014). Seasonal variability of the East Greenland Coastal Current, Journal of Geophysical Research: Oceans, 119, 3967– 3987.

Baek, S. H., Smerdon, J. E., Coats, S., Williams, A. P., Cook, B. I., Cook, E. R., and Seager, R. (2017). Precipitation, temperature, and teleconnection signals across the combined North American, monsoon Asia, and old world drought atlases. Journal of Climate, 30(18), 7141-7155.

Barrell, C. and Renfrew, I. (2020). Iceland Greenland Seas Project (IGP): surface layer meteorological measurements on board the NATO Research Vessel Alliance. Centre for Environmental Data Analysis.
https://catalogue.ceda.ac.uk/uuid/b4ba8f11459c422d84d7293b9211ccf7

Barton, N., Metzger, E. J., Reynolds, C. A., Ruston, B., Rowley, C., Smedstad, O. M., Ridout, J. A., Wallcraft, A., Frolov, S., Hogan, P. and Janiga, M. A. (2021). The Navy's Earth System Prediction Capability: A new global coupled atmosphere-ocean-sea ice prediction system designed for daily to subseasonal forecasting. Earth and Space Science, 8, e2020EA001199.

Bell, B., Hersbach, H., Berrisford, P., Dahlgren, P., Horányi, A., Muñoz Sabater, J., Nicolas, J., Radu, R., Schepers, D., Simmons, A., Soci, C., and Thépaut, J-N. (2020). ERA5 monthly averaged data on single levels from 1950 to 1978 (preliminary version). Copernicus Climate Change Service (C3S) Climate Data Store (CDS). (Accessed on 01-Sep-2021)

Blanchard-Wrigglesworth, E., Barthélemy, A., Chevallier, M., Cullather, R., Fučkar, N., Massonnet, F., Posey, P., Wang, W., Zhang, J., Ardilouze, C., Bitz, C. M., Vernieres, G., Wallcraft, A. and Wang, M. (2016). Multi-model seasonal forecast of Arctic sea-ice: forecast uncertainty at pan-Arctic and regional scales. Climate Dynamics, 49(4), 1399-1410.

Blockley, E. W., Martin, M. J., McLaren, A. J., Ryan, A. G., Waters, J., Lea, D. J., Mirouze, I., Peterson, K. A., Sellar, A., and Storkey, D. (2014). Recent development of the Met Office operational ocean forecasting system: an overview and assessment of the new Global FOAM forecasts. Geoscientific Model Development, 7(6), 2613–2638.

Boé, J., Hall, A., and Qu, X. (2009). September sea-ice cover in the Arctic Ocean projected to vanish by 2100. Nature Geoscience, 2(5), 341-343.

Bourassa, M. A., Gille, S. T., Bitz, C., Carlson, D., Cerovecki, I., Clayson, C. A., Cronin, M. F., Drennan, W. M., Fairall, C. W., Hoffman, R. N., Magnusdottir, G., Pinker, R. T., Renfrew, I. A., Serreze, M., Speer, K., Talley, L. D. and Wick, G. A., (2013). High-Latitude Ocean and Sea Ice Surface Fluxes: Challenges for Climate Research. Bulletin of the American Meteorological Society, 94(3), 403-423.

Boutle, I. A., Eyre, J. E. J., and Lock, A. P. (2014). Seamless stratocumulus simulation across the turbulent gray zone. Monthly Weather Review, 142(4), 1655-1668.

Bracegirdle, T. and Gray, S. (2009). The dynamics of a polar low assessed using potential vorticity inversion. Quarterly Journal of the Royal Meteorological Society, 135(641), 880-893.

Brakstad, A., Våge, K., Håvik, L., and Moore, G. W. K. (2019). Water mass transformation in the Greenland Sea during the period 1986–2016. Journal of Physical Oceanography, 49(1), 121-140.

Bourassa, M. A., Gille, S. T., Bitz, C., Carlson, D., Cerovecki, I., Clayson, C. A., Cronin, M. F., Drennan, W. M., Fairall, C. W., Hoffman, R. N., Magnusdottir, G., Pinker, R. T., Renfrew, I. A.,

Serreze, M., Speer, K., Talley, L. D. and Wick, G. A. (2013). High-Latitude Ocean and Sea Ice Surface Fluxes: Challenges for Climate Research. Bulletin Of The American Meteorological Society, 94(3), 403-423.

Brown, R.A. (1980). Longitudinal instabilities and secondary flows in the planetary boundary layer: A review. Reviews of Geophysics, 18(3), 683.

Brümmer, B. (1996). Boundary-layer modification in wintertime cold-air outbreaks from the Arctic sea ice. Boundary-Layer Meteorology, 80(1-2), 109-125.

Brümmer, B. (1997). Boundary layer mass, water, and heat budgets in wintertime cold-air outbreaks from the Arctic sea ice. Monthly weather review, 125(8), 1824-1837.

Buckley, M. W. and Marshall, J. (2016). Observations, inferences, and mechanisms of the Atlantic Meridional Overturning Circulation: A review. Reviews of Geophysics, 54, 5-63.

Bushuk, M., Winton, M., Haumann, F. A., Delworth, T., Lu, F., Zhang, Y., Jia, L., Zhang, L., Cooke, W., Harrison, M., Hurlin, B., Johnson, N. C., Kapnick, S. B., McHugh, C., Murakami, H., Rosati, A., Tseng, K., Wittenberg, A. T., Yang, X., and Zeng, F. (2021). Seasonal Prediction and Predictability of Regional Antarctic Sea Ice. Journal of Climate, 34(15), 6207-6233.

Caesar, L., Rahmstorf, S., Robinson, A., Feulner, G., and Saba, V. (2018). Observed fingerprint of a weakening Atlantic Ocean overturning circulation. Nature, 556(7700), 191-196.

Cavalieri, D. J., and Parkinson, C. L. (2012). Arctic sea ice variability and trends, 1979-2010, Cryosphere Discussions, 6(2), 957-979.

Chassignet, E. P., Yeager, S. G., Fox-Kemper, B., Bozec, A., Castruccio, F., Danabasoglu, G., Horvat, C., Kim, W. M., Koldunov, N., Li, Y., Lin, P., Liu, H., Sein, D. V., Sidorenko, D., Wang, Q. and Xu, X. (2020). Impact of horizontal resolution on global ocean–sea ice model simulations based on the experimental protocols of the Ocean Model Intercomparison Project phase 2 (OMIP-2). Geoscientific Model Development, 13(9), 4595-4637.

Chechin, D. G., Lüpkes, C., Repina, I. A., and Gryanik, V. M. (2013). Idealized dry quasi 2-D mesoscale simulations of cold-air outbreaks over the marginal sea ice zone with fine and coarse resolution. Journal of Geophysical Research: Atmospheres, 118(16), 8787-8813.

Claud, C., Duchiron, B., and Terray, P. (2007). Associations between large-scale atmospheric circulation and polar low developments over the North Atlantic during winter, Journal of Geophysical Research, 112, D12101.

Collins, M. (2002). Climate predictability on interannual to decadal time scales: The initial value problem. Climate Dynamics, 19, 671–692.

Comiso J.C. (1986). Characteristics of arctic winter sea ice from satellite multispectral microwave observations. Journal of Geophysical Research 91(C1), 975-994.

Comiso J.C, Cavalieri, D.J., C.L. Parkinson, and P. Gloersen (1997). Passive microwave algorithms for sea ice concentration: A comparison of two techniques. Remote Sensing of Environment 60(3), 357-384.

Comiso, J.C., Parkinson, C.L., Gersten, R. and Stock, L. (2008). Accelerated decline in the Arctic sea ice cover. Geophysical Research Letters, 35(1), L01703.

Condron, A., and Renfrew, I. A. (2013). The impact of polar mesoscale storms on northeast Atlantic Ocean circulation. Nature Geoscience, 6(1), 34-37.

Cusinato, E., Rubino, A., and Zanchettin, D. (2021). Winter Euro-Atlantic Climate Modes: Future Scenarios from a CMIP6 Multi-Model Ensemble. Geophysical Research Letters, 48(19), e2021GL094532.

Day, J. J., Hawkins, E., and Tietsche, S. (2014a). Will Arctic sea ice thickness initialization improve seasonal forecast skill? Geophysical Research Letters, 41(21), 7566-7575.

Day, J. J., Tietsche, S., and Hawkins, E. (2014b). Pan-Arctic and Regional Sea Ice Predictability: Initialization Month Dependence. Journal of Climate 27(12), 4371-4390.

Dellink, R., Chateau, J., Lanzi, E., and Magne, B. (2015). Long-term economic growth projections in the Shared Socioeconomic Pathways. Global Environmental Change, 42, 200-214.

Delworth, T. L., Zeng, F., Vecchi, G. A., Yang, X., Zhang, L., and Zhang, R. (2016). The North Atlantic Oscillation as a driver of rapid climate change in the Northern Hemisphere. Nature Geoscience, 9(7), 509-512.

Donlon, C., Martin, M., Stark, J., Roberts-Jones, J., Fiedler, E., and Wimmer, W. (2012). The Operational Sea Surface Temperature and Sea Ice Analysis (OSTIA) system. Remote Sensing Of Environment, 116, 140-158.

Drüe, C. and Heinemann, G. (2001). Airborne Investigation Of Arctic Boundary-Layer Fronts Over The Marginal Ice Zone Of The Davis Strait. Boundary-Layer Meteorology, 101(2), 261-292.

Dukhovskoy, D., Ubnoske, J., Blanchard-Wrigglesworth, E., Hiester, H. and Proshutinsky A. (2015). Skill metrics for evaluation and comparison of sea ice models, Journal of Geophysical Research: Oceans, 120(9), 5910– 5931.

Duscha, C., Barrell, C., Renfrew, I. A., Brooks, I. M., Sodemann, H., and Reuder, J. (2022). A ship-based characterization of coherent boundary-layer structures over the lifecycle of a marine cold-air outbreak. Boundary-Layer Meteorology, 183(3), 355-380.

Elvidge, A. D., Renfrew, I. A., Weiss, A. I., Brooks, I. M., Lachlan-Cope, T. A., and King, J. C. (2016). Observations of surface momentum exchange over the marginal-ice-zone and recommendations for its parameterization. Atmospheric Chemistry and Physics, 16(3), 1545-1563.

Elvidge, A. D., Renfrew, I. A., Brooks, I. M., Srivastava, P., Yelland, M. J., and Prytherch, J. (2021). Surface heat and moisture exchange in the marginal ice zone: Observations and a new parameterization scheme for weather and climate models. Journal of Geophysical Research: Atmospheres, 126, e2021JD034827.

Emmerson, C., and Lahn, G. (2012). Arctic opening: Opportunity and risk in the high north, Chatham House.

Etling, D. and Brown, R. (1993). Roll vortices in the planetary boundary layer: A review. Boundary-Layer Meteorology, 65(3), 215-248.

Eyring, V., Bony, S., Meehl, G. A., Senior, C. A., Stevens, B., Stouffer, R. J., and Taylor, K. E. (2016). Overview of the Coupled Model Intercomparison Project Phase 6 (CMIP6) experimental design and organization, Geoscientific Model Development, 9(5), 1937–1958.

Fairall, C. W., Bradley, E. F., Hare, J. E., Grachev, A. A. and Edson, J. B. (2003). Bulk Parameterization of Air–Sea Fluxes: Updates and Verification for the COARE Algorithm. Journal of Climate, 16(4), 571-591.

Foldvik, A., Aagaard, K., and Torresen, T. (1988). On the velocity field of the East Greenland Current. Deep-Sea Research, 35(8), 1335-1354.

Forbes, R. M., and Ahlgrimm, M. (2014). On the representation of high-latitude boundary layer mixed-phase cloud in the ECMWF global model. Monthly Weather Review, 142(9), 3425-3445.

Fox-Kemper, B., H.T. Hewitt, C. Xiao, G. Aðalgeirsdóttir, S.S. Drijfhout, T.L. Edwards, N.R. Golledge, M. Hemer, R.E. Kopp, G. Krinner, A. Mix, D. Notz, S. Nowicki, I.S. Nurhati, L. Ruiz, J.-B. Sallée, A.B.A. Slangen, and Y. Yu, (2021). Ocean, Cryosphere and Sea Level Change. In Climate

Change 2021: The Physical Science Basis. Contribution of Working Group I to the Sixth Assessment Report of the Intergovernmental Panel on Climate Change [MassonDelmotte, V., P. Zhai, A. Pirani, S.L. Connors, C. Péan, S. Berger, N. Caud, Y. Chen, L. Goldfarb, M.I. Gomis, M. Huang, K. Leitzell, E. Lonnoy, J.B.R. Matthews, T.K. Maycock, T. Waterfield, O. Yelekçi, R. Yu, and B. Zhou (eds.)]. Cambridge University Press.

Gehlen, M., Berthet, S., Séférian, R., Ethé, C., and Penduff, T. (2020). Quantification of Chaotic Intrinsic Variability of Sea-Air CO 2 Fluxes at Interannual Timescales. Geophysical Research Letters, 47(22), e2020GL088304.

Goessling, H. F., Tietsche, S., Day, J. J., Hawkins, E., and Jung, T. (2016). Predictability of the Arctic sea ice edge. Geophysical Research Letters, 43(4), 1642-1650.

Gryschka, M., Drüe, C., Etling, D. and Raasch, S. (2008). On the influence of sea-ice inhomogeneities onto roll convection in cold-air outbreaks. Geophysical Research Letters, 35(23), L23804.

Guemas, V., Blanchard-Wrigglesworth, E., Chevallier, M., Day, J.J., Déqué, M., Doblas-Reyes, F.J., Fučkar, N.S., Germe, A., Hawkins, E., Keeley, S., Koenigk, T., Salas y Mélia, D. and Tietsche, S. (2016), A review on Arctic sea-ice predictability and prediction on seasonal to decadal time-scales. Quarterly Journal of the Royal Meteorological Society, 142(695), 546-561.

Hall, R., Erdélyi, R., Hanna, E., Jones, J. M., and Scaife, A. A. (2015). Drivers of North Atlantic polar front jet stream variability. International Journal of Climatology, 35(8), 1697-1720.

Hallam, S., Josey, S., McCarthy, G., and Hirschi, J. (2022). A regional (land–ocean) comparison of the seasonal to decadal variability of the Northern Hemisphere jet stream 1871–2011. Climate Dynamics, 59(7-8), 1897-1918.

Hansen, J., Ruedy, R., Sato, M., and Lo, K. (2010). Global surface temperature change. Reviews of Geophysics, 48(4), RG4004.

Harden, B. E., and Renfrew, I. A. (2012). On the spatial distribution of high winds off southeast Greenland. Geophysical Research Letters, 39(14), L14806.

Harden, B. E., Renfrew, I. A., and Petersen, G. N. (2015). Meteorological buoy observations from the central Iceland Sea. Journal of Geophysical Research: Atmospheres, 120(8), 3199-3208.

Harden, B. E., Pickart, R. S., Valdimarsson, H., Våge, K., de Steur, L., Richards, C., Bahr, F., Torres, D., Børve, E., Jónsson, S., Macrander, A., Østerhus, S., Håvik, L. and Hattermann, T. (2016).

Upstream sources of the Denmark Strait Overflow: Observations from a high-resolution mooring array. Deep Sea Research Part I: Oceanographic Research Papers, 112, 94-112.

Harold, J., Bigg, G. and Turner, J. (1999). Mesocyclone activity over the North-East Atlantic. Part 1: vortex distribution and variability. International Journal of Climatology, 19(11), 1187-1204.

Hartmann, J., Kottmeier, C. and Raasch, S. (1997). Roll Vortices and Boundary-Layer Development during a Cold Air Outbreak. Boundary-Layer Meteorology, 84(1), pp.45-65.

Håvik, L., Våge, K., Pickart, R. S., Harden, B., Appen, W. V., Jónsson, S. and Østerhus, S. (2017). Structure and Variability of the Shelfbreak East Greenland Current North of Denmark Strait. Journal of Physical Oceanography, 47(10), 2631-2646.

Hebert, D. A., Allard, R. A., Metzger, E. J., Posey, P. G., Preller, R. H., Wallcraft, A. J., Phelps, M. W., and Smedstad, O. M. (2015). Short-term sea ice forecasting: An assessment of ice concentration and ice drift forecasts using the U.S. Navy's Arctic Cap Nowcast/Forecast System. Journal of Geophysical Research: Oceans, 120, 8327– 8345.

Heinemann, G. and T. Klein, (2003). Simulations of Topographically Forced Mesocyclones in the Weddell Sea and the Ross Sea Region of Antarctica. Monthly Weather Review, 131(2), 302–316.

Hersbach, H., Bell, B., Berrisford, P., Biavati, G., Horányi, A., Muñoz Sabater, J., Nicolas, J., Peubey, C., Radu, R., Rozum, I., Schepers, D., Simmons, A., Soci, C., Dee, D., and Thépaut, J-N. (2019). ERA5 monthly averaged data on single levels from 1979 to present. Copernicus Climate Change Service (C3S) Climate Data Store (CDS). (Accessed on 01-Sep-2021).

Heuzé, C. (2021). Antarctic Bottom Water and North Atlantic Deep Water in CMIP6 models. Ocean Science, 17(1), 59-90.

Hirschi, J. J., Barnier, B., Böning, C., Biastoch, A., Blaker, A. T., Coward, A., Danilov, S., Drijfhout, S., Getzlaff, K., Griffies, S. M., Hasumi, H., Hewitt, H., Iovino, D., Kawasaki, T., Kiss, A. E., Koldunov, N., Marzocchi, A., Mecking, J. V., Moat, B., Molines, J., Myers, P. G., Penduff, T., Roberts, M., Treguier, A., Sein, D. V., Sidorenko, D., Small, J., Spence, P., Thompson, L., Weijer, W. and Xu, X. (2020). The Atlantic Meridional Overturning Circulation in High-Resolution Models. Journal Of Geophysical Research: Oceans, 125(4), e2019JC015522.

Holland, M. M., and Bitz, C. M. (2003). Polar amplification of climate change in coupled models. Climate Dynamics, 21(3), 221-232.

Huang, J., Pickart, R., Bahr, F., McRaven, L., and Xu, F. (2021). Wintertime Water Mass Transformation in the Western Iceland and Greenland Seas. Journal Of Geophysical Research: Oceans, 126(8), e2020JC016893.

Hunke, E. C. and Lipscomb, W. H. (2010). CICE: the Los Alamos sea ice model documentation and software users' manual, Version 4.1, LA-CC-06-012, Los Alamos National Laboratory, N.M.

Iles, C., and Hegerl, G. (2017). Role of the North Atlantic Oscillation in decadal temperature trends. Environmental Research Letters, 12(11), 114010.

Ingvaldsen, R. B., Assmann, K. M., Primicerio, R., Fossheim, M., Polyakov, I. V., and Dolgov, A. V. (2021). Physical manifestations and ecological implications of Arctic Atlantification. Nature Reviews Earth and Environment, 2(12), 874-889.

IPCC (2021). Climate Change 2021: The Physical Science Basis. Contribution of Working Group I to the Sixth Assessment Report of the Intergovernmental Panel on Climate Change [Masson-Delmotte, V., P. Zhai, A. Pirani, S.L. Connors, C. Péan, S. Berger, N. Caud, Y. Chen, L. Goldfarb, M.I. Gomis, M. Huang, K. Leitzell, E. Lonnoy, J.B.R. Matthews, T.K. Maycock, T. Waterfield, O. Yelekçi, R. Yu, and B. Zhou (eds.)]. Cambridge University Press.

Isachsen, P., Drivdal, M., Eastwood, S., Gusdal, Y., Noer, G. and Saetra, Ø. (2013). Observations of the ocean response to cold air outbreaks and polar lows over the Nordic Seas. Geophysical Research Letters, 40(14), 3667-3671.

Jackson, L. C., Roberts, M. J., Hewitt, H. T., Iovino, D., Koenigk, T., Meccia, V. L., Roberts, C. D., Ruprich-Robert, Y. and Wood, R. A. (2020). Impact of ocean resolution and mean state on the rate of AMOC weakening. Climate Dynamics, 55(7-8), 1711-1732.

Jiang, L. and O'Neill, B. C. (2015). Global urbanization projections for the Shared Socioeconomic Pathways, Global Environmental Change, 42, 193-199.

Jochumsen, K., Moritz, M., Nunes, N., Quadfasel, D., Larsen, K. M. H., Hansen, B., Valdimarsson, H., and Jonsson, S. (2017). Revised transport estimates of the Denmark Strait overflow. Journal of Geophysical Research: Oceans, 122(4), 3434-3450.

Johannessen, O. M., Johannessen, J. A., Svendsen, E., Shuchman, R. A., Campbell, W. J., and Josberger, E. (1987). Ice-Edge Eddies in the Fram Strait Marginal Ice Zone. Science 236(4800): 427-429.

Johns, T. C., Blockley, E. W., and Ridley, J. K. (2021). Causes and Consequences of Sea Ice Initialization Shock in Coupled NWP Hindcasts with the GC2 Climate Model. Monthly Weather Review, 149(7), 2239-2254.

Jónsson, S. (2007). Volume flux and fresh water transport associated with the East Icelandic Current. Progress in Oceanography, 73(3-4), 231-241.

Jung, T., Gulev, S., Rudeva, I., and Soloviov, V. (2006). Sensitivity of extratropical cyclone characteristics to horizontal resolution in the ECMWF model. Quarterly Journal of the Royal Meteorological Society, 132(619), 1839-1857.

Jung, T., Miller, M. J., Palmer, T. N., Towers, P., Wedi, N., Achuthavarier, D., Adams, J. M., Altshuler, E. L., Cash, B. A., Kinter, I. J. L., Marx, L., Stan, C., and Hodges, K. I. (2012). High-Resolution Global Climate Simulations with the ECMWF Model in Project Athena: Experimental Design, Model Climate, and Seasonal Forecast Skill. Journal of Climate 25(9), 3155–3172.

Jung, T., Serrar, S., and Wang, Q. (2014). The oceanic response to mesoscale atmospheric forcing. Geophysical Research Letters, 41(4), 1255-1260.

Jung, T., Gordon, N. D., Bauer, P., Bromwich, D. H., Chevallier, M., Day, J. J., Dawson, J., Doblas-Reyes, F., Fairall, C., Goessling, H. F., Holland, M., Inoue, J., Iversen, T., Klebe, S., Lemke, P., Losch, M., Makshtas, A., Mills, B., Nurmi, P., Perovich, D., Reid, P., Renfrew, I. A., Smith, G., Svensson, G., Tolstykh, M. and Yang, Q. (2016). Advancing Polar Prediction Capabilities on Daily to Seasonal Time Scales. Bulletin of the American Meteorological Society, 97(9), 1631-1647.

Kanno, Y. and Iwasaki, T. (2019). Future Reductions in Polar Cold Air Mass and Cold Air Outbreaks Revealed From Isentropic Analysis. Geophysical Research Letters, 47(3), e2019GL086076.

Kay, J. E., Deser, C., Phillips, A., Mai, A., Hannay, C., Strand, G., Arblaster, J. M., Bates, S. C., Danabasoglu, G., Edwards, J., Holland, M., Kushner, P., Lamarque, J., Lawrence, D., Lindsay, K., Middleton, A., Munoz, E., Neale, R., Oleson, K., Polvani, L. and Vertenstein, M. (2015). The Community Earth System Model (CESM) Large Ensemble Project: A Community Resource for Studying Climate Change in the Presence of Internal Climate Variability. Bulletin of the American Meteorological Society, 96(8), 1333-1349.

Keeley, S. and Mogensen, K. (2018). Dynamic sea ice in the IFS. ECMWF Newsletter, Number 156, edited by Georg Lentze.

Keen, A., Blockley, E., Bailey, D. A., Boldingh Debernard, J., Bushuk, M., Delhaye, S., Docquier, D., Feltham, D., Massonnet, F., O'Farrell, S., Ponsoni, L., Rodriguez, J. M., Schroeder, D., Swart,

N., Toyoda, T., Tsujino, H., Vancoppenolle, M. and Wyser, K. (2021). An inter-comparison of the mass budget of the Arctic sea ice in CMIP6 models. The Cryosphere, 15(2), 951-982.

Kohout, A. L., Williams, M. J. M., Dean, S. M., and Meylan, M. H. (2014). Storm-induced sea-ice breakup and the implications for ice extent. Nature, 509(7502), 604-607.

Kolstad, E. W., Bracegirdle, T. J., and Seierstad, I. A. (2009). Marine cold-air outbreaks in the North Atlantic: Temporal distribution and associations with large-scale atmospheric circulation. Climate Dynamics, 33(2-3), 187-197.

Kolstad, E. (2011). A global climatology of favourable conditions for polar lows. Quarterly Journal of the Royal Meteorological Society, 137(660), 1749-1761.

Kwok, R. (2018). Arctic sea ice thickness, volume, and multiyear ice coverage: losses and coupled variability (1958–2018). Environmental Research Letters, 13(10).

Landgren, O., Seierstad, I. and Iversen, T. (2019). Projected future changes in Marine Cold-Air Outbreaks associated with Polar Lows in the Northern North-Atlantic Ocean. Climate Dynamics, 53(5-6), 2573-2585.

Lee, J.-Y., J. Marotzke, G. Bala, L. Cao, S. Corti, J.P. Dunne, F. Engelbrecht, E. Fischer, J.C. Fyfe, C. Jones, A. Maycock, J. Mutemi, O. Ndiaye, S. Panickal, and T. Zhou (2021). Future Global Climate: Scenario-Based Projections and Near-Term Information. In Climate Change 2021: The Physical Science Basis. Contribution of Working Group I to the Sixth Assessment Report of the Intergovernmental Panel on Climate Change [Masson-Delmotte, V., P. Zhai, A. Pirani, S.L. Connors, C. Péan, S. Berger, N. Caud, Y. Chen, L. Goldfarb, M.I. Gomis, M. Huang, K. Leitzell, E. Lonnoy, J.B.R. Matthews, T.K. Maycock, T. Waterfield, O. Yelekçi, R. Yu, and B. Zhou (eds.)]. Cambridge University Press.

Liu, A. Q., Moore, G. W. K., Tsuboki, K., and Renfrew, I. A. (2004). A high-resolution simulation of convective roll clouds during a cold-air outbreak. Geophysical Research Letters, 31(3), L03101.

Liu, A. Q., Moore, G. W. K., Tsuboki, K., and Renfrew, I. A. (2006). The effect of the sea-ice zone on the development of boundary-layer roll clouds during cold air outbreaks. Boundary-Layer Meteorology, 118(3), 557-581.

Loeng, H. (1991). Features of the physical oceanographic conditions of the Barents Sea. Polar Research, 10(1), 5-18.

Lüpkes, C., Gryanik, V. M., Hartmann, J. and Andreas, E. L. (2012). A parametrization, based on sea ice morphology, of the neutral atmospheric drag coefficients for weather prediction and climate models. Journal of Geophysical Research, 117, D13112.

Madec, G. (2008). NEMO Ocean Engine, Note du Pole de Modélisation, Institut Pierre-Simon Laplace (IPSL), France, No 27, ISSN No 1288-1619.

Martin, T. and Wadhams, P. (1999). Sea-ice flux in the East Greenland Current. Deep Sea Research Part II: Topical Studies in Oceanography, 46(6-7), 1063-1082.

Marzocchi, A., Hirschi, J. J., Holliday, N. P., Cunningham, S. A., Blaker, A. T. and Coward, A. C. (2015). The North Atlantic subpolar circulation in an eddy-resolving global ocean model. Journal of Marine Systems, 142, 126-143.

McLaren, A. J., Banks, H. T., Durman, C. F., Gregory, J. M., Johns, T. C., Keen, A. B., Ridley, J. K., Roberts, M. J., Lipscomb, W. H., Connolley, W. M. and Laxon, S. W. (2006). Evaluation of the sea ice simulation in a new coupled atmosphere-ocean climate model (HadGEM1). Journal of Geophysical Research, 111, C12014.

Megann, A., Storkey, D., Aksenov, Y., Alderson, S., Calvert, D., Graham, T., Hyder, P., Siddorn, J., and Sinha, B. (2014). GO5.0: the joint NERC-Met Office NEMO global ocean model for use in coupled and forced applications, Geoscientific Model Development, 7(3), 1069-1092.

Meier, W., Hovelsrud, G., Oort, B., Key, J., Kovacs, K., Michel, C., Haas, C., Granskog, M., Gerland, S., Perovich, D., Makshtas, A. and Reist, J. (2014). Arctic sea ice in transformation: A review of recent observed changes and impacts on biology and human activity. Reviews Of Geophysics, 52(3), 185-217.

Melia, N., Haines, K., and Hawkins, E. (2016). Sea ice decline and 21st century trans-Arctic shipping routes. Geophysical Research Letters, 43(18), 9720-9728.

Melsheimer, C. and Spreen, G. (2019). AMSR2 ASI sea ice concentration data, Arctic, version 5.4 (NetCDF) (July 2012 - December 2018). PANGAEA.

Meredith, M., M. Sommerkorn, S. Cassotta, C. Derksen, A. Ekaykin, A. Hollowed, G. Kofinas, A. Mackintosh, J. Melbourne-Thomas, M.M.C. Muelbert, G. Ottersen, H. Pritchard, and E.A.G. Schuur, (2019). Polar Regions. In: IPCC Special Report on the Ocean and Cryosphere in a Changing Climate [H.-O. Pörtner, D.C. Roberts, V. Masson-Delmotte, P. Zhai, M. Tignor, E. Poloczanska, K. Mintenbeck, A. Alegría, M. Nicolai, A. Okem, J. Petzold, B. Rama, N.M. Weyer (eds.)]. Cambridge University Press

Mitchelson-Jacob, G. (1993). Eddies in the Greenland Sea observed from infrared and visible satellite radiometry. Oceanologica Acta, 16, 213-220.

Moore, G. W. K. and Renfrew, I. A., (2005). Tip Jets and Barrier Winds: A QuikSCAT Climatology of High Wind Speed Events around Greenland. Journal of Climate, 18, 3713-3725.

Moore, G. W. K., Renfrew, I. A. and Pickart, R. S. (2012). Spatial distribution of air-sea heat fluxes over the sub-polar North Atlantic Ocean. Geophysical Research Letters, 39(18), L18806.

Moore, G. W. K., Våge, K., Pickart, R. S. and Renfrew, I. A. (2015). Decreasing intensity of open-ocean convection in the Greenland and Iceland seas. Nature Climate Change, 5(9), 877-882.

Moore, G. W. K., Bromwich, D. H., Wilson, A. B., Renfrew, I. A. and Bai, L. (2016). Arctic System Reanalysis improvements in topographically forced winds near Greenland. Quarterly Journal of the Royal Meteorological Society, 142, 2033-2045.

Moore, G. W. K., Schweiger, A., Zhang, J. and Steele, M. (2019). Spatiotemporal Variability of Sea Ice in the Arctic's Last Ice Area. Geophysical Research Letters, 46(20), 11237-11243.

Moore, G. W. K., Våge, K., Renfrew, I. A., and Pickart, R. S. (2022). Sea-ice retreat suggests re-organization of water mass transformation in the Nordic and Barents Seas. Nature Communications, 13(1), 1-8.

Notz, D. (2012). Challenges in simulating sea ice in Earth system models. Wiley Interdisciplinary Reviews: Climate Change, 3, 509–526.

Notz, D. and Stroeve, J. (2016). Observed Arctic sea-ice loss directly follows anthropogenic CO2 emission. Science, 354(6313), 747-750.

Notz, D., Jahn, A., Holland, M., Hunke, E., Massonnet, F., Stroeve, J., Tremblay, B. and Vancoppenolle, M. (2016), The CMIP6 Sea-Ice Model Intercomparison Project (SIMIP): understanding sea ice through climate-model simulations. Geoscientific Model Development, 9(9), 3427-3446.

Notz, D. and SIMIP Community (2020). Arctic sea ice in CMIP6. Geophysical Research Letters, 47, e2019GL086749.

O'Neill, B. C., Kriegler, E., Ebi, K. L., Kemp-Benedict, E., Riahi, K., Rothman, D. S., van Ruijven, B. J., van Vuuren, D. P., Birkmann, J., Kok, K., Levy, M., and Solecki, W. (2015). The roads ahead: Narratives for shared socioeconomic pathways describing world futures in the 21st century. Global Environmental Change, 42, 169-180.

Østerhus, S., Sherwin, T., Quadfasel, D., and Hansen, B. (2008). The Overflow Transport East of Iceland. In: Dickson, R.R., Meincke, J., Rhines, P. (eds) Arctic–Subarctic Ocean Fluxes, 427-441. Springer, Dordrecht.

Østerhus, S., Woodgate, R., Valdimarsson, H., Turrell, B., de Steur, L., Quadfasel, D., Olsen, S. M., Moritz, M., Lee, C. M., Larsen, K. M. H., Jónsson, S., Johnson, C., Jochumsen, K., Hansen, B., Curry, B., Cunningham, S. and Berx, B. (2019). Arctic Mediterranean exchanges: A consistent volume budget and trends in transports from two decades of observations. Ocean Science, 15(2), 379-399.

Overland, J. E. and Wang, M. (2013). When will the summer Arctic be nearly sea ice free? Geophysical Research Letters, 40(10), 2097-2101.

Pagowski, M. and Moore G. W. K. (2001). A Numerical Study of an Extreme Cold-Air Outbreak over the Labrador Sea: Sea Ice, Air–Sea Interaction, and Development of Polar Lows. Monthly Weather Review, 129, 47–72.

Palter, J. B. (2015). The role of the Gulf Stream in European climate. Annual Review of Marine Science (edited by Carlson, C. A. and Giovannoni, S. J.). Volume 7, 113-137.

Papritz, L. and Spengler, T. (2017). A Lagrangian Climatology of Wintertime Cold Air Outbreaks in the Irminger and Nordic Seas and Their Role in Shaping Air–Sea Heat Fluxes. Journal of Climate, 30, 2717–2737.

Perner, K., Moros, M., Otterå, O., Blanz, T., Schneider, R., and Jansen, E. (2019). An oceanic perspective on Greenland's recent freshwater discharge since 1850. Scientific Reports, 9(1), 17680.

Petty, A. A., Schröder, D., Stroeve, J. C., Markus, T., Miller, J., Kurtz, N. T., Feltham, D. L. and Flocco, D. (2017). Skillful spring forecasts of September Arctic sea ice extent using passive microwave sea ice observations. Earth's Future, 5, 254-263.

Pickart, R. S., Spall, M. A., Ribergaard, M. H., Moore, G. W. K., and Milliff, R. F. (2003). Deep convection in the Irminger Sea forced by the Greenland tip jet. Nature, 424(6945), 152-156.

Pithan, F., Svensson, G., Caballero, R., Chechin, D., Cronin, T. W., Ekman, A. M. L., Neggers, R., Shupe, M. D., Solomon, A., Tjernström, M. and Wendisch, M. (2018). Role of air-mass transformations in exchange between the Arctic and mid-latitudes. Nature Geoscience, 11(11), 805-812.

Posey, P. G., Metzger, E. J., Wallcraft, A. J., Hebert, D. A., Allard, R. A., Smedstad, O. M., Phelps, M. W., Fetterer, F., Stewart, J. S., Meier, W. N. and Helfrich, S. R. (2015). Improving Arctic sea ice edge forecasts by assimilating high horizontal resolution sea ice concentration data into the US Navy's ice forecast systems. Cryosphere, 9(4), 1735– 1745.

Rae, J. G. L., H. T. Hewitt, A. B. Keen, J. K. Ridley, A. E. West, C. M. Harris, E. C. Hunke, and Walters D. N. (2015). Development of the global sea ice 6.0 CICE configuration for the met office global coupled model. Geoscientific Model Development, 8(7), 2221-2230.

Rahmstorf, S., Box, J. E., Feulner, G., Mann, M. E., Robinson, A., Rutherford, S., and Schaffernicht, E. J. (2015). Exceptional twentieth-century slowdown in Atlantic Ocean overturning circulation. Nature Climate Change, 5(5), 475-480.

Renfrew, I. A. and Moore, G. W. K. (1999). An Extreme Cold-Air Outbreak over the Labrador Sea: Roll Vortices and Air–Sea Interaction. Monthly Weather Review, 127, 2379–2394.

Renfrew, I. A., Moore, G. W. K., Kristjánsson, J. E., Ólafsson, H., Gray, S. L., Petersen, G. N., Bovis, K., Brown, P. R. A., Føre, I., Haine, T., Hay, C., Irvine, E. A., Lawrence, A., Ohigashi, T., Outten, S., Pickart, R. S., Shapiro, M., Sproson, D., Swinbank, R., Woolley, A., and Zhang, S. (2008). The Greenland Flow Distortion Experiment. Bulletin of the American Meteorological Society, 89(9), 1307-1324.

Renfrew, I. A., Pickart, R. S., Våge, K., Moore, G. W. K., Bracegirdle, T. J., Elvidge, A. D., Jeansson, E., Lachlan-Cope, T., McRaven, L. T., Papritz, L., Reuder, J., Sodemann, H., Terpstra, A., Waterman, S., Valdimarsson, H., Weiss, A., Almansi, M., Bahr, F., Brakstad, A., Barrell, C., Brooke, J. K., Brooks, B. J., Brooks, I. M., Brooks, M. E., Bruvik, E. M., Duscha, C., Fer, I., Golid, H. M., Hallerstig, M., Hessevik, I., Huang, J., Houghton, L., Jónsson, S., Jonassen, M., Jackson, K., Kvalsund, K., Kolstad, E. W., Konstali, K., Kristiansen, J., Ladkin, R., Lin, P., Macrander, A., Mitchell, A., Olafsson, H., Pacini, A., Payne, C., Palmason, B., Pérez-Hernández, M. D., Peterson, A. K., Petersen, G. N., Pisareva, M. N., Pope, J. O., Seidl, A., Semper, S., Sergeev, D., Skjelsvik, S., Søiland, H., Smith, D., Spall, M. A., Spengler, T., Touzeau, A., Tupper, G., Weng, Y., Williams, K. D., Yang, X. and Zhou, S. (2019a). The Iceland Greenland Seas Project. Bulletin of the American Meteorological Society, 100(9), 1795-1817.

Renfrew, I. A., Elvidge, A. D. and Edwards, J. (2019b). Atmospheric sensitivity to marginal-ice-zone drag: Local and global responses. Quarterly Journal of the Royal Meteorological Society, 145(720), 1165-1179.

Renfrew, I. A., C. Barrell, A. D. Elvidge, J. K. Brooke, C. Duscha, J. C. King, J. Kristiansen, T. Lachlan Cope, G. W. K. Moore, R. S. Pickart, J. Reuder, I. Sandu, D. Sergeev, A. Terpstra, K. Våge, and A. Weiss (2021). An evaluation of surface meteorology and fluxes over the Iceland and Greenland Seas in ERA5 reanalysis: The impact of sea ice distribution. Quarterly Journal of the Royal Meteorological Society, 147, 691-712.

Renfrew, I. A., Huang, J., Semper, S., Barrell, C., Terpstra, A., Pickard, R. S., Våge, K., Elvidge, A. D., Spengler, T., Strehl, A-M., and Weiss, A. (2022). Coupled atmosphere-ocean observations of a cold air outbreak and its impact on the Iceland Sea. Quarterly Journal of the Royal Meteorological Society, 149(751), 472-493.

Reuder, J., Kolstad, E., Vage, K., Kristiansen, J., Barrell, C., Elvidge, A.D. and Renfrew, I. A. (2020). Iceland Greenland seas Project (IGP): meteorological buoy measurements. Centre for Environmental Data Analysis, https://catalogue.ceda.ac.uk/uuid/7cc70ebf9ebc46d483fb4f17a984a978.

Ridley, J. K., Blockley, E. W., Keen, A. B., Rae, J. G. L., West, A. E., and Schroeder, D. (2018). The sea ice model component of HadGEM3-GC3.1. Geoscientific Model Development, 11(2), 713-723.

Roberts, M. (2017a). MOHC HadGEM3-GC31-MM model output prepared for CMIP6 HighResMIP, Version 20190501. Earth System Grid Federation, available at https://www.wdc-climate.de/ui/cmip6?input=CMIP6.HighResMIP.MOHC.HadGEM3-GC31-MM.

Roberts, M. (2017b). MOHC HadGEM3-GC31-HH model output prepared for CMIP6 HighResMIP, Earth System Grid Federation, available at: http://cera-www.dkrz.de/WDCC/meta/CMIP6/CMIP6.HighResMIP.MOHC.HadGEM3-GC31-HH.

Roberts, M. J., Baker, A., Blockley, E. W., Calvert, D., Coward, A., Hewitt, H. T., Jackson, L. C., Kuhlbrodt, T., Mathiot, P., Roberts, C. D., Schiemann, R., Seddon, J., Vannière, B. and Vidale, P. L. (2019). Description of the resolution hierarchy of the global coupled HadGEM3-GC3.1 model as used in CMIP6 HighResMIP experiments. Geoscientific Model Development, 12(12), 4999-5028.

Roberts, M. J., Jackson, L. C., Roberts, C. D., Meccia, V., Docquier, D., Koenigk, T., Ortega, P., Moreno-Chamarro, E., Bellucci, A., Coward, A., Drijfhout, S., Exarchou, E., Gutjahr, O., Hewitt, H., Iovino, D., Lohmann, K., Putrasahan, D., Schiemann, R., Seddon, J., Terray, L., Xu, X., Zhang, Q., Chang, P., Yeager, S. G., Castruccio, F. S., Zhang, S. and Wu, L. (2020). Sensitivity of the Atlantic Meridional Overturning Circulation to Model Resolution in CMIP6 HighResMIP

Simulations and Implications for Future Changes. Journal Of Advances In Modeling Earth Systems, 12(8), 1942-2466.

de Roode, S. R., Frederikse, T., Siebesma, A. P., Ackerman, A. S., Chylik, J., Field, P. R., Fricke, J., Gryschka, M., Hill, A., Honnert, R., Krueger, S. K., Lac, C., Lesage, A. T. and Tomassini, L. (2019). Turbulent Transport in the Gray Zone: A Large Eddy Model Intercomparison Study of the CONSTRAIN Cold Air Outbreak Case. Journal Of Advances In Modeling Earth Systems, 11(3), 597-623.

Samir, K.C. and Lutz, W. (2014). The human core of the shared socioeconomic pathways: Population scenarios by age, sex and level of education for all countries to 2100. Global Environmental Change, 42, 181-192.

Balan-Sarojini, B., Tietsche, S., Mayer, M., Balmaseda, M., and Zuo, H. (2019). Towards improved sea ice initialization and forecasting with the IFS. ECMWF Technical Memoranda.

Schmitz, W. J. (1995). On the interbasin-scale thermohaline circulation. Reviews of Geophysics, 33(2), 151-173.

Schweiger, A. J., and Zhang, J. (2015). Accuracy of short-term sea ice drift forecasts using a coupled ice-ocean model. Journal of Geophysical Research: Oceans, 120, 7827-7841.

Screen, J. A., Deser, C., Smith, D. M., Zhang, X., Blackport, R., Kushner, P. J., Oudar, T., McCusker, K. E. and Sun, L. (2018). Consistency and discrepancy in the atmospheric response to Arctic sea-ice loss across climate models. Nature Geoscience, 11(3), 155-163.

Seager, R., Kushnir, Y., Nakamura, J., Ting, M., and Naik, N. (2010). Northern Hemisphere winter snow anomalies: ENSO, NAO and the winter of 2009/10. Geophysical research letters, 37(14), L14703.

Semper, S., Våge, K., Pickart, R. S., Valdimarsson, H., Torres, D. J., and Jónsson, S. (2019). The emergence of the North Icelandic Jet and its evolution from northeast Iceland to Denmark Strait. Journal of Physical Oceanography, 49(10), 2499-2521.

Semper, S., Pickart, R. S., Våge, K., Larsen, K. M. H., Hátún, H., and Hansen, B. (2020). The Iceland-Faroe Slope Jet: a conduit for dense water toward the Faroe Bank Channel overflow. Nature Communications, 11(1), 5390.

Semtner, A. J. (1976). A model for the thermodynamic growth of sea ice in numerical investigations of climate. Journal of Physical Oceanography, 6, 379– 389.

Seneviratne, S.I., X. Zhang, M. Adnan, W. Badi, C. Dereczynski, A. Di Luca, S. Ghosh, I. Iskandar, J. Kossin, S. Lewis, F. Otto, I. Pinto, M. Satoh, S.M. Vicente-Serrano, M. Wehner, and B. Zhou (2021). Weather and Climate Extreme Events in a Changing Climate. In Climate Change 2021: The Physical Science Basis. Contribution of Working Group I to the Sixth Assessment Report of the Intergovernmental Panel on Climate Change [MassonDelmotte, V., P. Zhai, A. Pirani, S.L. Connors, C. Péan, S. Berger, N. Caud, Y. Chen, L. Goldfarb, M.I. Gomis, M. Huang, K. Leitzell, E. Lonnoy, J.B.R. Matthews, T.K. Maycock, T. Waterfield, O. Yelekçi, R. Yu, and B. Zhou (eds.)]. Cambridge University Press.

Sergeev, D. E., Renfrew, I. A., Spengler, T. and Dorling, S. R. (2017). Structure of a shear-line polar low. Quarterly Journal of the Royal Meteorological Society, 143, 12-26.

Serreze, M., and Barry, R. (2011). Processes and impacts of Arctic amplification: A research synthesis. Global And Planetary Change, 77(1-2), 85-96.

Sévellec, F., Fedorov, A. and Liu, W. (2017). Arctic sea-ice decline weakens the Atlantic Meridional Overturning Circulation. Nature Climate Change 7(8), 604–610.

Shaffrey, L. C., Hodson, D., Robson, J., Stevens, D. P., Hawkins, E., Polo, I., Stevens, I., Sutton, R. T., Lister, G., Iwi, A. and Smith, D. (2016). Decadal predictions with the HiGEM high resolution global coupled climate model: description and basic evaluation. Climate Dynamics, 48, 297-311.

Shapiro, M. A., Fedor, L. S., and Hampel, T. (1987). Research aircraft measurements of a polar low over the Norwegian Sea. Tellus A: Dynamic Meteorology and Oceanography, 39(4), 272-306.

Shepherd, T. G., Boyd, E., Calel, R. A., Chapman, S. C., Dessai, S., Dima-West, I. M., Fowler, H. J., James, R., Maraun, D., Martius, O., Senior, C. A., Sobel, A. H., Stainforth, D. A., Tett, S. F. B., Trenberth, K. E., van den Hurk, B. J. J. M., Watkins, N. W., Wilby, R. L. and Zenghelis, D. A. (2018). Storylines: an alternative approach to representing uncertainty in physical aspects of climate change. Climatic Change, 151(3-4), 555-571.

Sigmond, M., Fyfe, J. C., Flato, G. M., Kharin, V. V., and Merryfield, W. J. (2013). Seasonal forecast skill of Arctic sea ice area in a dynamical forecast system. Geophysical Research Letters, 40, 529-534.

Sigmond, M., Fyfe, J. C., and Swart, N. C. (2018). Ice-free Arctic projections under the Paris Agreement. Nature Climate Change, 8(5), 404-408.

Small, R. J., Bacmeister, J., Bailey, D., Baker, A., Bishop, S., Bryan, F., Caron, J., Dennis, J., Gent, P., Hsu, H. M., Jochum, M., Lawrence, D., Muñoz, E., diNezio, P., Scheitlin, T., Tomas, R., Tribbia,

J., Tseng, Y. H., and Vertenstein, M. (2014). A new synoptic scale resolving global climate simulation using the Community Earth System Model. Journal of Advances in Modeling Earth Systems, 6, 1065-1094.

Smedsrud, L. H., Muilwijk, M., Brakstad, A., Madonna, E., Lauvset, S. K., Spensberger, C., Born, A., Eldevik, T., Drange, H., Jeansson, E., Li, C., Olsen, A., Skagseth, Ø., Slater, D. A., Straneo, F., Våge, K. and Årthun, M. (2021). Nordic Seas Heat Loss, Atlantic Inflow, and Arctic Sea Ice Cover Over the Last Century. Reviews Of Geophysics, 60(1), e2020RG000725.

Smeed, D. A., Josey, S. A., Beaulieu, C., Johns, W. E., Moat, B. I., Frajka-Williams, E., Rayner, D., Meinen, C. S., Baringer, M. O., Bryden, H. L. and McCarthy, G. D. (2018). The North Atlantic Ocean Is in a State of Reduced Overturning. Geophysical Research Letters, 45(3), 1527-1533.

Smith, D. M. (1996). Extraction of winter total sea ice concentration in the Greenland and Barents Seas from SSM/I data. International Journal of Remote Sensing 17(13), 2625-2646.

Smith, G. T., Jung, T., Gordon, N., Klebe, S., Goessling, H. F., Bauer, P., Bromwich, D., Chevallier, M., Day, J., Doblas-Reyes, F., Holland, M., Inoue, J., Iversen, T., Lemke, P., Makshtas, A., Mills, B., Nurmi, P., Renfrew, I., Reid, P., Svensson, G., Tolstykh, M. and Yang, Q. (2015). The Year of Polar Prediction (YOPP): Challenges and opportunities in ice-ocean forecasting. Ocean Quarterly Newsletter, (51), 9-12.

Smith, G.C., Roy, F., Reszka, M., Surcel Colan, D., He, Z., Deacu, D., Belanger, J.-M., Skachko, S., Liu, Y., Dupont, F., Lemieux, J.-F., Beaudoin, C., Tranchant, B., Drévillon, M., Garric, G., Testut, C.-E., Lellouche, J.-M., Pellerin, P., Ritchie, H., Lu, Y., Davidson, F., Buehner, M., Caya, A. and Lajoie, M. (2016). Sea ice forecast verification in the Canadian Global Ice Ocean Prediction System. Quarterly Journal of the Royal Meteorological Society, 142, 659-671.

Smith, E. and Sheridan, S. (2020). Where Do Cold Air Outbreaks Occur, and How Have They Changed Over Time? Geophysical Research Letters, 47(13), e2020GL086983.

Spensberger, C. and Spengler, T. (2021). Sensitivity of Air-Sea Heat Exchange in Cold-Air Outbreaks to Model Resolution and Sea-Ice Distribution. Journal of Geophysical Research: Atmospheres, 126(5), e2020JD033610.

Spreen, G., Kaleschke, L., and Heygster, G. (2008). Sea ice remote sensing using AMSR-E 89-GHz channels. Journal of Geophysical Research, 113, C02S03.

Storkey, D., Blaker, A. T., Mathiot, P., Megann, A., Aksenov, Y., Blockley, E. W., Calvert, D., Graham, T., Hewitt, H. T., Hyder, P., Kuhlbrodt, T., Rae, J. G. L., and Sinha, B. (2018). UK Global

Ocean GO6 and GO7: a traceable hierarchy of model resolutions. Geoscientific Model Development, 11(8), 3187–3213.

Stroeve, J., Holland, M. M., Meier, W., Scambos, T., and Serreze, M. (2007). Arctic sea ice decline: Faster than forecast. Geophysical Research Letters, 34, L09501.

Stroeve, J., Hamilton, L. C., Bitz, C. M., and Blanchard-Wrigglesworth, E. (2014). Predicting September sea ice: Ensemble skill of the SEARCH Sea Ice Outlook 2008–2013. Geophysical Research Letters, 41(7), 2411– 2418.

Stroeve, J. C., S. Jenouvrier, G. G. Campbell, C. Barbraud, and K. Delord, (2016). Mapping and assessing variability in the Antarctic marginal ice zone, pack ice and coastal polynyas in two sea ice algorithms with implications on breeding success of snow petrels. Cryosphere, 10, 1823-1843.

Strong, C., Magnusdottir, G., and Stern, H. (2009). Observed feedback between winter sea ice and the North Atlantic Oscillation. Journal of Climate, 22(22), 6021-6032.

Strong, C. and Rigor, I. (2013). Arctic marginal ice zone trending wider in summer and narrower in winter. Geophysical Research Letters, 40(18), 4864-4868.

Sutherland, D. and Pickart, R. (2008). The East Greenland Coastal Current: Structure, variability, and forcing. Progress in Oceanography, 78(1), 58-77.

Swift, J. H., and Aagaard, K. (1981). Seasonal transitions and water mass formation in the Iceland and Greenland seas. Deep Sea Research Part A. Oceanographic Research Papers, 28(10), 1107-1129.

Talley, L. (1996). North Atlantic circulation and variability, reviewed for the CNLS conference. Physica D: Nonlinear Phenomena, 98(2-4), 625-646.

Terpstra, A. and Watanabe, S. (2020). Polar Lows. Oxford Research Encyclopaedia of Climate Science, Oxford University Press.

Terpstra, A., Renfrew, I. A., and Sergeev, D. E. (2021). Characteristics of Cold-Air Outbreak Events and Associated Polar Mesoscale Cyclogenesis over the North Atlantic Region. Journal of Climate, 34(11), 4567-4584.

Thompson, D. and Wallace, J. (2001). Regional Climate Impacts of the Northern Hemisphere Annular Mode. Science, 293(5527), 85-89.

Tietsche, S., J. Day, V. Guemas, W. Hurlin, S. Keeley, D. Matei, R. Msadek, M. Collins, and E. Hawkins (2014). Seasonal to interannual Arctic sea ice predictability in current global climate models. Geophysical Research Letters, 41(3), 1035– 1043.

Trigo, R. M., Osborn, T. J., and Corte-Real, J. M. (2002). The North Atlantic Oscillation influence on Europe: climate impacts and associated physical mechanisms. Climate Research, 20(1), 9-17.

Tsubouchi, T., Våge, K., Hansen, B., Larsen, K. M. H., Østerhus, S., Johnson, C., Jónsson, S. and Valdimarsson, H. (2020). Increased ocean heat transport into the Nordic Seas and Arctic Ocean over the period 1993–2016. Nature Climate Change, 11(1), 21-26.

Våge, K., Pickart, R. S., Spall, M. A., Valdimarsson, H., Jónsson, S., Torres, D. J., Østerhus, S. and Eldevik, T. (2011). Significant role of the North Icelandic Jet in the formation of Denmark Strait overflow water. Nature Geoscience, 4(10), 723-727.

Våge, K., Pickart, R. S., Spall, M. A., Moore, G., Valdimarsson, H., Torres, D. J., Erofeeva, S. Y. and Nilsen, J. E. Ø. (2013). Revised circulation scheme north of the Denmark Strait. Deep Sea Research Part I: Oceanographic Research Papers, 79, 20-39.

Våge, K., Moore, G. W. K., Jónsson, S., and Valdimarsson, H. (2015). Water mass transformation in the Iceland Sea. Deep Sea Research Part I: Oceanographic Research Papers, 101, 98-109.

Våge, K., Papritz, L., Håvik, L., Spall, M. A. and Moore, G. W. K. (2018). Ocean convection linked to the recent ice edge retreat along east Greenland. Nature Communications 9(1), 1287.

Vihma, T., Pirazzini, R., Fer, I., Renfrew, I. A., Sedlar, J., Tjernström, M., Lüpkes, C., Nygård, T., Notz, D., Weiss, J., Marsan, D., Cheng, B., Birnbaum, G., Gerland, S., Chechin, D. and Gascard, J. C. (2014). Advances in understanding and parameterization of small-scale physical processes in the marine Arctic climate system: a review. Atmospheric Chemistry and Physics, 14(17), 9403-9450.

Visbeck, M., Hurrell, J., Polvani, L., and Cullen, H. (2001). The North Atlantic Oscillation: Past, present, and future. Proceedings of the National Academy Of Sciences, 98(23), 12876-12877.

Voet, G., Quadfasel, D., Mork, K. A., and Søiland, H. (2010). The mid-depth circulation of the Nordic Seas derived from profiling float observations. Tellus A: Dynamic Meteorology and Oceanography, 62(4), 516-529.

de Vos, M., Barnes, M., Biddle, L. C., Swart, S., Ramjukadh, C-L and M. Vichi (2021). Evaluating numerical and free-drift forecasts of sea ice drift during a Southern Ocean research expedition: An operational perspective. Journal of Operational Oceanography, 15(3), 187-203.

Wacker, U., Potty, K. J., Lüpkes, C., Hartmann, J., and Raschendorfer, M. (2005). A case study on a polar cold air outbreak over Fram Strait using a mesoscale weather prediction model. Boundary-Layer Meteorology, 117, 301-336.

Wadhams, P., Comiso, J. C., Prussen, E., Wells, S., Brandon, M., Aldworth, E., Viehoff, T., Allegrino, R., and Crane, D. R. (1996). The development of the Odden ice tongue in the Greenland Sea during winter 1993 from remote sensing and field observations. Journal of Geophysical Research, 101 (C8), 18213– 18235.

Wadhams, P. and Comiso, J. C. (1999). Two modes of appearance of the Odden ice tongue in the Greenland Sea. Geophysical Research Letters, 26(16), 2497-2500.

Wallace, J. M. and Hobbs, P. V. (1977). Atmosphere science-an introductory survey. Atmosphere science-an introductory survey: V.

Walters, D., Boutle, I., Brooks, M., Melvin, T., Stratton, R., Vosper, S., Wells, H., Williams, K., Wood, N., Allen, T., Bushell, A., Copsey, D., Earnshaw, P., Edwards, J., Gross, M., Hardiman, S., Harris, C., Heming, J., Klingaman, N., Levine, R., Manners, J., Martin, G., Milton, S., Mittermaier, M., Morcrette, C., Riddick, T., Roberts, M., Sanchez, C., Selwood, P., Stirling, A., Smith, C., Suri, D., Tennant, W., Vidale, P. L., Wilkinson, J., Willett, M., Woolnough, S. and Xavier, P. (2017). The Met Office Unified Model Global Atmosphere 6.0/6.1 and JULES Global Land 6.0/6.1 configurations. Geoscientific Model Development, 10(4), 1487-1520.

Walters, D., Baran, A. J., Boutle, I., Brooks, M., Earnshaw, P., Edwards, J., Furtado, K., Hill, P., Lock, A., Manners, J., Morcrette, C., Mulcahy, J., Sanchez, C., Smith, C., Stratton, R., Tennant, W., Tomassini, L., Van Weverberg, K., Vosper, S., Willett, M., Browse, J., Bushell, A., Carslaw, K., Dalvi, M., Essery, R., Gedney, N., Hardiman, S., Johnson, B., Johnson, C., Jones, A., Jones, C., Mann, G., Milton, S., Rumbold, H., Sellar, A., Ujiie, M., Whitall, M., Williams, K., and Zerroukat, M. (2019). The Met Office Unified Model Global Atmosphere 7.0/7.1 and JULES Global Land 7.0 configurations. Geoscientific Model Development, 12(5), 1909–1963.

Wang, Q., Wekerle, C., Wang, X., Danilov, S., Koldunov, N., Sein, D., Sidorenko, D., Appen, W. and Jung, T. (2020). Intensification of the Atlantic Water Supply to the Arctic Ocean Through Fram Strait Induced by Arctic Sea Ice Decline. Geophysical Research Letters, 47(3), e2019GL086682.

Weijer, W., Cheng, W., Drijfhout, S. S., Fedorov, A. V., Hu, A., Jackson, L. C., Liu, W., McDonagh, E. L., Mecking, J. V. and Zhang, J. (2019). Stability of the Atlantic Meridional Overturning

Circulation: A review and synthesis. Journal of Geophysical Research: Oceans, 124(8), 5336-5375.

Weiss, A. I., King, J. C., Lachlan-Cope, T. A., and Ladkin, R. S. (2011). On the effective aerodynamic and scalar roughness length of Weddell Sea ice. Journal of Geophysical Research, 116, D19119.

Weiss, A. I., King, J. C., Lachlan-Cope, T. A., and Ladkin, R. S. (2012). Albedo of the ice covered Weddell and Bellingshausen Seas. The Cryosphere, 6(2), 479-491.

Williams, K. D., Harris, C. M., Bodas-Salcedo, A., Camp, J., Comer, R. E., Copsey, D., Fereday, D., Graham, T., Hill, R., Hinton, T., Hyder, P., Ineson, S., Masato, G., Milton, S. F., Roberts, M. J., Rowell, D. P., Sanchez, C., Shelly, A., Sinha, B., and Walters, D. N. (2015). The Met Office Global Coupled model 2.0 (GC2) configuration. Geoscientific Model Development, 8(5), 1509-1524.

Williams, K. D., Copsey, D., Blockley, E. W., Bodas-Salcedo, A., Calvert, D., Comer, R., Davis, P., Graham, T., Hewitt, H. T., Hill, R., Hyder, P., Ineson, S., Johns, T. C., Keen, A. B., Lee, R. W., Megann, A., Milton, S. F., Rae, J. G. L., Roberts, M. J., Scaife, A. A., Schiemann, R., Storkey, D., Thorpe, L., Watterson, I. G., Walters, D. N., West, A., Wood, R. A., Woollings, T. and Xavier, P. K. (2017). The Met Office Global Coupled model 3.0 and 3.1 (GC3.0 and GC3.1) configurations. Journal of Advances in Modeling Earth Systems, 10(2), 357-380.

Yadav, J., Kumar, A. and Mohan, R. (2020). Dramatic decline of Arctic sea ice linked to global warming. Nature Hazards, 103, 2617–2621.

Young, G., Jones, H.M., Choularton, T.W., Crosier, J., Bower, K.N., Gallagher, M.W., Davies, R.S., Renfrew, I.A., Elvidge, A.D., Darbyshire, E. and Marenco, F. (2016). Observed microphysical changes in Arctic mixed-phase clouds when transitioning from sea ice to open ocean. Atmospheric Chemistry and Physics, 16(21), 13945–13967.

Yu, B., Lin, H., Wu, Z. W., and Merryfield, W. J. (2018). The Asian–Bering–North American teleconnection: seasonality, maintenance, and climate impact on North America. Climate Dynamics, 50(5), 2023-2038.

Zhang, R. and Thomas, M. (2021). Horizontal circulation across density surfaces contributes substantially to the long-term mean northern Atlantic Meridional Overturning Circulation. Communications Earth and Environment 2(1), 112.

Zheng, F., Sun, Y., Yang, Q., and Mu, L. (2021). Evaluation of Arctic sea-ice cover and thickness simulated by MITgcm. Advances in Atmospheric Sciences, 38, 29-48.